Clefted Equilibrium Shapes of Superpressure Balloon Structures

Thesis by

Xiaowei Deng

In Partial Fulfillment of the Requirements

for the Degree of

Doctor of Philosophy

California Institute of Technology

Pasadena, California

2012

(Defended April 6, 2012)

Acknowledgements

First and foremost, I would like to extend special thanks to my supervisor, Professor Sergio Pellegrino for his guidance and encouragement throughout my PhD studies. He gave me the opportunity to start my first year of PhD at Cambridge, created my new life by taking me to Caltech, and helped me to survive here. My life would sink into gloomy mist and all my dreams to the future would become bubbles without his salvation. Deep in my heart, life is such a miracle that I am the one with huge luck to meet another who never abandons you in the extremity and totally diverts the track of your future. His insight, enthusiasm, and expertise in the field of space structures have been a constant source of inspiration. Also I must thank Professor Chris Calladine for his valuable advice and suggestions.

I have been enjoying being a member of the NASA Super-Pressure Balloon Team and wish to thank them for their contributions to this research. I am truly grateful to Dr. David Wakefield (Tensys) and Dr. Jim Rand (Winzen Engineering) for helpful discussions. I must note that David Wakefield and Adam Brown provide results of the last three sets of cases for dimensional analysis in Chapter 6. I would like to extend my thanks to members of the NASA Balloon Program Office (BPO), in particular Henry Cathey, Debora Fairbrother, and Rodger Farley.

I need to thank the members of both my thesis defense and candidacy examination committees, Professors Guruswami Ravichandran, Michael Ortiz, and Kaushik Bhattacharya for helpful discussions and suggestions. I also want to acknowledge the support and inspiration of Professors Yongjiu Shi, my master advisor from Tsinghua University.

I would like to extend my gratitude to past and current colleagues in the Deployable Structures Group at Cambridge and Space Structures group at Caltech for their constructive suggestions and helpful discussions. I need to mention particularly Yixiang Xu, Ahmad Kueh, Quan Long, Markus Pagitz, Matthew Santer, and Tobias Gerngross from Cambridge, and Xin Ning, Francisco Lopez Jimenez, Olive Stohlman, Kawai Kowk, and Devvrath Khatri from Caltech. Chinthaka Mallikarachchi is the most special friend who has accompanied me for more than five years from Cambridge to Caltech. I owe him so much for unconditional help both academically and in life.

I am grateful for the funding provided by the NASA Balloon Program Office. The generous financial support from Dorothy Hodgkin Postgraduate Awards (DHPA) offered cooperatively by the Engineering and Physical Sciences Research Council (EPSRC) and the Shell Co., which allowed me to focus on my studies at

Cambridge, is gratefully appreciated.

Finally, my most sincere thanks to my family who are the people most special to me. In particular the deepest gratitude to my aunt who most steadily stands by my side to support my decisions and always encourages me to follow my dreams.

Abstract

This thesis presents a numerical and analytical study of the clefted equilibrium shape of superpressure balloon structures. Lobed superpressure balloons have shown a tendency to deploy into unexpected asymmetric shapes, hence their design has to strike a balance between the lower stresses achieved by increasing lobing and the risk of incomplete deployment. Extensive clefting is a regular feature of balloons that are incompletely inflated, and is regularly seen during launch and ascent. Our particular interest in the research is in clefts that remain once a balloon has reached its float altitude and is fully pressurized.

A simplified simulation technique for orthotropic viscoelastic membranes is presented in the thesis. Wrinkling is detected by a combined stress-strain criterion and an iterative scheme searches for the wrinkle angle using a pseudoelastic material stiffness matrix based on a nonlinear viscoelastic constitutive model. This simplified model has been implemented in ABAQUS/Explicit and is able to compute the behavior of a membrane structure by superposition of a small number of response increments. The model has been tested against a published solution for a time-independent isotropic membrane under simple shear and also against experimental results on StratoFilm 420 under simple shear.

A fully three-dimensional finite element model of balloon structures incorporating wrinkling and frictionless contact, able to simulate the shapes taken up by lobed superpressure balloons during the final stages of their ascent has been established. Two different methods have been considered to predict the clefts: (i) deflation and inflation method and (ii) constraint shift method. In method (i), the starting configuration is obtained by deflating an initially symmetric balloon subject to uniform pressure. The deflation simulation is continued until the differential pressure at the bottom of the balloon has become negative, at which point the balloon is extensively clefted. The balloon is then inflated by increasing the bottom pressure while maintaining a uniform vertical pressure gradient, and the evolution of the shape and stress distribution of the balloon is studied. Two different designs of superpressure balloons are investigated: a flat facet balloon and a highly lobed balloon. It is found that the flat facet balloon follows essentially the same path during deflation and inflation, and hence will deploy into a unique, symmetric shape. For the lobed balloon it is found that it follows different paths during deflation and inflation, and deploys into an alternate, clefted equilibrium shape.

Compared to method (i), method (ii) is computationally a more efficient clefting test. The test consists in setting up the balloon in its symmetrically inflated configuration, then breaking the symmetry of this

shape by artificially introducing a clefting imperfection, and finally determining the equilibrium shape of the balloon. The clefting imperfection is computed by shifting the constraint at the bottom of the balloon and removing the pressure in the bottom region, below the shifted constraint. The clefting test is applied successfully to three 27 m diameter superpressure balloons that have been tested indoors by NASA, of which one had remained clefted when it was inflated and the other two had deployed completely.

In addition to numerical simulations, formulation of a new cleft factor (CF_6), employed as an indicator of tendency to S-cleft for superpressure balloons based on constant-stress design has been established through dimensional analysis. The cleft factor, defined as the ratio of clefted volume to cyclically symmetrical volume, is expressed in the form of power law relation of the dimensionless groups. An example illustrates how to calculate the coefficients of the analytical formula and analyze sensitivity of design parameters to clefting.

Contents

List of Figures

List of Tables

Chapter 1

Introduction

There are two types of aircrafts to overcome gravity: aerostatic machines that rely on the density differences between envelope gas and atmosphere, and aerodynamic systems that rely on thrust and forward speed. Balloon structure, dependent on buoyancy to generate lift, is one type of lighter-than-air system. Its theoretical foundation was laid by Archimedes (287-212 B.C.), who stated that the buoyant force on a submerged object is equal to the weight of the fluid that is displaced by the object.

1.1 Brief history of ballooning

1.1.1 Premodern balloons

The sky lantern, also known as Kongming lantern, is a prototype of the hot air balloon, see Figure 1.1(a). It was invented by Liang Zhuge, a famous Chinese military strategist in the Three Kingdoms era (220-280 A.D.). Its bamboo frame is covered with oiled paper, and a small candle is put inside. Similar to the hot air balloon, the lantern rises into the sky when the air inside is heated by the lit candle. In ancient China, airborne lanterns were used for military signaling; while nowadays in traditional festivals, people convey the best wishes to the heavens, and believe in wishes coming true through lighting up a lantern and releasing it to the sky.

The famous Nazca Lines and designs in Southern Peru are perplexing archaeological riddles. Julian Nott and Jim Woodman speculated the Nazca people may have used hot air balloons as a tool for designing the figures 1500 years ago. They demonstrated the idea by making the flight of a "prehistoric" balloon over the Nazca lines in the late 1970s and again in 2003, as shown in Figure 1.1(b). Based on archeological evidence, the balloon was designed with woven cotton fabric and inflated over a smoke fire.

1.1.2 Invention of modern balloons in 18th century

The earliest recorded hot air balloon was built in 1783 by the brothers, Joseph-Michel and Jacques-Etienne Montgolfier in Annonay, France. By observing that smoke tended to rise and that paper bags placed over

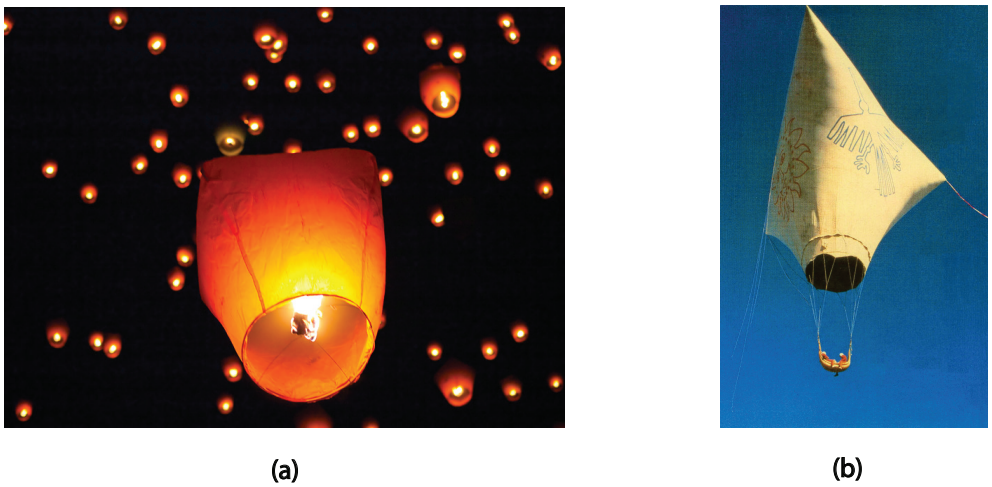

Figure 1.1: (a) Sky lantern (www.flickr.com/photos/olvwu), (b) Revisit of Nazca "prehistoric" balloon hanging a gondola (www.nott.com).

a fire expanded and also rose, they believed they had discovered a new gas, which they called "Montgolfier gas" that was lighter than air and might cause the inflated balloons to rise. Actually the scientific principle behind the fact that hot air rises is that it is less dense than cold air. Figure 1.2(a) shows the Montgolfier's hot air balloon using simple materials. The envelope was made from fabric lined with light colored paper, and a layer of alum coated the envelope to prevent it catching fire. After experimenting with unmanned balloons and flights with animals, the first manned flight took place on November 21st, 1783. The human passengers, a military officer, Francois d'Arlandes, and a physics professor named Pilatre de Rozier, flew untethered to 3000 feet and traveled about 5.5 miles in a 25-minute flight.

After the pioneering Montgolfier brothers' success, Jacques Charles, a French professor of physics, joined forces with two local craftsmen, Anne-Jean and Marie-Noel Robert, to produce a superior balloon. Charles had the misconception that the Montgolfiers had been filling their balloons with hydrogen instead of hot air, which led to the creation of a different type of aerostat, gas balloon. Unlike the hot air balloon requiring an open fire, which was quite dangerous, in the balloon design of Charles, a lighter-than-air gas, hydrogen, was completely enclosed in the balloon before liftoff. The spherical balloon they constructed was 13 feet in diameter, made of silk with an impermeable rubberized coating to contain the lifting gas. Their unmanned balloon ascended from the Champ de Mars in Paris, where the Eiffel Tower is now located, on August 27th 1783, and rose 3000 feet before falling to the ground 15 miles away in 45 minutes. Some months later Charles and the Robert brothers were ready with another hydrogen-filled balloon with a larger diameter of 26.75 feet which could carry two men, see Figure 1.2(b). On December 1st 1783 their second balloon made a manned flight piloted by Jacques Charles and Nicolas-Louis Robert, 10 days after the first manned flight in a Montgolfier hot air balloon. The two men ascended to a height of 1800 ft, and descended about 27 miles away after a two-hour flight. This balloon was much like a modern balloon. To avoid another structural

failure due to increasing differential pressures, the gas balloon was provided with an open neck serving as a safety valve, which has remained the standard type in use throughout the centuries. Stones were used for ballast, and a barometer and a thermometer were carried to measure the pressure and temperature of the air, making this the first scientific balloon flight.

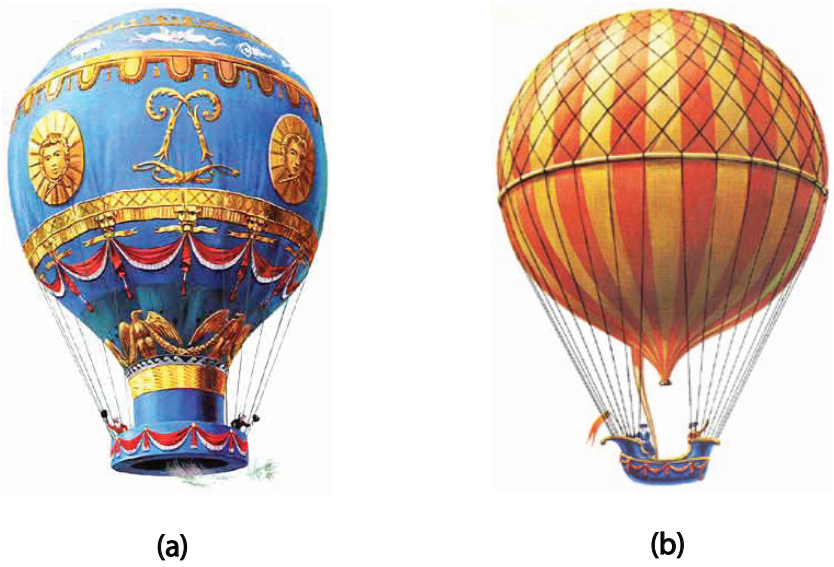

Figure 1.2: (a) Montgolfier hot air balloon (b) Charles hydrogen balloon (www.fiddlersgreen.net).

1.1.3 Early scientific balloons in 19th century

The early balloon flights in the 19th century were scientific experiments in nature because no one could predict what the effects would be when the balloonists attempted to fly farther, higher and longer.

The scientists Jean Baptiste Biot and Joseph Louis Gay-Lussac rose to 13,000 feet to make electromagnetic observations over Paris on August 24, 1804. Later, Gay-Lussac made another flight by himself and ascended to 23,000 feet, setting a record that held for 50 years. Until September 5, 1862, two Englishmen, Henry Coxwell and James Glaisher, reached the range of 30,000 feet using a hydrogen balloon with a capacity of 90,000 cubic feet. During the flight, they suffered from the symptoms of impaired visions, speech disorder, breath difficulty and even unconsciousness, but luckily survived the extreme oxygen deprivation of an altitude higher than anyone had flown before without breathing apparatus. Both of them made several more flights but never so high again. Over their 27 flights, they conducted systematic scientific measurements on the atmosphere, such as air temperature, moisture, electricity and the oxygen levels at different altitude and even determined types, heights, density and thickness of clouds.

In the early 1870s, the French physiologist Paul Bert, also known as the “Father of Aviation Medicine”, built the first low-pressure and airtight chamber, in which the atmospheric pressure could be varied to simulate any altitude, for the balloonists to learn how to use oxygen to protect themselves at high altitudes.

It had been demonstrated by many high-altitude flights the importance of using oxygen masks rather than depending on self-administration of oxygen when the balloonist felt he needed it. The last men of the era to dare altitudes over 30,000 feet were Herr Berson and Professor Suring of the Prussian Meteorological Institute, who ascended to 35,500 feet in 1901, a record that stood until 1931 when Auguste Piccard of Switzerland set a new record.

At the end of the 19th century, unmanned meteorological research balloons started to be used to probe the upper atmosphere. The first meteorological balloon sondes were flown in France in 1892. They were several thousand cubic feet, and carried barometers, thermometers and hygrometers to record pressure, temperature and moisture data from the upper atmosphere. The balloons expanded and ascended as the air became thinner and the pressure dropped; meanwhile the lifting gas in the balloons exited through an opening at the base. At the end of the day, the balloons slowly descended as the lifting gas cooled and took up less space. One big problem is that the meteorologists had to wait until the balloon had descended all the way to Earth to retrieve their instruments, which often had drifted up to hundreds of miles from their launch point. The problem of drifting balloons and retrieval of instruments was solved by the German meteorologist Richard Assmann who introduced closed rubber balloons that would burst when they reached a particular altitude, and then the instruments dropped to earth by parachute in location much closer to the launch site. In 1899, the meteorologist Leon Teisserenc de Bort discovered the stratosphere, the zone between 33,000 and 66,000 feet above the Earth's surface where temperatures remain constant.

1.1.4 Development of stratospheric balloons in 20th century

Since the 20th century, stratospheric balloons have played an important role for scientific research in various fields including meteorology, astrophysics, geophysics and space technology. They could provide a stable instrument platform free from the vibration and the electrical interference generated by aircraft engines. They could also measure atmospheric and cosmic conditions without atmospheric interference by climbing above most of the Earth's atmosphere. The flight altitude ranging from 65,000 to 150,000 ft is either too high for aircrafts to reach and too low for satellite to orbit, or only quickly passed through by rockets. Balloons are considered the only long-duration carrier in the stratosphere.

Development of stratospheric balloons in 20th century can be divided into two phases: pre and post World War II [35]. The separation is because before World War II balloons were made of rubber, while after World War II polyethylene plastic balloons became available and demonstrated their superiority over rubberized balloons for high-altitude flights.

1.1.4.1 Before World War II

On August 7, 1912, Austrian physicist Victor Hess took three electroscopes up to 16,000 feet in an open balloon basket and accidentally discovered high-energy particles not seen on the surface of the Earth, which were named "cosmic rays" in 1936 by physicist Robert Millikan of Caltech. In 1927, aeronaut Captain

Hawthorne Gray, of the U.S. Army Air Corps, ventured into the stratosphere, and tested high-altitude clothing, oxygen systems, and instruments as well as set a new record of 42,000 feet. But unluckily he died on his third high-altitude flight in an open basket. Gray's death attracted people to centralize the problem that it was lethal to fly above 40,000 feet without a pressure garment or the protection of a pressurized vessel because a person's lungs cannot function and gases begin to bubble out of the blood.

Using an apparatus developed by the Germans for use in submarines during World War I, Auguste Piccard built a pressurized aluminum gondola sphere 82 inches in diameter that weighed 300 pounds. The apparatus released pure oxygen into the cabin while scrubbing and recirculating cabin air by filtering it through alkali. He also solved the problem of the lifting gas of the balloon leaking away as it expanded during ascent by using a balloon envelope five times larger than necessary to get off the ground. The lifting gas would remain inside the balloon envelope as it expanded, giving it enough lift to return safely to Earth as the gas cooled at night. In 1932, Auguste Piccard and Max Cosyns soared into the stratosphere in a balloon that included a gondola and set a new altitude record of 53,152 feet. Jean Piccard, Auguste Piccard's twin brother, led a research team to fly *Century of Progress* to a record height of 61,000 feet on November 20, 1933. The balloon carried two instruments to measure how gas conducted cosmic rays, a cosmic ray telescope, a polariscope to study the polarization of light at high altitudes, fruit flies to study genetic mutations for the U.S. Department of Agriculture, and an infrared camera to study the ozone layer.

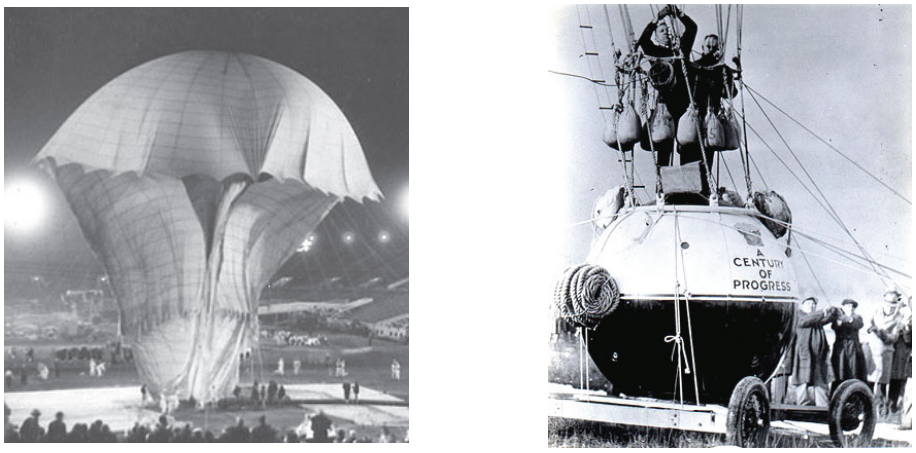

Figure 1.3: (a) Inflation of "Century of Progress" balloon before launch (b) Pressurized aluminum gondola (www.centennialofflight.gov).

In the 1930s, real time atmospheric data were obtained from unmanned balloons into the upper atmosphere with the newly developed radiosonde, a small, radio transmitter that broadcasts or radios measurements from a group of instruments, was developed. The radiosonde transmits data to Earth while measuring humidity, temperature, and pressure conditions. On November 10, 1935, *Explorer II*, with an envelope of

3,700,000 cubic feet, set a world altitude record by reaching 72,395 feet; this record stood for the next 21 years. The enormous and heavy balloon envelopes had clearly reached the limits of rubberized fabric balloon technology.

1.1.4.2 After World War II

During the worldwide depression of the 1930s, Jean Piccard teamed with physicist John Ackerman at the University of Minnesota to experiment with plastic film balloons. At the time, the only plastic available was cellophane, which tended to crack during cold weather inflations. Most research stopped during World War II. After the war, Piccard returned to work with Otto Winzen to find a suitable plastic for their balloons, and they finally decided on polyethylene and then worked on how to manufacture plastic balloons. From 1947 on, polyethylene plastic balloons became capable of lofting instrument payloads to altitudes of more than 100,000 feet. These balloons, which allow researchers to conduct scientific experiments above 99 percent of the Earth's atmospheric mass to measure atmospheric and cosmic effects without interference, demonstrated their superiority over natural or synthetic rubber balloons for high-altitude flights. Cosmic ray physicists were the first to use these new plastic balloons.

In 1950 Otto Winzen patented the natural shape polyethylene balloon. These balloons (vented to the atmosphere) with integral load tapes could carry heavy payloads to around 100,000 feet and played a significant role in paving the way for the space flight program. The advent of the first zero-pressure balloons made of thin polyethylene foil symbolizes the beginning of modern scientific ballooning. The shape of the zero-pressure balloon is obtained from the "natural shape" assumption [48] that the gas bubble confining force system acts in the meridional direction only. The balloon is lobed and open at the bottom, like a hot-air balloon. It is partially filled with lighter-than-air gas at launch. The differential pressure increases and so the balloon expands as it ascends. When it reaches its assigned altitude, the expanding gas fills the envelope and an automatic valve is activated so that the balloon can maintain the altitude as it travels horizontally. The launch of a zero-pressure balloon is shown in Figure 1.4.

High-altitude research balloons carrying science instruments ranging in mass from a few kilograms to more than 1000 kg have been flown for periods of 1-2 days since the 1950s. In the 1990s NASA increased the flight duration to 10-20 days by conducted launches in Antarctica summer when not much ballasting is necessary due to the lack of day night cycles. The development of manufacturing thinner polyethylene film LLDPE (Linear Low Density Polyethylene) with higher tensile strength and better impact resistance than the previously used LDPE, made it possible to construct large-size balloons capable of maintaining their float altitude over the polar regions for extended durations, e.g., up to a new LDB flight record set by a 39.2 mcf (million cubic feet) zero pressure balloon carrying the Cosmic Ray Energetic and Mass (CREAM) experiment circling Antarctica three times for 42 days in 2005. However, the balloon are only able to maintain the float altitude for a few days at mid-latitudes. The reason is that the internal gas is periodically heated and cooled during the day-and night cycle, leading to volume changes. During daylight, when the balloon envelope and

the lifting gas are heated, excess gas is vented through the ducts. At night, when the gas cools and the volume of the balloon decreases, ballast is dropped to maintain altitude, The number of diurnal cycles limits zero-pressure balloons to mid-latitude flights of a few days due to ballast limitations.

(a) (b)

Figure 1.4: Launch of zero-pressure balloon: (a) Release of balloon (b) Ascending balloon (courtesy of NASA).

One way to avoid carrying significant ballast is to design a balloon that can hold enough gas to maintain a positive differential pressure at night and is strong enough to hold the overpressure caused by solar heating during the day. Thus, by reducing the volume variation over diurnal cycles, altitude excursions will be reduced and less ballast will be required during the life of the mission. This approach leads to a design that has come to be known as the *superpressure balloon*. It has an enclosed envelope where the daytime differential pressure is set sufficiently high that at night there is still some residual pressure to keep the volume unchanged. The challenge of designing the superpressure balloon system is to design it with sufficient strength to withstand the large forces generated in the shell of the balloon and of the attachment points for the payload [52].

In the mid 1950s, the Air Force Cambridge Research Laboratory (AFCRL) experimented with polyester film cylinder superpressure balloons. The cylindrical shape minimizes the circumferential stresses in the shell material while transferring most of the loads to the longitudinal direction. However, the resulting forces at the ends of the gores are so high that the design of the end fitting termination became prohibitive. This rapid expansion in the material requirements with balloon size limited this type of design to very small balloons.

A new era in superpressure balloon design began with the introduction of spherical balloons in the early 1960s. The balloons were made from mylar, a biaxially oriented polyester film with a high tensile strength and chemical stability. Spherical balloons generally carry the loads globally in the balloon material. The shells of these balloons were fabricated with precisely cut gores which were joined at their edges with adhesive tape, as shown in Figure 1.5. The process of applying the adhesive tape required precision equal to that

of the gore cutting process. They were used extensively in 1970s for global stratospheric wind circulation studies. In the Global Horizontal Sounding Techniques (GHOST) project, as a result of the AFCRL program, spherical balloons fulfilled the long-time goal of atmospheric scientists to have a semipermanent platform floating high in the atmosphere. One GHOST balloon set a record by remaining in orbit for 744 days, circling Earth 63 times.

The main advantage of the superpressure balloon is the possibility of long-duration flights which can circumnavigate the globe. Small superpressure balloons 4 m in diameter have been released in the Southern Hemisphere, and some have remained aloft for over a year. Balloons having diameters of over 30 m have been flown with limited results. The main problem with spherical superpressure balloons is that the inflation pressure which is needed to preserve the spherical shape may impose unacceptably high stress due to low curvature and the local force due to attachment of the payload. The required robustness of fabrication along with the limitations of the materials also limit the payload capability. The required skin strength growing approximately with the cube root of the volume of the lifting gas makes the design difficult to scale up, which has limited this type of superpressure balloons to rather small sizes.

Figure 1.5: Spherical superpressure balloon [52]

In response to the growing needs of the scientific community, a pumpkin-shaped superpressure balloon capable of maintaining high altitudes, long duration flights with a heavy payload comparable to current zero-pressure balloons is currently being developed, see Figure 1.6. Pumpkin superpressure balloons have been developed over the years. The pumpkin shape design was first considered by G. I. Taylor who used a rubber weather balloon surrounded by strings to validate the parachute shape in 1919. As awareness grew that this envelope material would at best marginally meet the design goal, a novel design that relies on tendons to provide the global pressure-confining strength and requires of the skin only to carry the pressure load to the adjacent tendons was investigated. This is exactly a “natural shape” configuration design and this balloon design concept was studied by Smalley. In 1970, Smalley introduced the “e-balloon”,

a prototype of the pumpkin balloon, which used glass fiber tapes and whose gores could stretch in both meridional and circumferential directions. He also used the term pumpkin balloon, probably because that it approximates the shape of an oblate spheroid. Nott was the first to construct a full size pumpkin balloon, named Endeavour, in 1984 to circumnavigate the world. In 2008, the most successful flight of the entire NASA ULDB development program, Flight 591NT, even broke the previous endurance record of 42 days set by a zero pressure balloon in 2005. This balloon had a size of 7 mcf and was made of 200 gores measuring 82.6 m in diameter, and 51.7 m tall when fully inflated and pressurized. It was designed for a maximum differential pressure of 125 Pa. The balloon was launched in Antarctica on December 28, 2008, deployed at an altitude of 33.69 km and reached float altitude of 33.87 km that was 2 hours and 42 minutes after launched. The balloon performed flawlessly for the next 54 days, completing three circumnavigations of the entire continent.

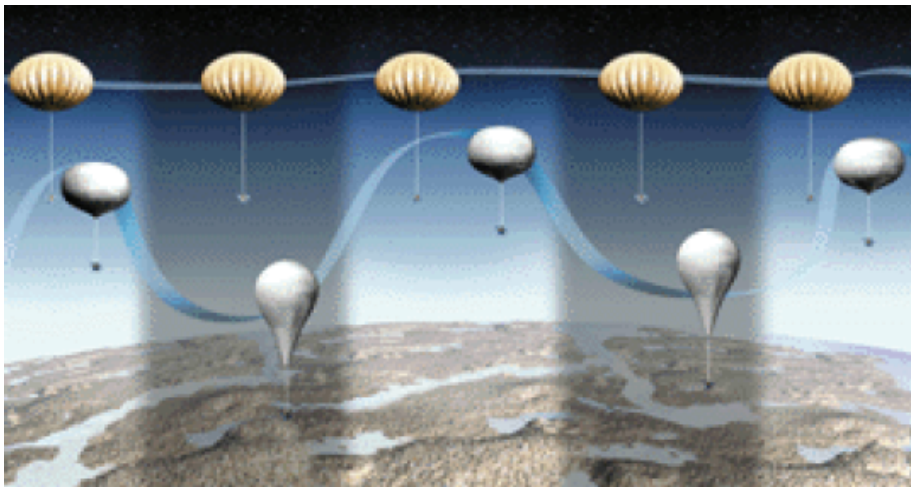

Figure 1.6: Altitude stability of superpressure balloon (top) versus zero pressure balloons (bottom)(sites.wff.nasa.gov).

1.2 NASA superpressure balloon program

The National Aeronautics and Space Administration (NASA) Balloon Program provides support to the scientific community with enhanced capabilities across a spectrum of balloon related disciplines, including cosmic and heliospheric physics, plasma physics, solar physics, high energy astrophysics, infrared astronomy, and upper atmospheric research. The Wallops Flight Facility (WFF) located at Wallops Island, a division of NASA's Goddard Space Flight Center (GSFC), manages NASA's scientific balloon program for the Science Mission Directorate.

Currently there are three classes of balloon missions supported by the Balloon Program [50]. They are: (1) Conventional, (2) Long Duration (LDB) and (3) Ultra-Long Duration (ULDB), see Table 1.1. In

the conventional missions, the flights are usually 8-48 hour long using conventional zero-pressure balloons and ballasting to maintain altitude at night. The Long Duration Balloon (LDB) [21] continues to be a prominent element of the program with a mission model of a two-flight campaign in the Northern and Southern Hemispheres per year during the local summer at the time of constant daylight. These missions use zero-pressure balloons with polar and mid-latitude LDB capabilities as on-going operational elements of the flight program. In the mid 1990s, NASA started the Ultra Long Duration Balloon (ULDB) project [13] for the development of a general purpose platform that can carry payloads of several tons to altitudes over 30 km above 99% of the Earth's atmosphere for up to 100 days. Superpressure balloons floated at constant altitudes by remaining pressurized at all times to maintain a constant volume subject to the typical temperature variations during day and night cycles, and thus fulfilled the requirements of ULDB.

Table 1.1: NASA balloon program capability

Classes of missions	Conventional	LDB	ULDB
Duration	2 hours to 3 days	Up to 41 days	Up to 100 days
Flight opportunities	16 per year	3-6 per year	1 per year
Suspended capability	1650-8000 lbs		6000 lbs
Float altitude	Up to 160,000 ft		Up to 110,000 ft
Launch locations	Fort summer, NM; Palestine, TX; Alice Springs, Australia	Antarctica; Kiruna, Sweden; Alice Springs, Australia	

The initial ULDB superpressure balloons were designed to a spherical shape, similar to the GHOST balloons of the 1970s. No meridional load tapes were used and the stresses were carried by the film; a concentrated payload was attached at the base, which led to great difficulties in early flight tests. The pumpkin shape superpressure balloon concept was adopted for the ULDB design when advantages over a spherical shape design were convincingly demonstrated at the end of 1998. Such advantages include: (1) suspending the heavy payload from the bottom apex does introduce high membrane stresses; (2) it has a favorable self-weight to volume ratio to scale up the size of pumpkin balloons.

The main characteristic of the pumpkin balloon, as shown in Figure 1.7, is to form high curvature lobes by constraining thin polyethylene film bulging between stiff load-carrying PBO tendons, which are sealed into polyethylene pockets all the way along the seams between the neighboring lobes. It allows a clear separation of the load-transferring functions of the major structural elements of the pneumatic envelope, the tendons and the film. The film essentially provides a gas barrier and transfers only the local pressure load to the tendons, thereby minimizing the strength requirement on the film. The efficiency of the pumpkin balloon design scheme depends on allowing the skin to bulge with a small bulge radius between the tendons. This bulging requires excess in skin material beyond what is called minimal enclosure. Such excess can promote the existence of stable equilibria other than the design shape, which assumes cyclic symmetry of the full inflated and pressurized balloon. However, the existence of undesired stable equilibrium states has been observed and should be avoided as they are associated with higher local stress than those predicted for

cyclically symmetric configurations. The successful design of superpressure pumpkin balloons has to ensure proper deployment into a cyclically symmetrical form and the maintenance of this shape throughout the service life.

Figure 1.7: Pumpkin superpressure balloon for high-altitude long-duration scientific flight (courtesy of NASA).

1.2.1 Launch of partially inflated balloons

Low-altitude balloons, as commonly seen, are fully inflated with lighter-than-air gas at the ground level. By contrast, large scientific superpressure balloons for high-altitude missions are partially inflated with gas before launch. Their ascent shapes can be characterized by the formation of lobes surrounding the gas bubble, commonly known as "natural shape". The stresses in the transverse direction are very small compared to the stresses in the meridional direction which concentrate in the load tapes, leading to the natural shape. The differential pressure and skin weight lead to the variation of natural shapes, as illustrated in Figures 1.8. The shape on the far left is called "pumpkin" with bulges; even more pressure will not change this basic shape once it has been established. The balloon shrinks in size when reducing the bottom pressure, and the cone angle at the bottom decreases from a flat angle as well. The shape on the far right has the same scale shape and zero cone angle, with a "roped" section of uninflated balloon below the vertical point.

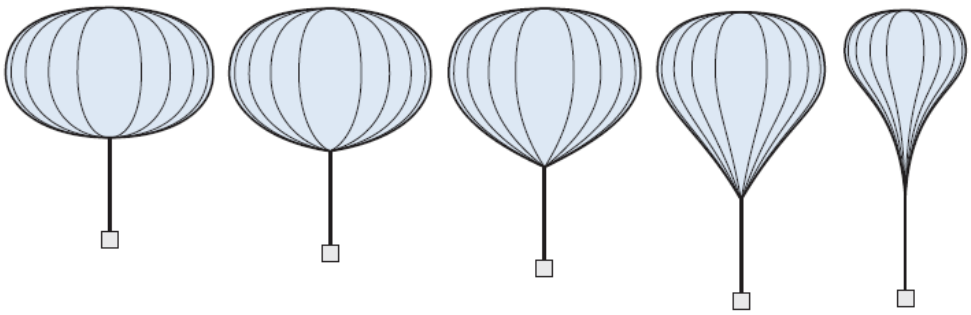

Figure 1.8: Spectrum of axi-symmetric natural balloon shapes (courtesy of Rodger Farley).

In reality, as shown in Figures 1.9, the balloon envelope collapses in the lower part and folds of excess material are formed when it is partially inflated. As the balloon rises, the balloon envelope expands with the reduced surrounding atmosphere pressure. When it reaches the float altitude, the balloon envelope is inflated to the pumpkin shape and maintain a constant volume until gas leakage gradually brings it down. A superpressure balloon is essentially a constant volume system, so the strength of the balloon skin must be sufficient to withstand the pressure created by the exposure of the balloon to solar radiation during the day, and still remain pressurized at night after the gas has cooled. The reason for inflating the balloon with an appropriate mass of gas is to maintain a sufficient differential pressure, which should remain within the strength limit of the balloon structure.

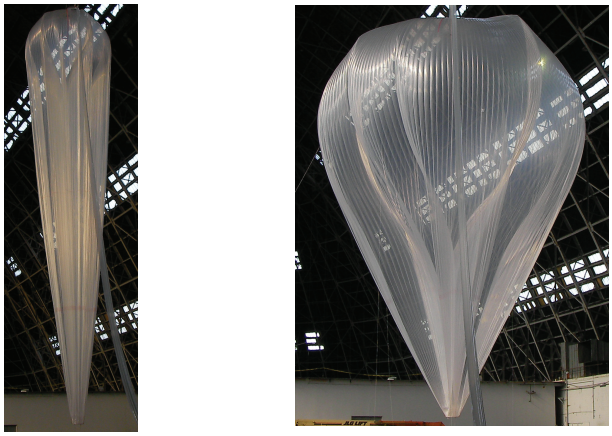

(a) (b)

Figure 1.9: ULDB indoor launch and inflation test: (a) inflated balloon with small portion of gas (b) inflated balloon with large portion of gas (courtesy of NASA).

1.3 Motivation and scope

The lobed shape of superpressure balloons, chosen for its structural efficiency, has led to complications during deployment: several balloons did not deploy into the expected, cyclically symmetrical equilibrium configuration, but instead settled into unexpected asymmetric shapes. Incomplete deployment occurred during the 555NT test flight in Sweden and a characteristic S-cleft, i.e. a single non-meridional cleft spanning from top to bottom of the balloon and involving several lobes, was observed, see Figure 1.10.

Extensive clefting is a regular feature of partially inflated balloons during launch and ascent and yet some balloons remain clefted when they are fully pressurized and others don't. Highly lobed balloon designs achieve lower film stress and yet are more prone to clefting. The first goal of this thesis is to establish a computational clefting test that can be applied to any given balloon design.

The ULDB superpressure balloon is made of a particular type of LLDPE (linear low density polythene)

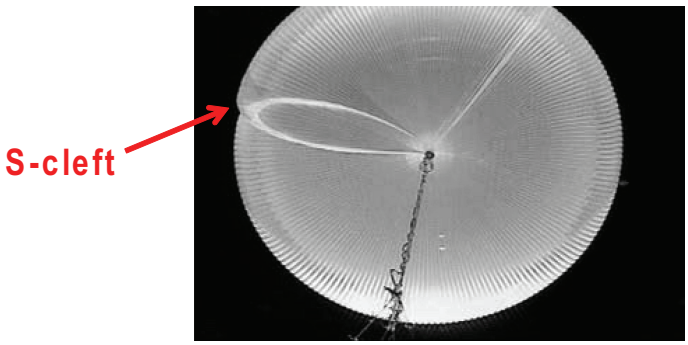

Figure 1.10: S-cleft observed during Sweden flight 555NT (courtesy of NASA BPO).

film, known as StratoFilm 420, which has high tensile strength and impact resistance. It remains ductile at low temperature and exhibits both anisotropy and visco-elasticity. Generally the film in a deployed balloon is under biaxial stress; however during deployment, wrinkled regions subject to uniaxial stress distribution develop in the balloon at low pressure. So far little is known about wrinkles in anisotropic viscoelastic membranes and how these combined effects will influence the deployment of superpressure balloons. Also vicoelastic simulations that require the computation of the convolution integral step by step are numerically so expensive that they pose great challenges to the finite element implementation of complex balloon structures. Therefore the second goal of the thesis is to develop an approximate method that is accurate in capturing the behavior of a real plastic film in a finite element simulation within affordable computational capabilities.

Finally, the third goal is the formulation of a cleft factor (CF) with constant-stress (CS) design parameters of superpressure balloons. the overall shape of pumpkin balloons can be described by Taylor's curve, and the cross-sectional shapes of the lobes are essentially circular arcs. In NASA's early phases, two typical cutting patterns for the lobes were considered, the so-called constant-angle (CA) and constant-radius (CR) cutting patterns. Since these two cutting patterns were derived from engineering intuition, it seems likely that better designs can be obtained from a mathematical optimization approach. The constant-stress (CS) design concept optimizes the flat cutting pattern to be fully stressed for a given design stress constraint, which defines a family of superpressure balloons for optimal design. It would facilitate NASA engineers to be able to predict S-clefts with a simple analytical formula without carrying out many expensive clefting tests and also analyze the sensitivity of design parameters to clefting.

1.4 Layout of dissertation

This dissertation consists of six chapters. The contents of the following are organized as follows:

Chapter 2 contains a comprehensive review of research papers dealing with superpressure design, incomplete deployment of pumpkin balloons, viscoelastic material theory and wrinkling of membranes.

Chapter 3 presents a simplified simulation technique for orthotropic viscoelastic membranes. The method

is based on a modification of the material stiffness matrix to incorporate the effects of orthotropic wrinkling and viscoelasticity. This wrinkling model has been validated by comparison with a published solution for the case of a time-independent isotropic membrane under simple shear. Experimental test on balloon film, StratoFilm 420, under simple shear are also carried out, including loading and unloading, and the experimental results are compared with ABAQUS/Explicit simulations.

Chapter 4 describes deflation and inflation simulations of superpressure balloons. Two different designs of NASA superpressure balloons have been investigated to validate the prediction of S-Clefts: a flat-facet balloon and a highly lobed balloon.

Chapter 5 presents a perturbation method to artificially break the symmetry of a balloon, seed a clefting perturbation and finally determine the equilibrium shape of the balloon. The clefting test is applied to three 27 m diameter superpressure balloons that have been tested indoors by NASA.

Chapter 6 employs dimensional analysis to establish a simple analytical model as indicator of tendency to S-cleft. And sensitivity study of design parameters to clefting is also analyzed.

Finally, Chapter 7 discusses the results of the preceding chapters.

Chapter 2

Background and literature review

This chapter starts with an overview of pumpkin balloon structures, materials, and designs. Then it presents a literature review of a major problem with pumpkin balloons, incomplete deployment due to an excess of hoop material and the resulting formation of S-clefts. Afterwards linear viscoelastic theory is introduced, extended to nonlinear and biaxial models, and a creep model for the balloon film StratoFilm 420 is presented. The final part is a brief review of membrane wrinkling theory.

2.1 Design of pumpkin balloons

The NASA superpressure balloon is a particular type of tension structure consisting of three major components: the balloon hull, high strength and stiffness tendons and end fittings at the top and bottom apex. A schematic representation of a pumpkin balloon is presented in Figure 2.1. The balloon hull is made of a thin plastic film surface that provides a gas tight cavity and is constrained by many stiff tendons. Between the tendons, the surface bulges out and it is expected that the balloon will take up a symmetric shape, with n identical lobes of large transverse curvature. End fittings terminate both film and tendons and also allow attachment of the payload.

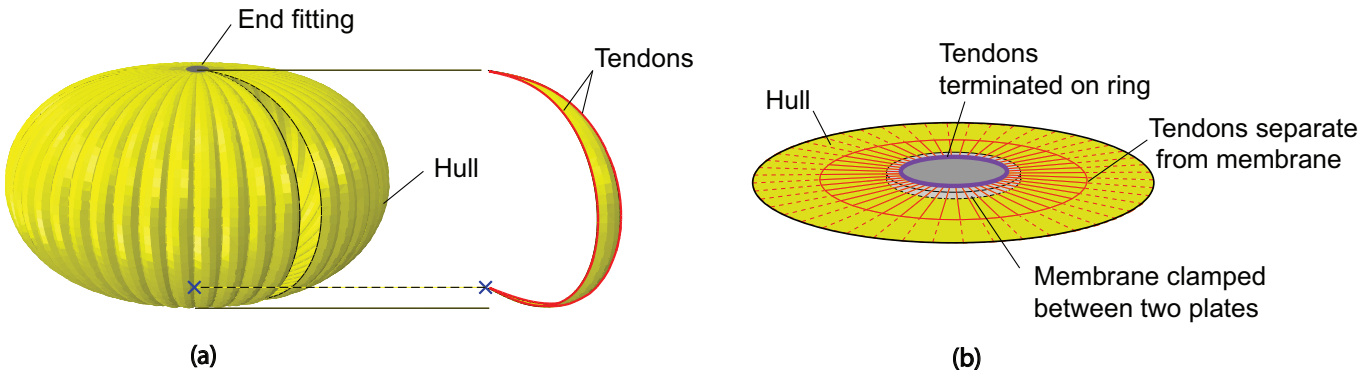

Figure 2.1: Schematic layout of a pumpkin balloon with 48 lobes: (a) components of a pumpkin balloon; (b) detail of end fitting.

2.1.1 Components of a pumpkin balloon

In the past most balloon hulls were made of StratoFilm 372, a 20 micron monolayer film. Current development of coextrusion technology allows to produce a much more uniform film thickness. Blown from the same LLDPE resin as SF 372, the current balloon film consists of three layers with a total thickness of 38 microns and thickness proportions 20/60/20 [43, 44]. The outer layers have an additive that is intended to protect the inner layer from ultraviolet and other radiation damage during flight. The balloon hull is manufactured by welding patterned gores along the edges. Each gore piece is cut from Linear Low Density Polyethylene (LLDPE) film. Two gores are placed on top of each other and a tendon assembly consisting of two polyethylene strips with a tendon welded in is placed on top. A heat sealer moves along the gore's edge to weld the various layers together. The process is repeated for all the gores until the envelope is enclosed.

In the lobed balloon design, the film transfers most of the load to the tendons, thereby minimizing the strength requirements. Tendons are made with a very stiff fiber material called PBO, which has double stiffness than high-modulus Kevlar. This particular material is manufactured by Toyobo Ltd, Japan, under the commercial trade name Zylon®, which provides high tensile strength, high stiffness, creep resistance and low weight. The tendons on ULDB are typically made of 72,000 denier PBO braided cords to attain the desired rope size. PBO however has significant degradation in the tensile strength subject to long-term exposure to visible and ultraviolet light and moisture. Without protection measures one must assume that at least 50% of the strength will diminish over the course of the flight. And in any case the failure mode is by creep-rupture type which further derates the tensile ability.

It is impractical to design a balloon terminating both the gores and tendons into a single point at the top or bottom of the balloon. Therefore a plate shaped structure, the so called "end fitting" is made to provide an attachment for the gores and the tendons as well as for external accessories and payloads. The ends of the gores are clamped and sealed between one ring (inside the balloon) and a circular plate (outside the balloon) made of aluminum. Figure 2.2(a) shows an individual tendon attached to another ring (also outside the balloon) with pins by Brummel splices, a knotting technique in which the end of the rope is braided into itself after forming a loop around a pin. In order to allow the tendons attachment to the end fitting, the tendons are detached from the seams at a certain length before reaching the end fitting. It is noteworthy that separation of the tendons from seams may result in an uneven distribution of local tendon stress. While most tendons are under tension, some are slack in the end fitting region, see Figure 2.2(b).

2.1.2 Profile selection of overall pumpkin balloon surface

The computation of the overall shape of the pumpkin balloon dates back to the calculation of the parachute shape by Taylor in 1919 [55]. His basic idea was to determine the shape which satisfies a particular, prescribed stress distribution by using the equations of equilibrium. To look for the flattest possible shape of parachute, he presumed that the shape occurs at the point of wrinkling, which means that the hoop stress becomes

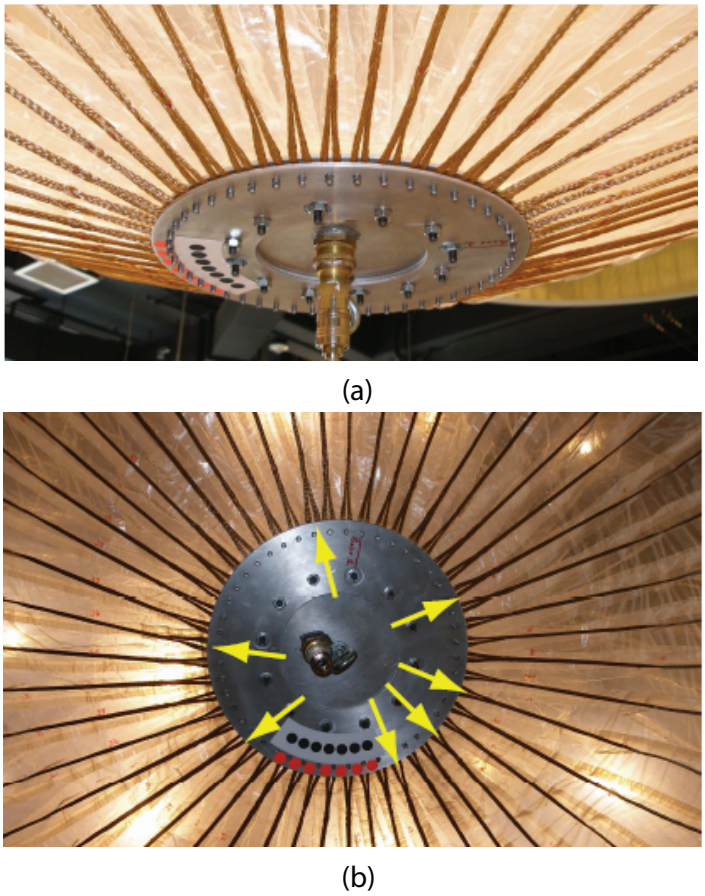

Figure 2.2: (a) End fitting and tendons with Brummel splices; (b) Uneven tendon stresses; arrows mark loose tendons (Courtesy of Gerngross).

zero, see Figure 2.3(a). Further assuming that the differential pressure Δp is uniform, Taylor obtained the following closed-form solution. To verify his theory, he constructed a small pumpkin balloon, shown in Figure 2.3(b).

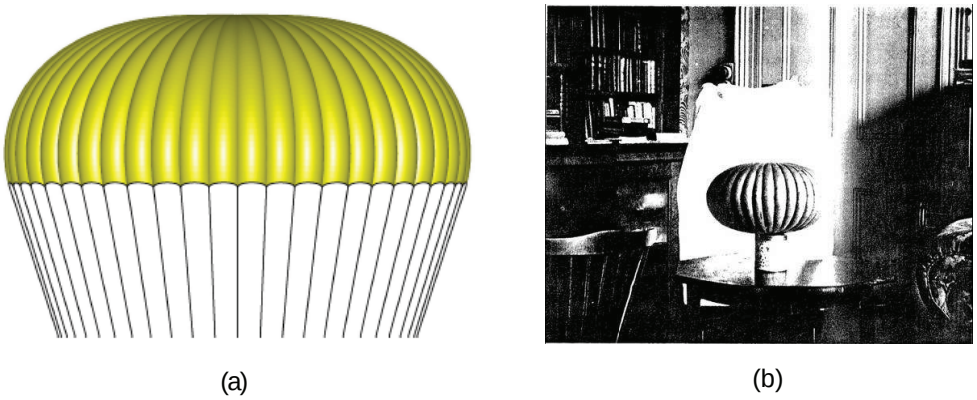

Figure 2.3: (a) Parachute subjected to a uniform pressure; (b) Taylor's pumpkin balloon model.

The overall pumpkin surface can be represented by rotation of the meridional profile $r(z)$ around the z axis under the coordinate system in Figure 2.5(a).

The meridional profile, $r(z)$ is shown in Figure 2.4. The radius of principal curvature in the meridional direction is r_1 and the second radius of principal curvature is r_2; s represents the arc length in the meridional direction, measured from the apex. The angle ϕ measures the colatitude, while the angle θ measures the longitude. From Figure 2.4(a)

$$r = r_2 \sin \phi \tag{2.1}$$

and the meridional curvature has the standard expression

$$\frac{1}{r_1} = -\frac{d^2r/dz^2}{[1 + (dr/dz)^2]^{\frac{3}{2}}} \tag{2.2}$$

The meridional and hoop tensions per unit length are denoted by N_ϕ and N_θ respectively, the normal pressure is denoted by Δp, and there is no shear for symmetry, see Figure 2.4(b). In general, they are related by the three equations of equilibrium [22]

$$\frac{\partial(r_2 \sin \phi N_\phi)}{\partial \phi} - r_1 \cos \phi N_\theta = 0 \tag{2.3}$$

in the meridional direction,

$$r_1 \frac{\partial N_\theta}{\partial \theta} = 0 \tag{2.4}$$

in the hoop direction, and

$$\frac{N_\phi}{r_1} + \frac{N_\theta}{r_2} = \Delta p \tag{2.5}$$

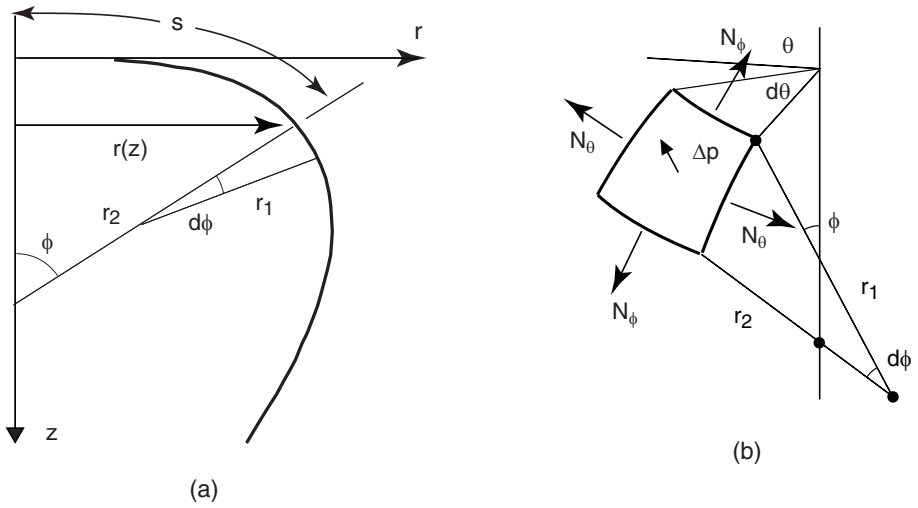

Figure 2.4: (a) Geometry of axisymmetric balloon; (b) equilibrium of infinitesimal element.

along the normal.

Since it has been assumed that the film has no hoop tension

$$N_\theta = 0 \tag{2.6}$$

Hence, Equation 2.4 is satisfied and Equation 2.5 becomes

$$N_\phi = \Delta p r_1 \tag{2.7}$$

Substituting Equation 2.1, Equation 2.6 and Equation 2.7 into Equation 2.3 we get

$$\frac{\partial(rN_\phi)}{\partial\phi} = 0 \tag{2.8}$$

and solving this partial differential equation gives

$$N_\phi = C(\theta)/r \tag{2.9}$$

For symmetry, N_ϕ has to be independent of θ and hence

$$N_\phi = C/r \tag{2.10}$$

where C is called the *stress constant*. It can be seen that there is a singular point at the crown of the balloon, where the above equation gives an infinite N_ϕ.

Substituting Equation 2.7 into Equation 2.10, and then Equation 2.2 for r_1 and rearranging gives the

differential equation governing the profile of the axisymmetric balloon with zero hoop stress

$$\frac{d^2r}{dz^2} + \frac{\Delta p}{C} r[1 + (dr/dz)^2]^{\frac{3}{2}} = 0 \tag{2.11}$$

This is an initial value problem because we know in advance only the boundary conditions at the crown, which can be expressed as

$$r(0) = 0, \qquad \left(\frac{dr}{dz}\right)_0 = \infty \tag{2.12}$$

Subject to uniform pressure, Δp=const, analytical solution of the meridian is generally defined by the hoop radius r and vertical distance from the nadir z, which could be respectively expressed as

$$z = \int_0^r \frac{r^2 dr}{\sqrt{r_0^4 - r^4}} \tag{2.13}$$

$$r = r_0 cn(u) \tag{2.14}$$

and

$$z = \frac{r_0}{\sqrt{2}}\{2[E - E(u)] - (K - u)\} \tag{2.15}$$

where

$$u = K - \frac{s\sqrt{2}}{r_0} \tag{2.16}$$

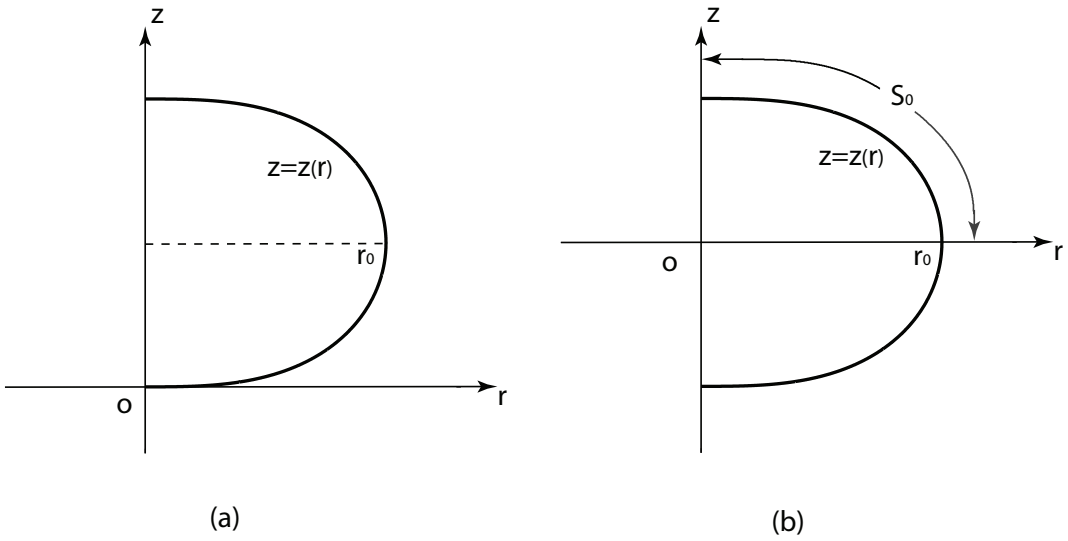

Figure 2.5: (a) Definition of coordinate system by Taylor; (b) Definition of coordinate system in variation calculus by Paulsen.

Here $cn(u)$ is a Jacobian elliptic function, K and E are the complete elliptic integrals of the first and second kinds respectively, for modulus $1/\sqrt{2}$; K=1.8541 and E=1.3506. s is the meridional arc length

measured from the start point at the origin. z is zero at nadir, and the maximal ratio z/r_0 is 0.5991 at the equator. Matlab provides the functions **ellipj, ellipke and EllipticE** to evaluate the equations above. The resulting curve is called "Taylor's curve".

While a sphere is famous for its maximum volume to surface area ratio of 3/2, pumpkin shape has a greater volume to gore length ratio, 3, than a sphere, which is why filament-wound spacecraft propulsion tanks use this shape. One good example is that surprisingly a balloon made by fusing two circular mylar sheets together at the circumference doesn't take up spherical shape. Paulsen solved the inflated shape of a Mylar balloon by a variational method [37]. He reduced the formfinding of the isotensoid balloon to the following mathematical problem: given deflated radius S_0 of a circular mylar sheet, what will be the shape of the balloon when it is fully inflated? Its mathematical model was set up as follows.

Assuming Mylar does not stretch during inflation, the curve length calculated by integrating inflated radius r from 0 to r_0 is constrained by the original radius S_0 measured on the flat sheet, shown in Figure 2.5(b) after inflation, that is,

$$\int_0^{r_0} \sqrt{1 + z'(r)^2} dr = S_0 \tag{2.17}$$

We will assume that these wrinkles don't affect the volume of the balloon significantly, so the total volume is given by

$$V = 4\pi \int_0^{r_0} r z(r) dr \tag{2.18}$$

Our aim is to find curve $z(r)$ and r_0 such that V is maximized subject to the subsidiary condition from Equation 2.17 and the end point condition $z(r_0) = 0$. Using the calculus of variations, we find such curve

$$z(r) = \int_r^{r_0} \frac{t^2 dt}{\sqrt{r_0^4 - t^4}} \qquad (0 \leqslant r \leqslant r_0) \tag{2.19}$$

and the maximal volume is

$$V = \frac{64\pi^2 S_0^3}{3\Gamma(1/4)^4} \tag{2.20}$$

where $\Gamma(x)$ is defined as Beta integral, and the volume is about $1.2185{S_0}^3$. Paulsen's solution is the same as Taylor's, which proves that the pumpkin shape provides the maximal volume, maximal lift, and thus the highest carrying efficiency for given arc length.

2.1.3 Lobe geometry

Taylor curve is employed to describe the envelope of a pumpkin balloon; however in real balloon design such smooth surface is seldom used. It is necessary to consider a doubly curved surface which will then carry lower surface tension due to the presence of a small principal radius of curvature. Lobed shapes form between neighboring tendons under internal pressure by increasing the width of the flat gores and thus decrease the stresses in the transverse direction.

Figure 2.6(a) shows a lobed shape between adjacent tendons. Assuming that the tendons of the balloon lie on an overall pumpkin surface, the equatorial radius of the balloon is denoted by R_{tendon}. For the case of n lobes, the equatorial subtended angle is $\theta = 2\pi/n$. Also consider the lobe geometry at equator in Figure 2.6(b), where d is the arc length of the lobe, and c the chord length. r_{lobe} is the radius of the circular arc and α is the angle subtended by the lobe.

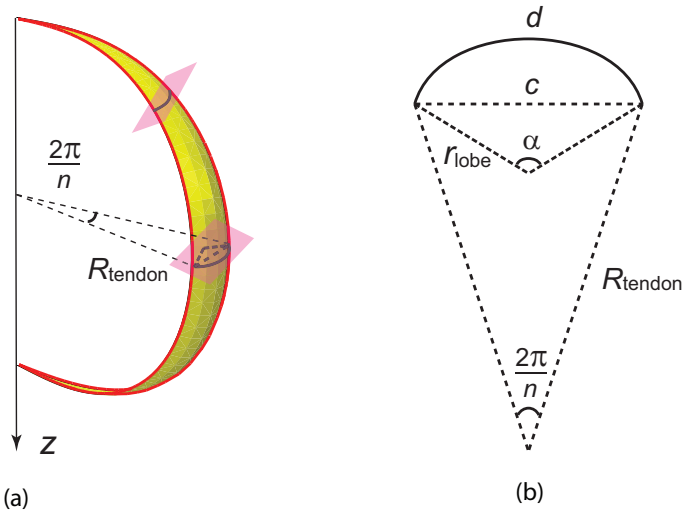

Figure 2.6: (a) Lobed shape between neighboring tendons; (b) Lobe geometry at equator.

It is easy to express the chord length c in terms of R_{tendon} and θ as

$$c = 2R_{tendon} \sin \frac{\pi}{n} \tag{2.21}$$

Also the chord length c can be expressed in terms of r_{lobe} and α as

$$c = 2r_{lobe} \sin \frac{\alpha}{2} \tag{2.22}$$

Combining the above two equations, balloon radius R_{tendon} and lobe radius r_{lobe} are related by

$$r_{lobe} = R_{tendon} \frac{\sin \frac{\pi}{n}}{\sin \frac{\alpha}{2}} \tag{2.23}$$

The profile of the flat gore is often called the "cutting-pattern", which is determined by the geometrical parameters of the lobe, i.e. lobe radius r_{lobe} or bulge angle α. Two particular cutting patterns have been considered for superpressure balloons, the constant-radius (CR) and constant-angle (CA) design meaning either r_{lobe} or α remain constant along the meridian. The arc length of bulged lobe d is given by

$$d = \alpha r_{lobe} \tag{2.24}$$

Substituting Equation 2.23 and 2.24 yields

$$d = \begin{cases} \alpha \frac{R_{tendon} \sin \frac{\pi}{n}}{\sin \frac{\alpha}{2}} & \text{for constant angle (CA) design} \\ 2r_{lobe} \arcsin(\frac{R_{balloon}}{r_{lobe}} \sin \frac{\pi}{n}) & \text{for constant radius (CR) design} \end{cases} \tag{2.25}$$

The key difference between the two designs is that the CA design bulges more towards the apex while the CR design is flatter. Recently, a new design based on more balanced stress distribution, called constant-stress (CS) design, has been explored to optimize the cutting pattern. Pagitz and Pellegrino argued that the critical buckling pressure of an n-fold symmetric superpressure balloons is maximized if the unstressed surface area of the balloon was minimized [34]. Therefore they presented anoptimization algorithm to minimize the unstressed lobe area, subject to a constraint on the maximum value of the von Mises stress in the lobe, for a given differential pressure. It was shown that, compared to current designs, the buckling pressure was increased by up to 300% without increasing the maximum stress in the lobe and also a more uniform stress distribution was obtained for the optimized cutting pattern.

2.2 Incomplete deployment of superpressure balloons

Clefts due to improper deployment of a few lobes were observed in ULDB flight tests. A typical example is S-cleft developed in the second phase IV-A balloon (Flight 517NT, Spring 2003). Many clefts was observed in the launch configuration, and gradually disappeared throughout the ascent phase, and one cleft still remained once the balloon reached maximal altitude, as shown in Figure 2.7.

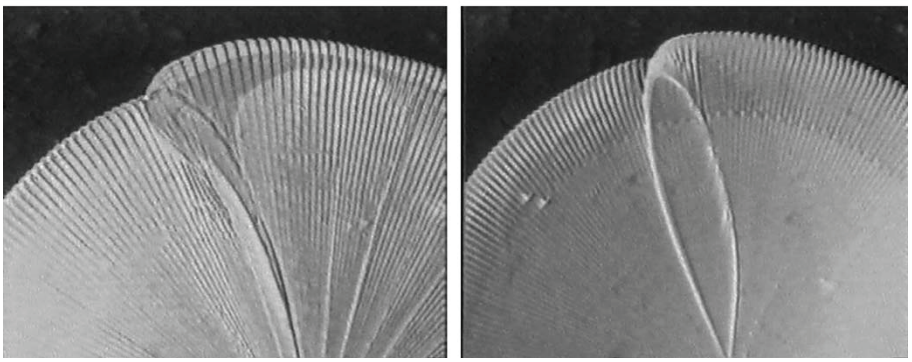

Figure 2.7: Flight 517 cleft: (a) ascent; (b) at maximum altitude [10].

In 2007, a systematic set of indoor inflation experiments on one-third scale models of flight balloons were carried out by the NASA Balloon Program Office [14]. These tests showed indoor balloon tests that a cleft will reappear either in the same location or somewhere else when it is pulled out by applying hoop forces

that are then released. This observation suggests that a balloon with an S-cleft is in a stable equilibrium configuration and hence it seems reasonable to approach clefting as a problem involving a bifurcation, or buckling from the main equilibrium path. Two independent bifurcation approaches have been considered; the first approach aims to find the equilibrium shapes of partially inflated balloons and the second approach computes the buckled asymmetrical shapes of superpressure balloons.

2.2.1 Shapes of partially inflated balloons

After Taylor's first study of pumpkin balloons in 1919, the next notable contribution was made by researchers at University of Minnesota [3] in 1950s, who developed equilibrium equations for an axisymmetric balloon shape called the Σ-shape equations. Σ-shape was named after the parameter Σ appearing in rescaled model equations. Following the general membrane theory, the first-order system of nonlinear ordinary differential equations [7, 5] have the form:

$$(r\sigma_m)\frac{d\theta}{ds} = \sigma_c \cos\theta - rw\sin\theta - rp, \tag{2.26}$$

$$\frac{d(r\sigma_m)}{ds} = \sigma_c \sin\theta + rw\cos\theta, \tag{2.27}$$

$$\frac{dz}{ds} = \cos\theta, \tag{2.28}$$

$$\frac{dr}{ds} = \sin\theta \tag{2.29}$$

where $(z(s), r(s))$ is the generating curve for the axisymmetric balloon shape, s is the meridional arc length measured from the start point, $\sigma_m(s)$ is the meridional stress, $\sigma_c(s)$ is the circumferential or hoop stress, $\theta(s)$ is the angle the tangent makes with the z-axis, and $w(s)$ is the film weight density. $b = g(\rho_{out} - \rho_{in})$ is the specific buoyancy of the lifting gas (uniform over the length of the balloon). The differential pressure at level z is given by $p = b(z + z_0) = bz + p_0$. It is assumed that the film is inextensible and all the tension is carried in the meridional direction and thus $\sigma_c = 0$. We define the total film load in the meridional direction as

$$T = 2\pi r\sigma_m \tag{2.30}$$

Thus the governing differential equations for a natural shape balloon in terms of T are

$$\frac{d\theta}{ds} = -\frac{2\pi r(w\sin\theta + bz + bz_0)}{T}, \tag{2.31}$$

$$\frac{dT}{ds} = 2\pi rw\cos\theta, \tag{2.32}$$

$$\frac{dz}{ds} = \cos\theta, \tag{2.33}$$

$$\frac{dr}{ds} = \sin\theta \tag{2.34}$$

Smalley [49] was the first to use a digital computer to carry out extensive numerical studies based on the Σ-shape model. Two numerical solutions to the equations were discussed by Rand [42]. The first is a "shooting" method solution, where certain variables are assumed at the start of the integration and a check of the final radius and angle is made at the end. If the check is not satisfied, the assumed starting values are changed and the process repeated. The difficulty of this technique is that the equations may become numerically unstable in the "rope" section at the bottom of the balloon. The alternative approach starts from the observation that, regardless of altitude, the apex of the balloon is always fully inflated. Hence the integration starts with an assumed pressure at the apex. As the integration proceeds down the balloon, the circumferential load required to satisfy the equilibrium equations is monitored. This force will become negative when excess material is available. At this point the force is set to zero and the calculation proceeds to generate the "natural shape" with no circumferential stress. Due to the delicate balance between the applied forces and the extent of the integration, the numerical procedure selected was a modified Runge-Kutta technique. Figure 2.8 shows a sequence of results obtained by Rand. Archimedes' principle states that for equilibrium, the balloon must displace an amount of air equal to its weight, hence $W_{tot} = Lift = bV$ where V is the volume of the balloon, W_{tot} is the total weight, and $b = g(\rho_{out} - \rho_{in})$ is the specific buoyancy of the lifting gas. The subscript d indicates a quantity related to the design shape. At float $b = b_d$ and $V = V_d$. When $V < V_d$, equilibrium requires that $bV = b_d V_d$. Thus b is adjusted so that $b = b_d V_d / V$ and hence this parameter describes the ascent shape.

Baginski [8, 4, 9] solved the problem of determining the equilibrium shape of a strained balloon using the principle of minimum total potential energy. The total potential energy ε of a strained, inflated balloon in a configuration φ is given by

$$f(S) = \varepsilon_P + \varepsilon_{\text{film}} + \varepsilon_{\text{t}} + \varepsilon_{\text{top}} + S^*_{\text{t}} + S^*_{\text{film}} \tag{2.35}$$

where ε_P is the hydrostatic pressure potential of the lifting gas, $\varepsilon_{\text{film}}$ the gravitational potential energy of the film, ε_{t} the gravitational potential energy of the load tendons, ε_{top} the gravitational potential energy of the apex fitting, S^*_{t} the relaxed strain energy of the tendons, and S^*_{film} the relaxed strain energy of film. Then, the following problem is defined

$$\min \quad f(S) \qquad \text{where } S \in C_s \tag{2.36}$$

where C_s denotes the class of feasible balloon shapes. Any boundary conditions or symmetry conditions that are to be imposed on the particular shapes of interest can be built into C_s. $S(V, n, r_g)$ denotes a balloon with volume V, n lobes and r_g gores per lobe. The total number of gores, n_g, can be expressed as $n_g = r_g n$. As an example of the shapes computed by Baginski, a partially inflated balloon with periodic lobes $S(0.4V_d, 9, 3)$

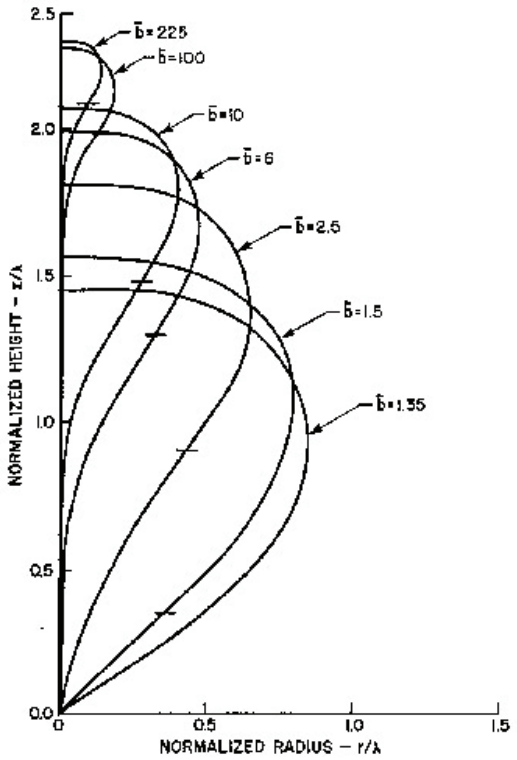

Figure 2.8: Natural shape balloons, $\overline{b} = V_d/V$ [42].

is shown in Figure 2.9.

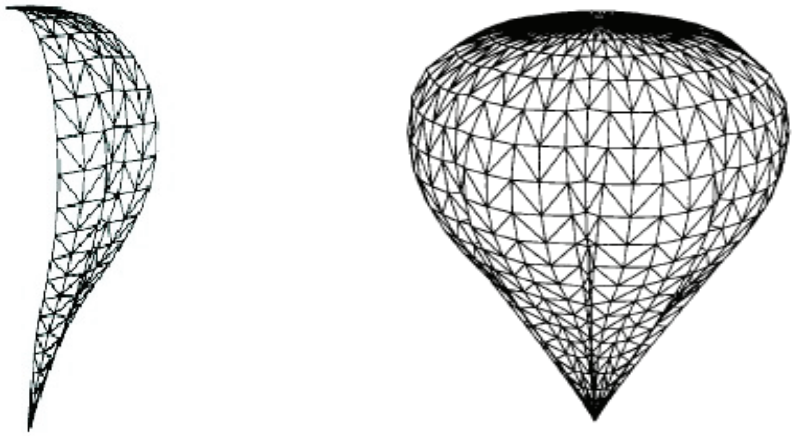

Figure 2.9: 27-gore pumpkin balloon $S(0.4V_d, 9, 3)$: (a) 3-gore lobe from S (b) Balloon configuration S [4].

2.2.2 Stability of cyclically symmetric balloons

Another approach has focused on the overall geometric stability of cyclically symmetric balloons subject to internal pressure. Alexander [2] analyzed the inflation of initially spherical neoprene balloons both analytically and experimentally to understand tensile instabilities at very large deformations. Using a constitutive relation for elastic incompressible rubber-like material, an investigation of dimensionless pressure p^* versus dimensionless radius r^* derived by minimization of total potential energy revealed the existence of different stable or unstable equilibrium states for a given pressure, as shown in Figure 2.10.

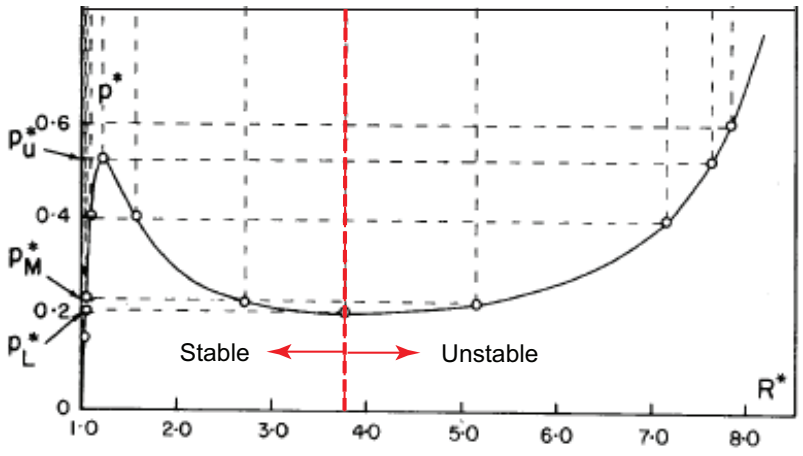

Figure 2.10: Pressure versus radius for inflation of a spherical neoprene balloon [2].

Chater and Hutchinson [15] investigated the inflation of a long cylindrical balloon in which a bulge propagated down the length of the balloon. As shown in Figure 2.11, at the starting inflation, a bulge first localized at one weak end of the balloon when the peak pressure was attained. With continued inflation, the pressure falls to a constant level as the bulge slowly propagated along the balloon while the radii of the bulged and unbulged section didn't change through the quasi-static propagation. The general characteristic of this instability mode is a substantial barrier to initial bulging and reduced load during spreading.

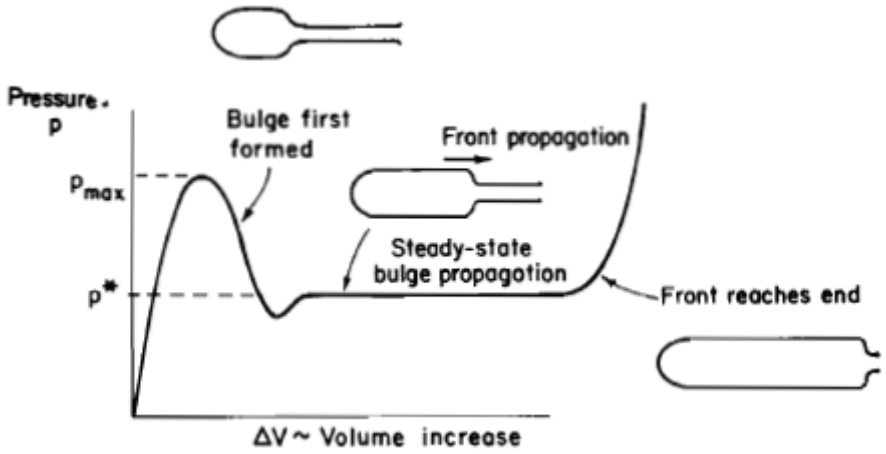

Figure 2.11: Pressure versus volume for a cylindrical balloon [15].

In 1984, during the race for the first balloon circumnavigation of the world, Nott proposed a design of a constant bulge angle pumpkin balloon called Endeavour, see Figure 2.12(a). This balloon had 64 gores and the gores were originally designed to have a full 180° radius between the load tapes. When the balloon was first inflated, it had extra material between the load tapes and so it remained heavily asymmetrical even after increasing the differential pressure after inflation. This global shape can be seen in Figure 2.12(b). Removal of two gores and reinflation diminished but didn't eliminate the lack of symmetry; full deployment occurred if four gores had been removed. But even so, a slightly buckled shape was observed when the skin was stretched under increased pressure.

To explain the behavior of the fully inflated Endeavour in terms of its stability, Calladine [12] ignored strain energy contribution to the total potential energy, and converted the buckling of a balloon to a study of the variation of volume enclosed by a pumpkin balloon. He showed that this volume increases for certain small amplitude inextensible deformations of the balloon if the number of lobes and bulge are sufficient large. This led to a stability criterion for pumpkin balloons with constant-angle (CA) designs based on an analogy between the geometrical stiffness of a lobe and the elastic bending stiffness of an Euler strut. He found that there are two key balloon parameters, the number of lobes, n, and the lobe angle, α (in radians). Balloons for which

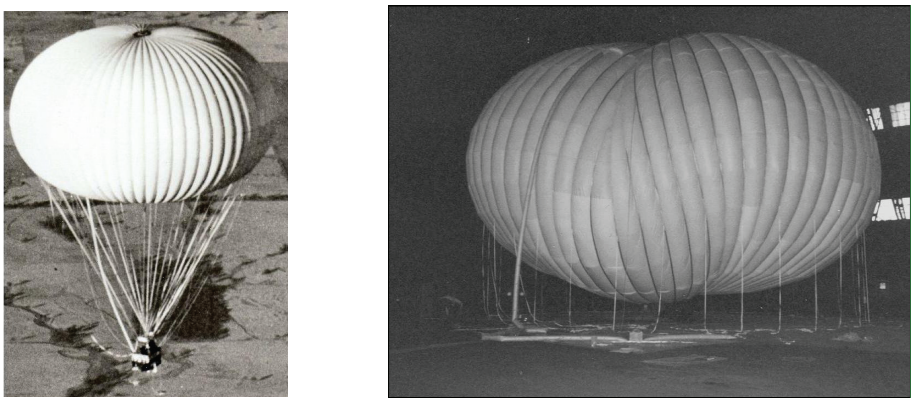

(a) (b)

Figure 2.12: Endeavour pumpkin superpressure balloon: (a) Nott's flight with Endeavour (b) Undesired stable equilibrium state of Endeavour (Courtesy of J. Nott).

$$n\alpha^{2.5} > 34 \tag{2.37}$$

have the property that their volume can be increased by deforming the balloon shape according to a certain inextensional buckling mode, hence they are unstable. From this discovery Calladine explained the behaviour of the Endeavor balloon and Nott's successful design changes. In 2000, Lennon and Pellegrino [26] carried out a semi-analytical study of the variation of the volume enclosed by an inextensible, constant-radius (CR) pumpkin balloon. Different numbers of lobes and amount of bulging were considered. It was found that the volume of these balloons decrease for small deformation but increase for sufficiently large deformation. Hence the balloon was unstable for large perturbations. However, these analytical models are based on assumed buckling modes and neglect the elastic deformation of membrane and tendons.

Calladine's criterion was rearranged as a relationship between the ratio (d/c) and the number of gores, where d is the arc length between adjacent tendons measured along the bulging gore and c is the chord length between the tendons. This relationship was plotted as a curve and compared with experiments [48, 51]. It was inferred that excess gore-with in the "tropics" (using a geographic metaphor) is beneficial to proper deployment, while excess gore width outside this region is definitely detrimental. In addition, constant bulge angle designs require a larger radius at the equator than comparable constant bulge radius designs. Calladine's criterion, based on a simple proxy-problem, was found to be remarkably accurate when compared with the stability results on constant-angle pumpkin balloons, whereas balloons with constant-radius designs have better deployment performance and lie beyond the relationship proposed by him.

Pagitz and Pellegrino [33] exploited the high degree of symmetry of pumpkin balloons by adopting a closed form symmetry-adapted coordinate system, which provided the tangent stiffness matrix in a very efficient block-diagonal form. Figure 2.13 shows two buckling modes for a 10 m diameter, 145 gore balloon

with lobes of constant radius. It was found that for any chosen balloon there is a power law relation between the critical pressure p_{crit} and the number of lobes n

$$p_{crit} = an^k \tag{2.38}$$

where a and k depend on the cutting pattern and the material parameter.

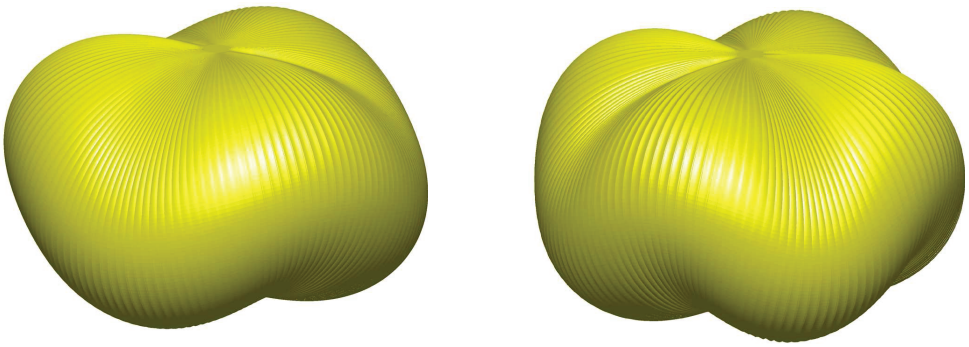

Figure 2.13: Stability modes of a 145-gore constant radius balloon: (a) 3up3down; (b) 4up4down [33].

Xu and Pellegrino [63] predicted the critical pressure and the corresponding buckling modes by eigenvalue analysis using ABAQUS/Standard. The eigenmodes were used as geometric imperfections seeded into the post-buckling analysis. Two different types of geometric imperfections were used: either single critical eigenmode, or linear combination of the first 10 eigenmodes. It was found that by using the single critical eigenmode as imperfection, the balloon deformed into a globally buckled shape whereas a more localized deformed shape can be obtained by introducing the combined eigenmodes. A comparison of balloon configurations obtained from postbuckling analyses applying different geometric imperfections is shown in Figure 2.14.

Baginski [6] analyzed the Hessian (matrix of second derivatives) of the total potential energy f in the form $H_f = D^2 f$, and defined that the corresponding S is unstable if at least one eigenvalue of H_f is negative. Two types of end-fitting boundary conditions, free and fixed top apex, were considered in thin balloon models. A number of parametric studies on constant-stress design balloons were carried out to gauge the susceptibility to deployment. A correlation was observed between incomplete deployment and the number of negative eigenvalues of the Hessian when the boundary constraint at the top apex are released. Two unstable configurations for the 230-gore 14.836 mcf design are presented in Figure 2.15. Note that free top apex system has only two unstable eigenmodes, shapes with two-lobe and three-lobe symmetry, and the fixed top apex system has no unstable modes.

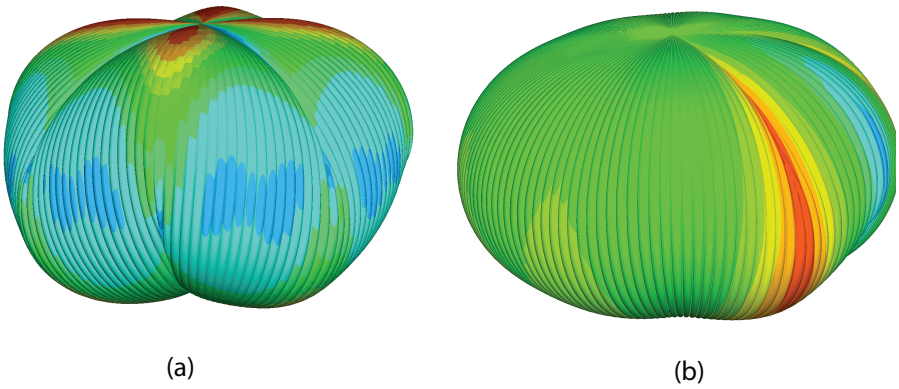

Figure 2.14: Postbuckling analyses on pumpkin balloon: (a) global buckled shape using single critical eigenmode; (b) localized buckled shape using linearly combined eigenmodes [63].

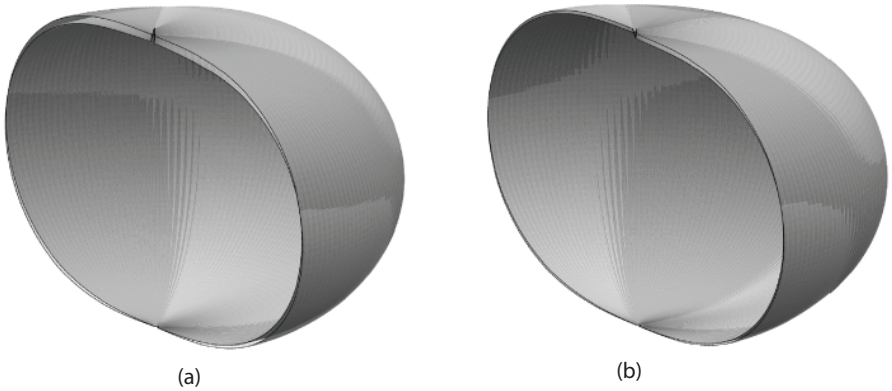

Figure 2.15: Asymmetric equilibrium configurations of a 230-gore 14.836 mcf balloon: (a) two-lobe symmetry (b) three-lobe symmetry [6].

2.3 Review of viscoelastic theory

In the classical theory of linear viscoelasticity [56, 28] the creep compliance D and relaxation modulus E can be obtained from spring and dashpot models. A spring in series with a dashpot is known as the Maxwell model; a spring in parallel with a dashpot is known as the Kelvin-Voigt model. Both models have serious shortcomings. A more realistic model is the Standard Linear Solid model which is either represented by a Maxwell element with an additional spring in parallel or a Kelvin-Voigt element with an additional spring in series.

A more realistic representation of actual viscoelastic behavior is obtained by considering n Kelvin-Voigt elements with one spring in series, which leads to a compliance function expressed as a sum of exponential terms called Prony series

$$D(t) = D_0 + \sum_{i=1}^{n} \Delta D_i (1 - e^{-t/\tau_i}) \tag{2.39}$$

Viscoelastic materials are temperature as well as time dependent but both effects can be combined through the time-temperature superposition principle by considering only the reference temperature T_0 and the reduced time

$$\psi(t) \equiv \int_0^t \frac{d\tau}{a_T(T)} \tag{2.40}$$

where $a_T(T)$ is the temperature shift factor, defined to be 1 at the reference temperature ($a_T(T_0) = 1$).

The compliance master curve, which defines the time-dependent compliance at the reference temperature, can be obtained from a series of uniaxial creep tests. It can be expressed as a combination of an instantaneous part D_0 and a transient part $\Delta D(\psi)$:

$$D(\psi) = D_0 + \Delta D(\psi) \tag{2.41}$$

Here D_0 represents the instantaneous compliance at the reduced time $\psi = 0$ and the transient part $\Delta D(\psi)$ can be represented by the Prony series:

$$\Delta D(\psi) = \sum_{i=1}^{n} \Delta D_i (1 - e^{-\psi/\tau_i}) \tag{2.42}$$

The linear viscoelastic strain at time t, $\epsilon(t)$, is calculated by the convolution integral (also called Boltzman superposition integral)

$$\epsilon(t) = D_0 \sigma(t) + \int_{0^+}^{t} \Delta D(\psi^t - \psi^\tau) \frac{d\sigma(\tau)}{d\tau} d\tau \equiv D(\psi)\sigma(t) \tag{2.43}$$

Experimental studies have shown that this linear model is acceptable at small strains; at larger strains a nonlinear viscoelastic model has to be adopted, where the creep compliance is a function of stress, as well as of time and temperature. Following Schapery [46, 47] this behavior can be captured by introducing an experimentally derived stress-related shift a_σ in the reduced time expression, which kicks in at stresses

higher than a limiting value σ_0. Hence Equation 2.40 for the reduced time is rewritten as

$$\psi(t) \equiv \int_0^t \frac{d\tau}{a_T(T)a_\sigma(\sigma,T)} \tag{2.44}$$

Schapery [46] has adopted a single-integral representation for the strain at time t based on the three nonlinear parameters g_0, g_1 and g_2:

$$\epsilon(t) = g_0 D_0 \sigma(t) + g_1 \int_{0^+}^t \Delta D(\psi^t - \psi^\tau) \frac{dg_2\sigma(\tau)}{d\tau} d\tau \equiv D(\psi) * \sigma(t) \tag{2.45}$$

where the nonlinear parameters are all equal to 1 in the linear viscoelasticity range.

The above uniaxial model has been extended to plane stress loading of a polymeric film by making the assumption that the transient compliance in any direction can be expressed in terms of a constant matrix S_{ij} multiplied by the compliance in a direction of orthotropy of the material, assumed to be known

$$D_{ij} = S_{ij} D_{11} \tag{2.46}$$

where $S_{11} = 1$ by definition. Thus the in-plane compliance matrix $[D]$ can be expanded as

$$\begin{bmatrix} D_{11} & D_{12} & 0 \\ D_{21} & D_{22} & 0 \\ 0 & 0 & D_{66} \end{bmatrix} = D_{11} \begin{bmatrix} S_{11} & S_{12} & 0 \\ S_{21} & S_{22} & 0 \\ 0 & 0 & S_{66} \end{bmatrix} \tag{2.47}$$

The uniaxial stress σ used to calculate all stress-dependent non-linearities in the previous model is then replaced with an effective stress. This is defined as

$$\sigma_{\text{eff}} = \sqrt{\widehat{\sigma_{11}}^2 + 2A_{12}\widehat{\sigma_{11}}\widehat{\sigma_{22}} + A_{22}\widehat{\sigma_{22}}^2 + A_{66}\widehat{\tau_{12}}^2} \tag{2.48}$$

where $\widehat{\sigma_{11}}$ is the normal stress in the one of the directions of material orthotropy, and it is assumed that the uniaxial model has been developed in this particular direction, $\widehat{\sigma_{22}}$ is the normal stress in the other direction of orthotropy, and $\widehat{\tau_{12}}$ is the shear stress. The notation $\widehat{\ }$ denotes components in the directions of orthotropy.

2.4 Wrinkling of membranes

Thin balloon film is prone to wrinkling. The existence and severity of wrinkled regions in balloon film may have adverse effects on its stability hence wrinkling has to be modeled currently if one wishes to predict the stress and displacement within a partly wrinkled membrane surface. If the actual shape and number of wrinkles is of less interest, we may use a membrane model that neglects bending stiffness for a wrinkled structure made of thin film, and a fictitious non-wrinkled surface to describe the average membrane

deformation. The following assumptions are made for the membrane model: (1) no bending stiffness in the film and thus the exact shape of the wrinkles cannot be defined; (2) wrinkling is treated as a two-dimensional plane stress problem; (3) membrane can only carry tension and it will wrinkle once a negative stress appears. A wrinkled region is in a state of uniaxial tension and has no loading capability along the wave direction of the wrinkles.

2.4.1 Review of wrinkling theory

2.4.1.1 Tension field theory

Tension field theory which describes the wrinkled state of membranes, was first introduced in 1929 by Wagner [56], with the primary concern of explaining the behavior of thin metal webs in beams and spars carrying a shear load well after exceeding the buckling load. This theory was further developed by Reissner [45] who introduced *artificial orthotropy* as a numerical trick to derive a compression-free solution for isotropic membranes. Mansfield [27] generalized tension field theory to anisotropic membranes with restricted types of nonlinear stress-strain relationships. He considered a flat membrane of arbitrary shape and stiffness subject to prescribed in-plane displacements or free boundary along the edges. By observing that there are no normal and shear stresses across adjacent rays in Figure 2.16(a), he discovered that cuts parallel to the tension lines had no effect on the strain energy, while cuts not coinciding with tension rays release energy. Figure 2.16(b) shows two tension rays that cross the x-axis at angles α and $\alpha + \Delta\alpha$ and intersect at point H. The position along a tension ray is described by η expressed in terms of α and x. To determine the orientation of the tension rays, he concluded that the true distribution of tension rays maximized the strain energy, and thus coincides with the distribution of cuts which maximizes the work done at the boundaries. The distribution of tension rays and maximum tensile stress was determined for various membrane shapes and different material properties, e.g. shearing of a semi-infinite strip, torsion of an annular membrane and torsion of a quadrilateral membrane.

2.4.1.2 Relaxed energy model

General membrane theory cannot predict the details of the deformation of a wrinkled membrane; however the mean deformation and stress in a wrinkled region can be predicted if the strain energy density W^* is replaced by the relaxed strain energy density W [38, 39]. The stress derived from a relaxed energy density is never compressive. Considering an isotropic elastic membrane, the relaxed strain energy density W can be expressed as a symmetric function of the stretches μ_1 and μ_2, and the principal forces f_1 and f_2 are defined by

$$f_1 = \frac{\partial W}{\partial \mu_1}, f_2 = \frac{\partial W}{\partial \mu_2} \tag{2.49}$$

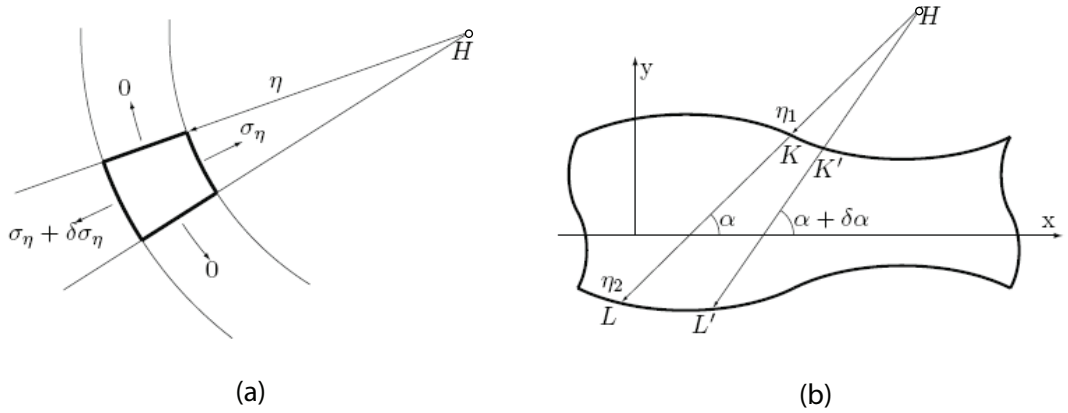

Figure 2.16: Membrane defined in tension field: (a) infinitesimal element of a membrane (b) membrane with tension ray [27].

In a state of simple tension, the stretch μ_1 induces transverse contraction $\mu_2 = \phi(\mu_1)$ due to Poisson's effect. We define $\phi(\mu_1)$ as *natural width in simple tension* with

$$f_1 = f_1(\lambda, w(\lambda)) = f(\lambda), f_2 = 0 \tag{2.50}$$

for isotropic incompressible material, the stretch of the membrane in the thickness direction is $1/(\mu_1\mu_2)$, which equals μ_2 in simple tension, so

$$\phi(\mu_1) = (\mu_1)^{-1/2} \tag{2.51}$$

Based on comparison of stretches and natural width, the relaxed strain energy is expressed as follows:

$$W = \begin{cases} W^*(\mu_1, \mu_2) & \text{if } \mu_2 \geq \phi(\mu_1) \text{ and } \mu_1 \geq \phi(\mu_2) \quad \text{taut} \\ W(\mu_1) & \text{if } \mu_2 \leq \phi(\mu_1) \text{ and } \mu_1 \geq 1 \quad \text{wrinkled} \\ W(\mu_2) & \text{if } \mu_1 \leq \phi(\mu_2) \text{ and } \mu_2 \geq 1 \quad \text{wrinkled} \\ 0 & \text{if } \mu_1 \leq 1 \text{ and } \mu_2 \leq 1 \quad \text{slack} \end{cases} \tag{2.52}$$

Then the strain energy in the taut region is

$$W^*(\mu_1, \mu_2) = \frac{E}{2(1-\nu^2)}[(\mu_1 - 1)^2 + (\mu_2 - 1)^2 + 2\nu(\mu_1 - 1)(\mu_2 - 1)] \tag{2.53}$$

And if the membrane is wrinkled, the relaxed strain energy becomes

$$W(\mu_1) = \frac{E}{2}(\mu_1 - 1)^2 \tag{2.54}$$

2.4.1.3 Variable Poisson's ratio model

A load-carrying path is prescribed to eliminate compressive stresses iteratively based on a variable Poisson's ratio model. An early, general approach was proposed by Stein and Hedgepeth [53] and further developed and applied by Mikulas [29]. After discovering some serious computational disadvantages associated with the direct implementation of the Stein-Hedgepeth approach, a new algorithm for finite element analysis based on the same assumption and field equations was proposed by Miller and Hedgepeth [30].

The stress-strain relationship within a statically determinant region of uniaxial stress that could be an approximation to the state of stress within a wrinkled portion of the membrane should be constructed. In a taut region, the stresses and strains are related according to the usual plane stress elastic equations for isotropic and elastic solids. However, within a wrinkled region, the usual elastic equations don't apply. Instead the assumption of negligible bending stress in the membrane yields the stress state:

$$\sigma_1 = E\varepsilon_1; \qquad \sigma_2 = 0 \tag{2.55}$$

where 1 and 2 are the directions parallel and perpendicular to the wrinkles, respectively. For the purpose of numerical analysis, it is desirable to express the stress in terms of the strains in the form

$$\{\sigma\} = [D]\{\varepsilon\} \tag{2.56}$$

where

$$\sigma = \{\sigma_x, \sigma_y, \tau_{xy}\}^T \qquad \varepsilon = \{\varepsilon_x, \varepsilon_y, \gamma_{xy}\}^T \tag{2.57}$$

Probably the most natural choice for $[D]$ is of the form

$$D_1 = \frac{E}{1-\lambda^2}\begin{bmatrix} 1 & \lambda & 0 \\ \lambda & 1 & 0 \\ 0 & 0 & (1-\lambda)/2 \end{bmatrix} \tag{2.58}$$

where the "variable Poisson's ratio" λ varies from point to point within the wrinkled region so that $[D_1]$ is not a constant matrix. This "variable Poisson's ratio" formulation is precisely the approach used by Stein, Hedgepeth and Mikulas to develop closed form solutions to simple problems. However, because of the presence of the term $1/(1-\lambda^2)$, $[D_1]$ is not suitable for numerical implementation within the wrinkled region where $\lambda = 1$. Hence another representation for $[D]$ is desirable.

Miller and Hedgepeth [31] introduced another wrinkled matrix with the form

$$D_w = \frac{E}{4}\begin{bmatrix} 2(1+P) & 0 & Q \\ 0 & 2(1-P) & Q \\ Q & Q & 1 \end{bmatrix} \tag{2.59}$$

where $P = (\epsilon_x - \epsilon_y)/(\epsilon_1 - \epsilon_2)$ and $Q = \gamma_{xy}/(\epsilon_1 - \epsilon_2)$. No singularities of the matrix are observed for any value of P and Q between 0 and 1, and hence this numerical representation of D_w has no difficulties.

In any taut regions, where λ = Poisson's ratio, the following matrix based on Hooke's law for plane stress is used.

$$D_t = \frac{E}{1-\nu^2}\begin{bmatrix} 1 & \nu & 0 \\ \nu & 1 & 0 \\ 0 & 0 & (1-\nu)/2 \end{bmatrix} \tag{2.60}$$

Adler [1] implemented this model as a user-defined material (UMAT) subroutine in the Standard finite element package.

2.4.2 Wrinkling criteria

A membrane can be in three different stress states: *taut*, *wrinkled* or *slack*. Depending on the stress state, a different constitutive matrix should be used: D_t is applicable for the *taut* state, D_w is applicable for the *wrinkled* state and the modulus matrix is set to be zero in the *slack* state. This raises the problem of how one defines such stress states. The stress criterion is as follows: a membrane is in a *taut* state if both principal stresses, denoted by σ_1 and σ_2, are positive; it is in a *wrinkled* state if the minor principal stress is non-positive and the major principal stress is tensile; there is also a *slack* state, which is the extreme case of a wrinkled membrane where all the stresses are non-positive.

Similarly, an alternative wrinkling criterion, based on the principal strains denoted by ε_1 and ε_2, can be formulated. The membrane is in a taut state when the major principal strain is positive, i.e. tensile, and the minor principal strain be greater than the strain predicted purely by Poisson's ratio effects [30]. It is slack if both principal strains are non-positive. In both the taut and slack states there is no wrinkling in the membrane. Therefore, a wrinkled state occurs in the membrane when the minor principal strain is less than the strain due to the Poisson's ratio and the major principal strain is positive.

The two criteria can be summarized as follows,

a) Principal stress criterion

(i) $\sigma_2 > 0$ taut

(ii) $\sigma_2 \leq 0$ and $\sigma_1 > 0$ wrinkled

(iii) $\sigma_2 \leq 0$ and $\sigma_1 \leq 0$ slack

b) Principal strain criterion

(i) $\varepsilon_1 > 0$ and $\varepsilon_2 > -\nu\varepsilon_1$ taut

(ii) $\varepsilon_1 > 0$ and $\varepsilon_2 \leq -\nu\varepsilon_1$ wrinkled

(iii) $\varepsilon_2 \leq 0$ and $\varepsilon_1 \leq 0$ slack

A combination of the above two criteria can also be introduced.

c) Combined criterion

(i) $\sigma_2 > 0$ taut

(ii) $\sigma_2 \leq 0$ and $\varepsilon_1 > 0$ wrinkled

(iii) $\sigma_1 \leq 0$ and $\varepsilon_1 \leq 0$ slack

2.4.3 Wrinkling of orthotropic films

Wu [60, 61, 62] represented the true deformed surface of a wrinkled membrane by a so-called smooth pseudo-deformed surface and hence introduced the wrinkle strain as a kinematic variable to measure the wrinkliness of a wrinkled surface. Based on the same basic ideas, Kang and Im [24] proposed an iterative scheme convenient for the finite element analysis of wrinkling in orthotropic membrane structures, which was later adopted by Gerngross and Pellegrino [18, 19, 20]. Alternative approaches have been proposed by Epstein and Forcinito [16] and Raible et al. [40].

The general idea in Kang and Im's paper is that a wrinkled region in a thin film is in a state of uniaxial tension and the orientation and magnitude of this tension can be obtained from an invariant relation between strain components. The actual wrinkled shape of the film is not of interest, instead a fictitious non-wrinkled surface is used to describe the average deformation of the film.

Consider an undeformed material element ABCD, as shown in Figure 2.17(a). Let $(\widehat{x}, \widehat{y})$ denote a Cartesian coordinate system in the undeformed configuration, where $\widehat{x}, \widehat{y}$ are aligned with the directions of orthotropy of the material. Let (x, y) denote a rotated Cartesian coordinate system for the same material point but such that x is the direction of the uniaxial stress in the wrinkled material. The rigid body rotation angle, α, from $\widehat{x}\widehat{y}$ to xy is called the *wrinkling angle*. It is noteworthy that for isotropic materials the wrinkling angle is the same as the principal stress or strain angle but this is generally not the case for anisotropic materials.

After this rigid body rotation, the material element, which is now considered in a rotated Cartesian coordinate system, is transformed from the undeformed configuration ABCD to the final, wrinkled configuration $\mathrm{A}''\mathrm{B}''\mathrm{C}''\mathrm{D}''$ in two steps, Figure 2.17(b). The first step is a pure deformation from the undeformed

configuration ABCD to the deformed configuration $\mathrm{A}'\mathrm{B}'\mathrm{C}'\mathrm{D}'$, due to the application of the correct uniaxial stress σ_x. No wrinkling occurs during this deformation, because there are no constraints on the deformation kinematics. This deformation consists of a normal strain ϵ_x^u, a transverse contraction ϵ_y^u (due to the Poisson's ratio of the membrane), and an additional shear strain γ_{xy}^u (only in the case of anisotropic materials). This strain state is called the *state of natural uniaxial tension* and the superscript u has been used to denote the corresponding strains. The second step involves pure wrinkling from $\mathrm{A}'\mathrm{B}'\mathrm{C}'\mathrm{D}'$ to $\mathrm{A}''\mathrm{B}''\mathrm{C}''\mathrm{D}''$. During this step, the stress in the material does not change and hence its strain state also does not change, but the material element "shrinks" due to the formation of a series of wrinkles. At this point, though, the actual material element (which is no longer planar) is replaced by a fictitious wrinkled surface with the same outer profile.

Let $\overline{e_1}$ and $\overline{e_2}$ be unit vectors denoting respectively the x and y direction. The material point $\overline{X} = X_1\overline{e_1} + X_2\overline{e_2}$ in the reference configuration ABCD corresponds to point $\overline{x} = x_1\overline{e_1} + x_2\overline{e_2}$ in the state of natural uniaxial tension (i.e., in configuration $\mathrm{A}'\mathrm{B}'\mathrm{C}'\mathrm{D}'$) and to point $\overline{x^u} = x_1^u\overline{e_1} + x_2^u\overline{e_2}$ in the final deformed configuration $\mathrm{A}''\mathrm{B}''\mathrm{C}''\mathrm{D}''$. The mapping from ABCD to $\mathrm{A}'\mathrm{B}'\mathrm{C}'\mathrm{D}'$ is written as $x_1^u = a^u X_1 + c^u X_2$ and $x_2^u = b^u X_2$, and the mapping from ABCD to $\mathrm{A}''\mathrm{B}''\mathrm{C}''\mathrm{D}''$ is written as $x_1 = aX_1 + cX_2$ and $x_2 = bX_2$.

During the wrinkling process, the points A', B', C', D' move vertically to A'', B'', C'', D'', therefore there is no deformation of $\overline{e_2}$, but there is still contraction of $\overline{e_1}$, i.e.

$$a = a^u, c = c^u \quad \text{and} \quad b \leq b^u \tag{2.61}$$

The Green strain tensors for the fictitious wrinkled state and the state of natural uniaxial tension are

$$\begin{aligned} \epsilon &= \frac{1}{2}(a^2-1)\overline{e_1}\otimes\overline{e_1} + \frac{1}{2}ac(\overline{e_1}\otimes\overline{e_2} + \overline{e_2}\otimes\overline{e_1}) + \frac{1}{2}(b^2+c^2-1)\overline{e_2}\otimes\overline{e_2} \\ &= \epsilon_x\overline{e_1}\otimes\overline{e_1} + \epsilon_{xy}\overline{e_1}\otimes\overline{e_2} + \epsilon_{yx}\overline{e_2}\otimes\overline{e_1} + \epsilon_y\overline{e_2}\otimes\overline{e_2} \end{aligned} \tag{2.62}$$

$$\begin{aligned} \epsilon^u &= \frac{1}{2}[(a^u)^2-1]\overline{e_1}\otimes\overline{e_1} + \frac{1}{2}(a^u)(c^u)(\overline{e_1}\otimes\overline{e_2} + \overline{e_2}\otimes\overline{e_1}) + \frac{1}{2}[(b^u)^2+(c^u)^2-1]\overline{e_2}\otimes\overline{e_2} \\ &= \epsilon_x^u\overline{e_1}\otimes\overline{e_1} + \epsilon_{xy}^u\overline{e_1}\otimes\overline{e_2} + \epsilon_{yx}^u\overline{e_2}\otimes\overline{e_1} + \epsilon_y^u\overline{e_2}\otimes\overline{e_2} \end{aligned} \tag{2.63}$$

Comparing the above three equations, we conclude that in the wrinkled state the strain components ϵ_x and γ_{xy} remain unchanged, i.e. $\epsilon_x = \epsilon_x^u$ and $\gamma_{xy} = \gamma_{xy}^u$, but the transverse strain ϵ_y is different due to the over-contraction of the material in the direction perpendicular to the stress direction, i.e. $\epsilon_y^u \geq \epsilon_y$.

Assuming that the Green strain ϵ in the membrane is small, it is approximately equal to the standard

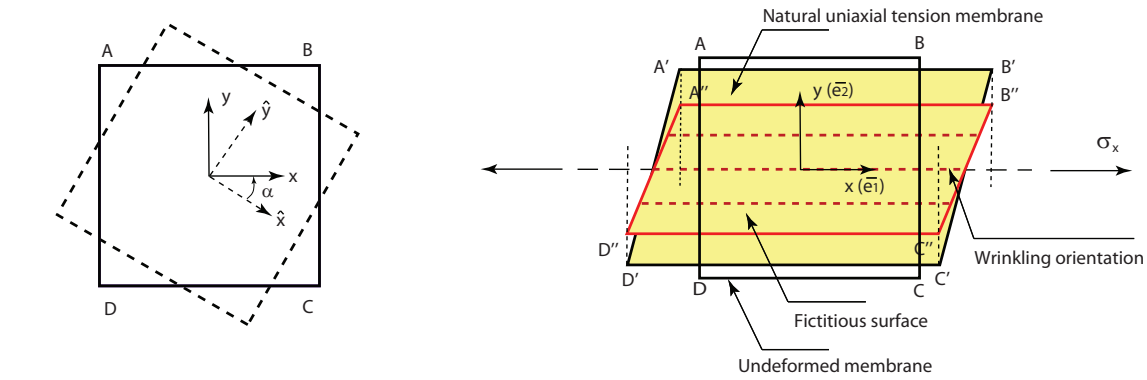

(a) Rigid body rotaion of Cartesian coordinate system

(b) Wrinkling process of deformed configurations

Figure 2.17: States of a wrinkled element.

Cauchy strain and so the stress-strain relationship has the standard linear form

$$\left\{\begin{array}{c}\widehat{\sigma_x}\\ \widehat{\sigma_y}\\ \widehat{\tau_{xy}}\end{array}\right\} = \left[\begin{array}{ccc}\widehat{C_{11}} & \widehat{C_{12}} & 0\\ \widehat{C_{21}} & \widehat{C_{22}} & 0\\ 0 & 0 & \widehat{C_{66}}\end{array}\right] \cdot \left\{\begin{array}{c}\widehat{\epsilon_x}\\ \widehat{\epsilon_y}\\ \widehat{\gamma_{xy}}\end{array}\right\} \tag{2.64}$$

which can be written in the compact form $\{\widehat{\sigma}\} = [\widehat{C}]\{\widehat{\epsilon}\}$. Note that the shear-extension coupling terms in this material stiffness matrix $[\widehat{C}]$ are zero because the relationship has been set up in the directions of orthotropy of the material. This stress-strain relationship can be transformed to the x, y coordinate system by rotating through the angle α

$$\left\{\begin{array}{c}\sigma_x\\ \sigma_y\\ \tau_{xy}\end{array}\right\} = \left[\begin{array}{ccc}C_{11} & C_{12} & C_{16}\\ C_{21} & C_{22} & C_{26}\\ C_{61} & C_{62} & C_{66}\end{array}\right] \cdot \left\{\begin{array}{c}\epsilon_x\\ \epsilon_y\\ \gamma_{xy}\end{array}\right\} \tag{2.65}$$

or $\{\sigma\} = [C]\{\epsilon\}$. Here $\{\epsilon\}$ can be obtained from $\{\widehat{\epsilon}\}$ by the transformation

$$[C] = [T][\widehat{C}][R][T]^{-1}[R]^{-1} \tag{2.66}$$

where $[R] = \text{diag}\{1, 1, 2\}$ and

$$[T] = \left[\begin{array}{ccc}\cos^2(\alpha) & \sin^2(\alpha) & 2\sin(\alpha)\cos(\alpha)\\ \sin^2(\alpha) & \cos^2(\alpha) & -2\sin(\alpha)\cos(\alpha)\\ -\sin(\alpha)\cos(\alpha) & \sin(\alpha)\cos(\alpha) & \cos^2(\alpha) - \sin^2(\alpha)\end{array}\right]. \tag{2.67}$$

The wrinkling angle α has to be such that the normal stress in the direction perpendicular to the wrinkles is zero and the shear stress is also zero, that is $\sigma_y^u = \tau_{xy}^u = 0$. If this condition is satisfied, then the transverse strain ϵ_y^u and the shear strain γ_{xy}^u can be obtained from

$$\epsilon_y^u = \epsilon_x^u \frac{C_{21}C_{66} - C_{26}C_{61}}{C_{26}C_{62} - C_{22}C_{66}} \tag{2.68}$$

$$\gamma_{xy}^u = \epsilon_x^u \frac{C_{22}C_{61} - C_{21}C_{62}}{C_{26}C_{62} - C_{22}C_{66}} \tag{2.69}$$

Kang and Im [24] proposed an iterative approach to search for the wrinkling angle; their procedure to find α is as follows. First, one determines a value of α that satisfies the relationship $\gamma_{xy}^u = \gamma_{xy}$, with $\epsilon_x^u = \epsilon_x$. Here, ϵ_y^u and γ_{xy}^u are calculated from Equations 2.68 and 2.69. Finding α is equivalent to solving the equation

$$f(\alpha) = \gamma_{xy}^u(\alpha) - \gamma_{xy}(\alpha) = 0 \tag{2.70}$$

which may have multiple solutions between 0 and 180 degrees. To find all of the solutions, we first divide the domain into ten uniform intervals and look for a change of sign between two boundary points in any interval. If a change of sign is found, then there is at least one solution inside this particular interval. Then we iteratively calculate the intersection between a straight line connecting two boundary points and the x-axis until the error is less than a prescribed tolerance. Once we have found a value of α that satisfies this equation, we check that $\epsilon_y^u \geq \epsilon_y$ and if this inequality is satisfied, then α defines the wrinkling orientation. If no change of sign is found, the domain is divided into 50 intervals and the calculation is repeated.

Chapter 3

Wrinkling of Orthotropic Viscoelastic Membrane

Wrinkling of thin membranes has attracted much interest and yet little is known about wrinkles in anisotropic viscoelastic membranes. Our interest in this topic is motivated by current research in superpressure balloons, and particularly their behavior during inflation when the balloon envelope is heavily wrinkled. When wrinkling had been combined with these effects, we were unable to find any published test cases that could be used to confirm the validity of our simulations and so we decided to carry out our own set of experiments as well. In addition, viscoelastic simulations based on the convolution integral would be generally computationally expensive, so a more efficient numerical scheme is required to reduce the computational burden.

In this chapter, we begin with a computational scheme that models the viscoelasticity of the film with an incremental, pseudoelastic representation that is modified to allow for the formation of wrinkles, when a combined stress-strain wrinkling criterion is satisfied. This scheme is then implemented as a VUMAT subroutine in the finite element software Abaqus/Explicit. Next we consider the special case of isotropic and elastic membranes, for which there is an extensive literature, and compare the results from our simulations to some published results. The following section presents a set of experiments that have been carried out on balloon film in a simple shear apparatus; the experimental setup and procedure are described and the results of shear tests are presented. Finally these experimental results are compared with the simulations.

3.1 Effective material stiffness matrix

A particular balloon film, StratoFilm 420, will be considered in this study. This film has been extensively characterized by Rand [43, 44]. In the first part of this section we review the nonlinear viscoelastic properties of Stratofilm 420 and then develop an approximate pseudoelastic constitutive model for a chosen temperature, time interval and stress level; this approach was inspired by Stubstad and Simitses [54]. In the second part of the section we modify the pseudoelastic coefficients to consider the effects of wrinkling.

Table 3.1: Prony series for StratoFilm SF420

i	D_i (MPa^{-1})	τ_i (s)
1	1.8764×10^{-4}	1.6548×10^{-16}
2	2.9249×10^{-5}	4.8697×10^{-15}
3	5.8224×10^{-5}	1.4330×10^{-13}
4	8.7542×10^{-5}	4.2170×10^{-12}
5	1.1561×10^{-4}	1.2409×10^{-10}
6	1.4159×10^{-4}	3.6517×10^{-9}
7	1.6989×10^{-4}	1.0746×10^{-7}
8	2.0924×10^{-4}	3.1623×10^{-6}
9	2.7274×10^{-4}	9.3057×10^{-5}
10	3.7796×10^{-4}	2.7384×10^{-3}
11	5.4670×10^{-4}	8.0582×10^{-2}
12	8.0581×10^{-4}	2.3714
13	1.1844×10^{-3}	69.783
14	1.7204×10^{-3}	2053.5
15	2.6285×10^{-3}	60430

3.1.1 Pseudoelastic model for StratoFilm 420

StratoFilm 420 is a 38 micron thick film made of Linear Low Density Polyethylene. Rainwater [41] and Rand [43, 44] has developed a nonlinear viscoelastic constitutive model for this film.

The transient compliance $\Delta D(T_0, \psi)$ in the machine direction of the film was given at a reference temperature T_0 =293.16 K and the instantaneous compliance $D_0 = 3.0 \times 10^{-10}$ (Pa^{-1}) was chosen to ensure that the transient compliance D_i would all be positive. The coefficients of a 15 term Prony series are listed in Table 3.1.

The temperature shift factor a_T was evaluated over the range 163 K to 323 K and then fitted at the reference temperature $T_0 = 293.16$K in the logarithmic form

$$\log a_T = \begin{cases} (T - 293.16)[7.33 \times 10^{-4}(T - 273.16) - 0.179133] & T > 233.16 \\ 3.1068 - 0.2350275(T - 273.16) & T < 233.16 \end{cases} \tag{3.1}$$

The stress shift was represented by a_σ

$$\log a_\sigma = -0.126(\sigma_{\text{eff}} - \sigma_0) \tag{3.2}$$

where σ_0 is threshold at which linear behavior ends and nonlinear behavior begins

$$\sigma_0 = 69.527 - 0.430944T + 6.7962 \times 10^{-4}T^2 \tag{3.3}$$

Two of the non-linear coefficients, g_0 and g_1 were set equal to 1. The parameter g_2 was described by

$$g_2 = 1 + 0.1875(\sigma_{\text{eff}} - \sigma_0) \tag{3.4}$$

The coefficients for the biaxial model were, in addition to $S_{11} = 1$,

$$S_{22} = 1.122 + 6.5895 \times 10^{-4}T - 6.609 \times 10^{-6}T^2 \tag{3.5}$$

and $S_{12} = S_{21} = -0.58$, $S_{66} = 4.45$. Clearly in-plane Poisson's ratio in longitudinal direction $\nu_{21} = S_{12} = 0.58$, while Poisson's ratio in transverse direction $\nu_{12} = S_{12}/S_{22}$, equal to 0.744 at 283 K. Balloon film SF 420, composed of three-layer LLDPE, shows weak anisotropy in plane, and thus is assumed in-plane isotropic material. Its out-of-plane behavior can be very different from in-plane, but is of little interest due to plane stress assumption. For in-plane isotropic composite material, even if in-plane Poisson's ratio is greater than 0.5, it still possesses positive definite stiffness matrix.

The coefficients for the effective stress, A_{ij}, were expressed as

$$A_{22} = 1.44, A_{12} = -0.4 \text{ and } A_{66} = 0.8 \tag{3.6}$$

A finite-element implementation of the above constitutive model for the analysis of a single balloon lobe has been developed by Gerngross and Pellegrino [18, 19, 20] model. Here we present an alternative approach that, although less accurate, is more suitable for large scale simulations of balloon structures.

For a given time t, the integral representation for the strain $\epsilon(t)$ in Equation 2.45 can be approximated by replacing the convolution integral with a series of m equal substeps $\Delta t = \frac{t}{m}$ where each term is evaluated at the discrete time $t_i = i\Delta t$

$$\begin{aligned} \epsilon(t) &\approx g_0 D_0 \sigma(t) + g_1 \sum_{i=1}^{m} \Delta D(\psi^t - \psi^{t_{i-1}}) \Delta[g_2(\sigma^{t_i})\sigma(t_i)] \\ &= g_0 D_0 \sigma(t) + g_1 \sum_{i=1}^{m} \Delta D(\psi^t - \psi^{t_{i-1}})[g_2(\sigma^{t_i})\sigma(t_i) - g_2(\sigma^{t_{i-1}})\sigma(t_{i-1})] \end{aligned} \tag{3.7}$$

Substituting $g_0 = g_1 = 1$ and assuming that g_2 changes slowly over Δt, i.e. $g_2(\sigma^{t_i}) \approx g_2(\sigma^{t_{i-1}})$, then the above equation becomes

$$\begin{aligned} \epsilon(t) &\approx D_0 \sum_{i=1}^{m} \Delta\sigma(t_i) + \sum_{i=1}^{m} g_2(\sigma^{t_i}) \Delta D(\psi^t - \psi^{t_{i-1}}) \Delta\sigma(t_i) \\ &= \sum_{i=1}^{m} [D_0 + g_2(\sigma^{t_i}) \Delta D(\psi^t - \psi^{t_{i-1}})] \Delta\sigma(t_i) \end{aligned} \tag{3.8}$$

Hence, we can define a pseudoelastic compliance, $D^{p,i}$ (the superscript p corresponds to "pseudoelastic")

between $i\Delta t$ and t, and considering the corresponding reduced times

$$D^{p,i} = D_0 + g_2 \Delta D(\psi^t - \psi^{t_{i-1}}) \tag{3.9}$$

The corresponding strain can then be expressed as

$$\epsilon(t) = \sum_{i=1}^{m} D^{p,i} \Delta\sigma(t_i) = \sum_{i=1}^{m} \Delta\epsilon(t_i) \tag{3.10}$$

This uniaxial expression can be generalized to plane stress by defining the pseudoelastic compliance in the machine direction, $\widehat{D}_{11}^{p,i}$, from Equation 3.9

$$\widehat{D}_{11}^{p,i} = D_0 + g_2 \Delta D(\psi^t - \psi^{t_{i-1}}) \tag{3.11}$$

and the remaining coefficients of the pseudoelastic compliance matrix are then

$$\widehat{D}_{22}^{p,i} = S_{22}\widehat{D}_{11}^{p,i} \ , \ \widehat{D}_{12}^{p,i} = \widehat{D}_{21}^{p,i} = S_{12}\widehat{D}_{11}^{p,i} \ , \ \widehat{D}_{66}^{p,i} = S_{66}\widehat{D}_{11}^{p,i} \tag{3.12}$$

It follows from Equation 3.10 that the strain at time t can be obtained as a sum of strain increments, which are calculated from the stress increments multiplied by the corresponding total pseudoelastic compliances. For each increment, the pseudoelastic compliance is constant.

For example, if we consider the conditions of constant temperature $T = 293$ K, constant stress $\widehat{\sigma_x} = 4.5$ MPa, $\widehat{\sigma_y} = 5.0$ MPa and $\widehat{\tau_{xy}} = 0$ MPa, the shift of the compliance master curve in the machine direction is shown in Figure 3.1. At time $t = 1000$ s, the pseudoelastic moduli can be obtained from the compliance at the point marked with a dot in Figure 3.1. They are respectively $\widehat{E}_{11}^{p} = 90.98$ MPa and $\widehat{E}_{22}^{p} = 121.68$ MPa.

The pseudoelastic stiffness matrix in the directions of orthotropy of the film can be obtained by inversion of $\widehat{D}^{p,i}$

$$\widehat{E}^{p,i} = \begin{bmatrix} \widehat{E}_{11}^{p,i} & \widehat{E}_{12}^{p,i} & 0 \\ \widehat{E}_{21}^{p,i} & \widehat{E}_{22}^{p,i} & 0 \\ 0 & 0 & \widehat{E}_{66}^{p,i} \end{bmatrix} \tag{3.13}$$

where

$$\begin{aligned} \widehat{E}_{11}^{p,i} &= \frac{1}{D_{11}^{p,i}} \frac{1}{S_{11} - S_{12}^2/S_{22}} \\ \widehat{E}_{12}^{p,i} &= E_{21}^{p,i} = \frac{1}{D_{11}^{p,i}} \frac{1}{S_{12} - S_{11}S_{22}/S_{12}} \\ \widehat{E}_{22}^{p,i} &= \frac{1}{D_{11}^{p,i}} \frac{1}{S_{22} - S_{12}^2/S_{11}} \\ \widehat{E}_{66}^{p,i} &= \frac{1}{D_{11}^{p,i}} \frac{1}{S_{66}} \end{aligned}$$

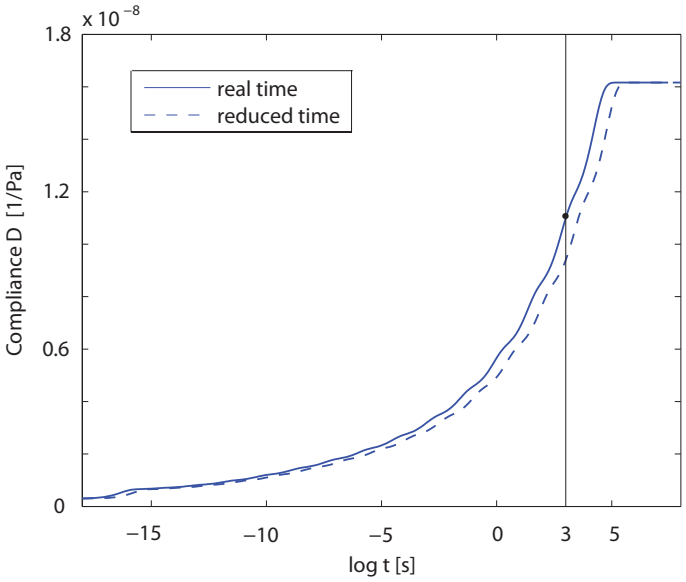

Figure 3.1: Master curves of compliance in machine direction.

3.1.2 Correction for wrinkling

Kang and Im [24] compared the three types of wrinkling criteria described in 2.4.2. They concluded that the mixed criterion works better for anisotropic wrinkling as it avoids numerical divergence caused by making wrong judgements about the membrane state, which happened with the principal stress based criterion.

The effective elasticity matrix depends on the state of a membrane element:

- Minor principal stress $\sigma_2 > 0$: the membrane is *taut*, hence Equation 3.13 is valid.
- Minor principal stress $\sigma_2 \leq 0$ and major principal strain $\varepsilon_1 > 0$: the membrane is *wrinkled*.

  Hence we must solve for the wrinkling angle α. First we transform the pseudoelastic stiffness in Equation 3.13 to the rotated coordinate system x, y (the transformation is analogous to Equation 2.65). In this system, the normal strain ϵ_x and the shear strain γ_{xy} are equal to the strains in the state of natural uniaxial tension whereas ϵ_y is not. The transverse stress σ_y has to be zero in a coordinate system aligned with the wrinkles, hence

$$\sigma_y = E_{21}^{p,i}\epsilon_x + E_{22}^{p,i}\epsilon_y + E_{23}^{p,i}\gamma_{xy} = 0 \tag{3.14}$$

  From the above equation, ϵ_y can be expressed in terms of ϵ_x and γ_{xy}.

$$\epsilon_y = -\frac{E_{21}^{p,i}}{E_{22}^{p,i}}\epsilon_x - \frac{E_{26}^{p,i}}{E_{22}^{p,i}}\gamma_{xy} \tag{3.15}$$

  Hence we eliminate ϵ_y by substituting this expression into Equation 2.65, and obtain the effective

elasticity matrix [20] for the wrinkled element

$$E_w^{p,i} = \begin{bmatrix} E_{11}^{p,i} - \frac{E_{12}^{p,i} E_{21}^{p,i}}{E_{22}^{p,i}} & 0 & E_{13}^{p,i} - \frac{E_{12}^{p,i} E_{26}^{p,i}}{E_{22}^{p,i}} \\ 0 & 0 & 0 \\ E_{61}^{p,i} - \frac{E_{62}^{p,i} E_{21}^{p,i}}{E_{22}^{p,i}} & 0 & E_{66}^{p,i} - \frac{E_{26}^{p,i} E_{62}^{p,i}}{E_{22}^{p,i}} \end{bmatrix} \tag{3.16}$$

An alternative method is using directly the strains in the state of natural uniaxial tension $\{\epsilon^u\}$ from Equations 2.68 and 2.69. Hence the corrected stress in the wrinkled state $\{\sigma\}$ has to be a uniaxial tension, rewritten as $\{\sigma\} = \{\sigma^u\} = E^{p,i}\{\epsilon^u\}$. Since the element is under uniaxial tension, only the x component σ_x is nonzero. Finally $\{\sigma\}$ is transformed back to $\{\widehat{\sigma}\}$ in the direction of orthotropy.

- Major principal strain $\varepsilon_1 \leq 0$ and minor principal stress $\sigma_2 < 0$: the membrane is *slack* and hence $E_s^{p,i} = [0]$

In conclusion, to calculate the correct stress, the following steps are carried out:

Step 1. Check the state of the membrane element by means of the mixed criterion;

Step 2. If the element is wrinkled, find the wrinkling angle α from Kang and Im's scheme, described in Section 2.4.3;

Step 3. Compute the corrected Cauchy stress using the effective elasticity matrix.

The stress and strain components used for the above wrinkling tests should ideally be the best current estimates of the values at time t. However our current approach is to run each step i as a separate simulation in ABAQUS/Explicit and hence the only estimates that are available in each run are only the estimates based on the current increment.

3.2 Finite element implementation

In Section 3.1.1 we have presented an approach to obtain approximate estimates of the stresses in a viscoelastic film at time t. The loading sequence is divided into m steps, where m is determined by the required precision, and

$$\sigma(t) = \sum_{i=1}^{m} \Delta\sigma(t_i) = \sum_{i=1}^{m} \widehat{E}^{p,i} \Delta\epsilon(t_i) \tag{3.17}$$

For example, the strain increments due to a three step loading sequence are shown on the left of Figure 3.2(a), hence

$$\epsilon = \Delta\epsilon_1 + \Delta\epsilon_2 + \Delta\epsilon_3 \tag{3.18}$$

The stress at the end time, t_3, due to the strain increments $\Delta\epsilon_i$ is computed with ABAQUS/Explicit in three separate analyses with compliances $\widehat{E}^{p,i}$. The results are shown in Figure 3.2(b-d) and are superposed

in Figure 3.2(a). From the plots on the right in Figure 3.2, the stress at time t_3 is given by

$$\begin{aligned} \sigma(t_3) &= \Delta\sigma_1 + \Delta\sigma_2 + \Delta\sigma_2 \\ &= E^{p,1}\Delta\epsilon_1 + E^{p,2}\Delta\epsilon_2 + E^{p,3}\Delta\epsilon_3 \end{aligned} \tag{3.19}$$

Note that an approximation in this approach is to assume that the wrinkling directions in each step will not change significantly between the various steps,. Also, the coefficient g_2 is stress-dependent and so is not correctly estimated for the full stress level. In other words, the proposed linear superposition is suitable for weakly nonlinear materials with only small wrinkle angle changes.

A user-defined material ABAQUS/Explicit subroutine (VUMAT) has been written to model wrinkling in an orthotropic viscoelastic film. It is schematically described in Figure 3.3.

3.3 Verification for isotropic elastic membranes

We have tested our VUMAT implementation of wrinkling in ABAQUS/Explicit by means of a comparison with the analytical solution for a linear-elastic, time-independent rectangular membrane under simple shear. The longer edges of the membrane are attached to rigid edges that are sheared uniformly while the shorter edges are unconstrained. This problem was investigated by Wong and Pellegrino [59].

3.3.1 Construction of FE model

This test case involves a rectangular membrane under simple shear [32]. The properties of the film used in the model and the geometrical dimensions of the rectangular membrane are summarized in Table 3.2.

Table 3.2: Summary of membrane properties

Length, L (mm)	380
Height, H (mm)	128
Thickness, t (mm)	0.025
Young's Modulus, E (N/mm^2)	3530
Poisson's ratio, ν	0.33
Density, ρ (kg/mm^3)	1.46×10^{-6}

The membrane was modeled with 3-node, fully integrated triangular membrane elements (M3D3). All translations of the bottom edge nodes were fully constrained, whereas the top edge nodes were left free. As shown in Figure 3.4, the shear load was applied in terms of a horizontal shear displacement of the top edge.

The loading process consisted of two analysis steps: during the first step, lasting 2.5 seconds, the upper edge nodes were moved by 3 mm in the x-direction while all other translations were constrained. In the second step, also lasting 2.5 seconds, all the translational degrees of freedom on the upper and lower edges were constrained, to test the stability of the simulation.

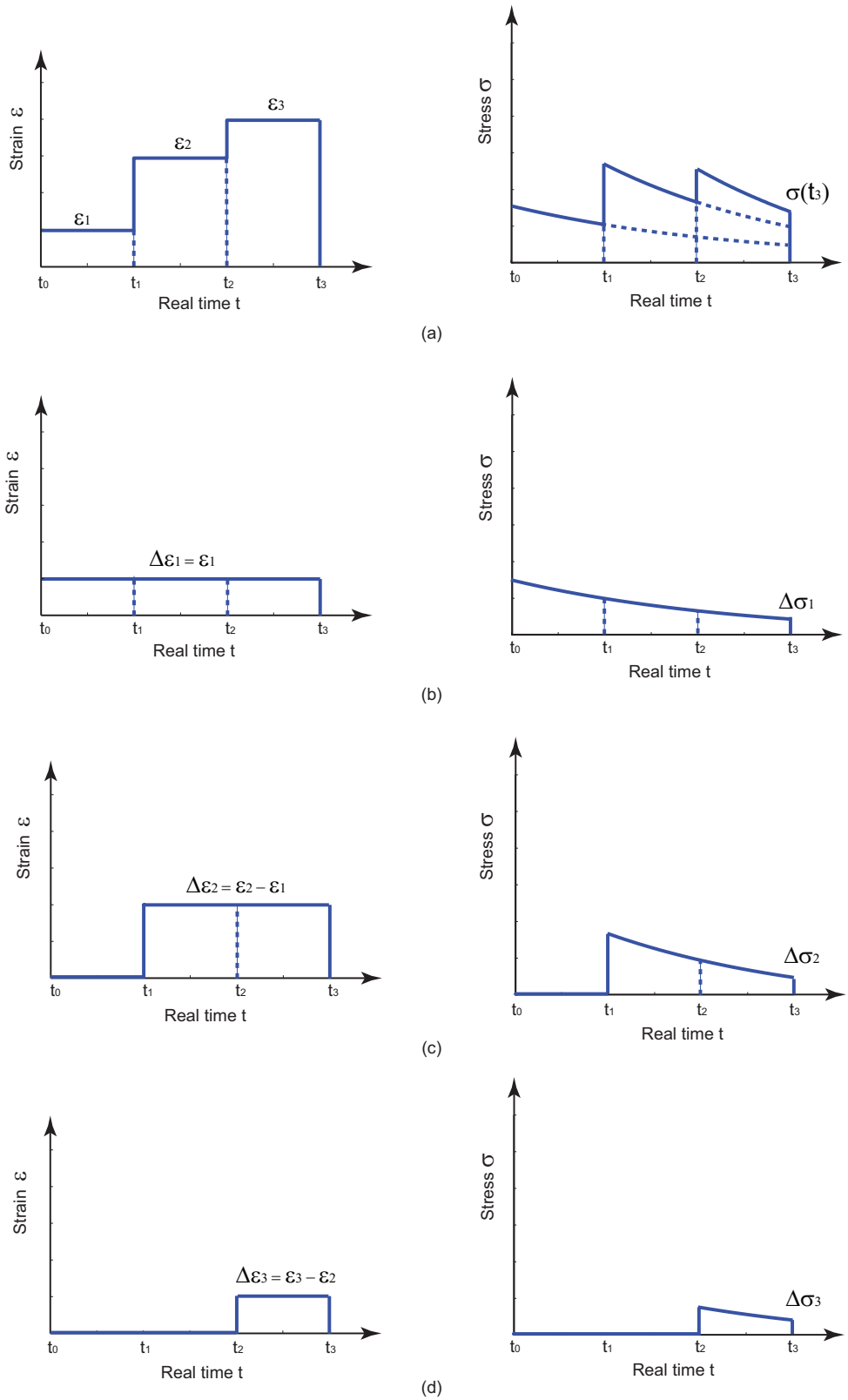

Figure 3.2: Superposition of loading steps: (a) total strain input and stress response; (b)−(d) incremental strain functions and corresponding stress responses.

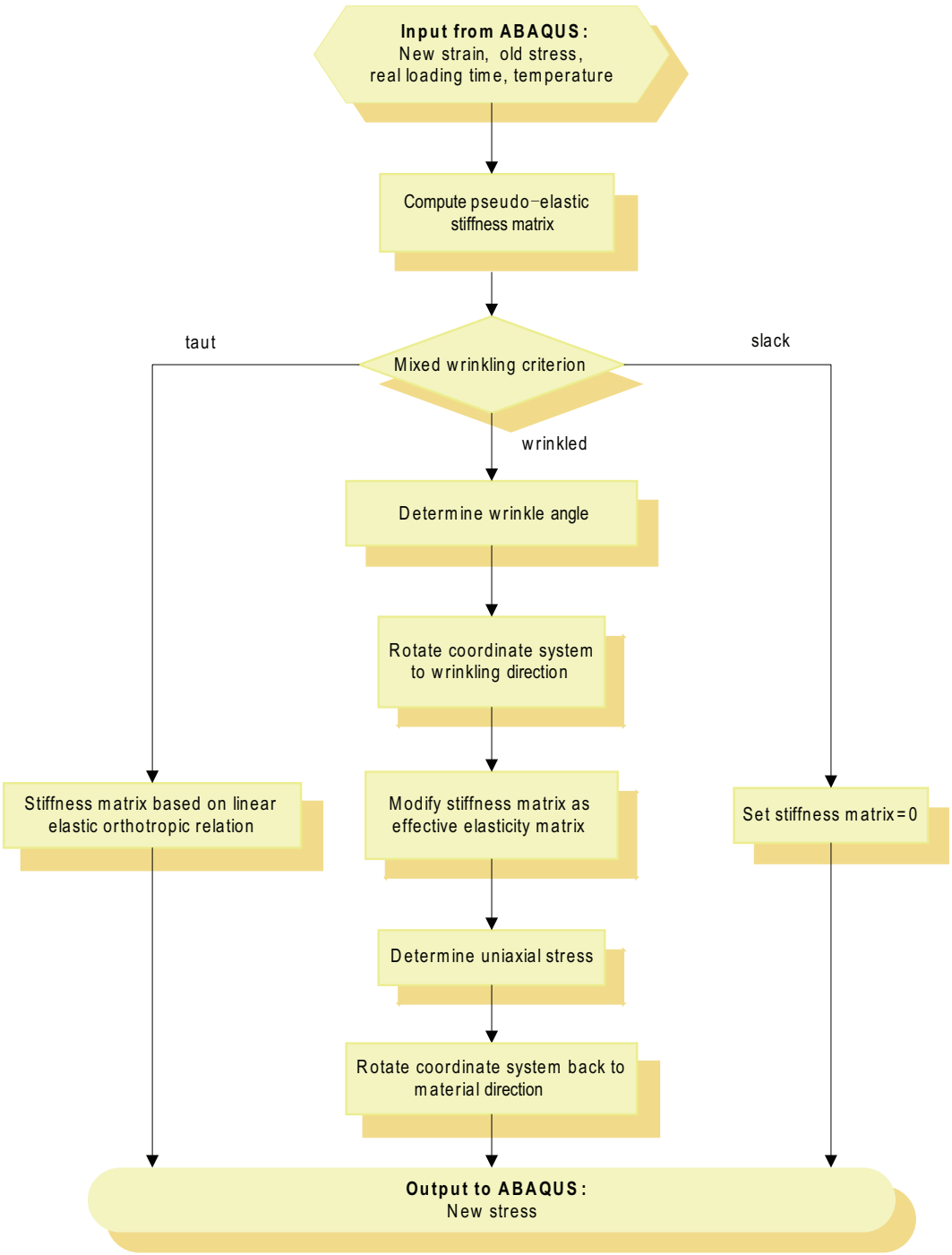

Figure 3.3: Wrinkling algorithm for linear orthotropic viscoelastic material subroutine VUMAT.

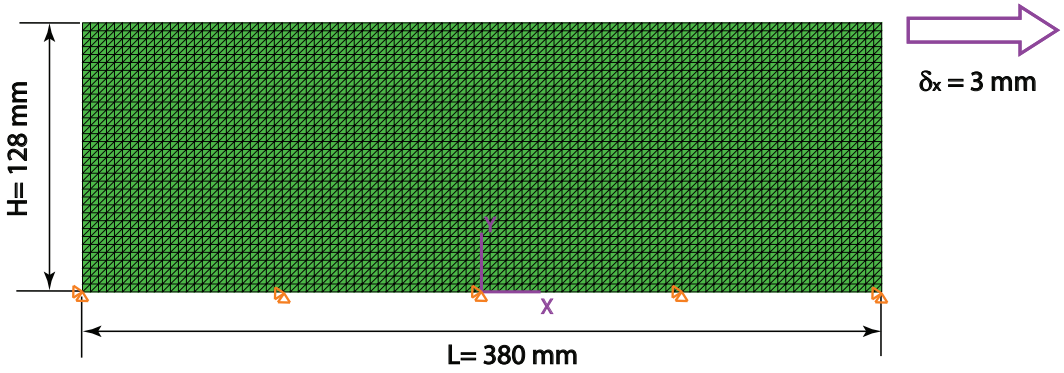

Figure 3.4: Finite element mesh for membrane in shear.

3.3.2 Results

The stress distribution corresponding to the final value of the horizontal displacement of the membrane is illustrated by means of contour plots and a vector plot, in Figure 3.5. Since the major principal stress, σ_1, is much greater than the minor principal stress, σ_2, only the major stress can be seen in the vector plot. The direction of the major principal stress, inclined at 45°, corresponds to the direction of the wrinkles. The dense distributions of vectors at the top-right and bottom-left corners indicate two areas of stress concentration.

The membrane finite element model using the VUMAT subroutine has succeeded in eliminating all negative stress, as illustrated by the minor stress distribution being approximately non-negative everywhere.

The principal stresses across the middle of the membrane are plotted in Figure 3.6. σ_1 increases from zero at the edge to a uniform and positive value, σ_1 =41.36 MPa, whereas σ_2 remains approximately zero. The major principal strain is at 45° and given by Wong and Pellegrino [58]

$$\epsilon_1 = \frac{\gamma}{2} \tag{3.20}$$

Since the shear strain is $\gamma = \delta_x/H$, $\sigma_1 = E\epsilon_1$ =41.37 MPa. A detailed simulation with a thin-shell model of the membrane was carried out by Wong and Pellegrino [59] and the stress distribution obtained from that approach has been plotted for reference in Figure 3.6. Figure 3.7 illustrates the wrinkling pattern for an isotropic membrane; it consists of a parallelogram region with a uniform wrinkling angle of 45° plus two triangular regions that are slack. Note that there are stress concentrations at the corners B and D whereas the stress is zero at the other two corners of the membrane, A and C.

The energy variation during the Explicit simulation has been shown in Figure 3.8. The viscous dissipation is negligible (the linear viscosity coefficient was set equal to 0.005) and the kinetic energy is also small, indicating that a quasi-static simulation has been achieved. A constant strain energy level of 236.76 mJ during the second step indicates that the simulation is stable.

(a) Major principal stress (unit: MPa)

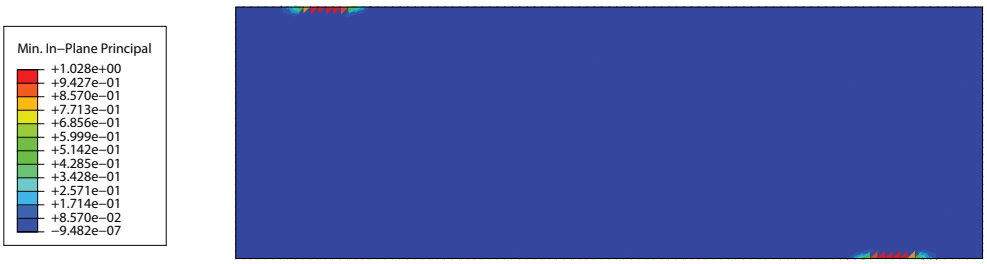

(b) Minor principal stress (unit: MPa)

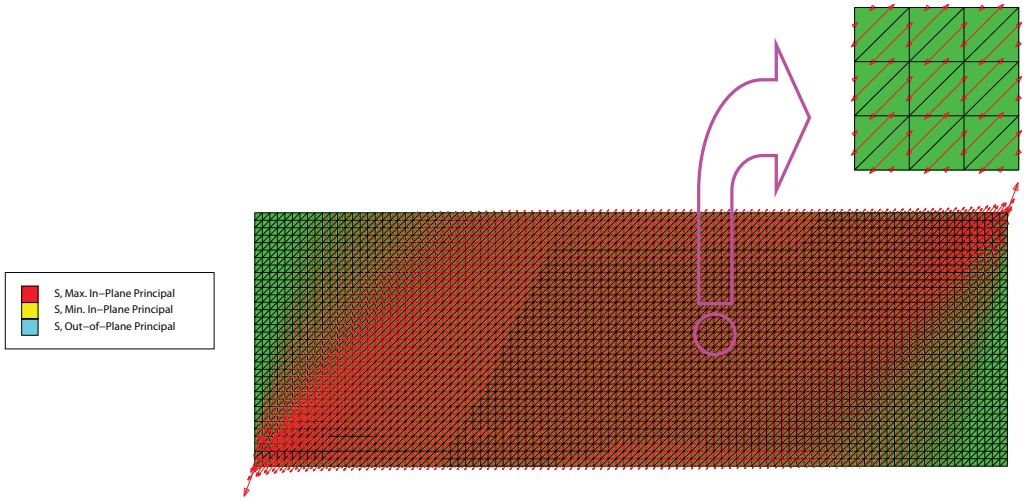

(c) Vector plot

Figure 3.5: Plot of principal stress distribution for isotropic, time-independent membrane.

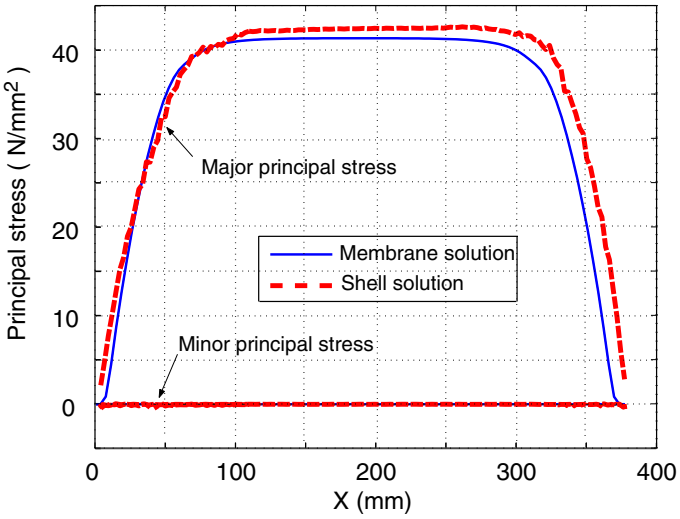

Figure 3.6: Variation of principal stresses across middle horizontal section of isotropic, time-independent membrane.

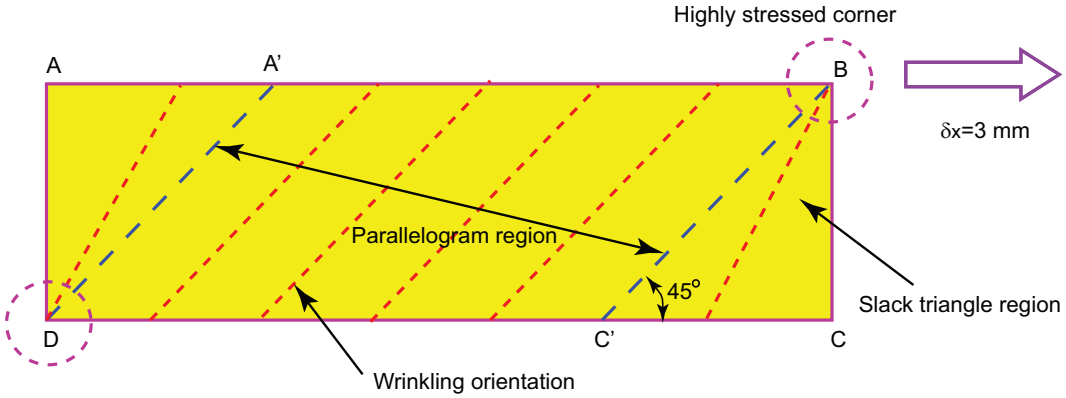

Figure 3.7: Wrinkling pattern for isotropic, time-independent membrane under simple shear.

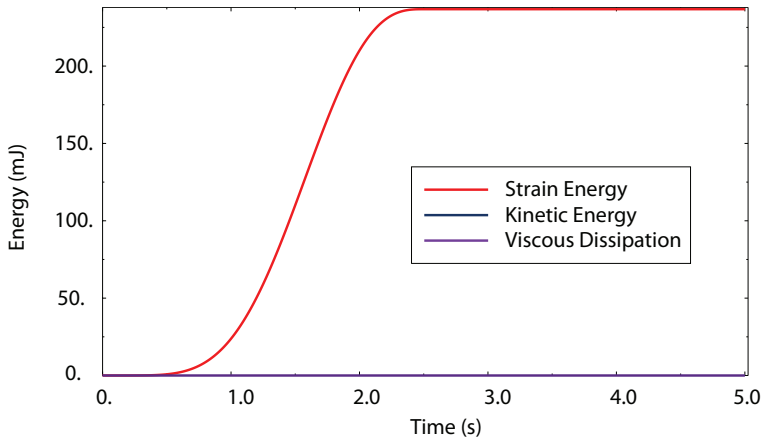

Figure 3.8: Energy variation for isotropic, time-independent membrane.

3.4 Experimental studies of viscoelastic orthotropic membranes

A rectangular membrane with exactly the same dimensions as the one considered in Section 3.3.1 and subject to the same loading condition has been tested. However, now the situation is different in the following respects: (1) the membrane is StratoFilm 420, which is an orthotropic material showing nonlinear viscoelastic effects; (2) both loading and unloading are measured and hysteretic curves obtained from experiments will be compared with results of pseudoelastic simulations; (3) after a linear ramp loading, the imposed displacement is kept constant for a certain time before unloading, to observe the viscoelastic response.

3.4.1 Shear test rig

The scheme for the shear test was based on the concept previously adopted by Jenkins [23] and then followed by Wong and Pellegrino [57]. The shear rig is shown in Figure 3.9, note that the moving edge block is attached to four linear bearings (LUI 5AL). A key step in the preparation for a test is setting up the flat membrane surface without any visible imperfections. To do this, a mist of distilled water was sprayed on a flat Perspex sheet and a piece of StratoFilm 420 with the required dimensions was put on the sheet. Then the film was lightly pressured with a hand roller to eliminate any air bubbles. The surface tension of the water at the interface holds the films against the plastic sheet. The upper and lower edges of one side of the film were glued to the fixed and moving edges of the rig, then clamping strips were glued and bolted to the other side of the film with M4 screws.

A controlled displacement of the moving edge block was imposed by means of a fine threaded screw, on the left-hand side of the rig and a force sensor (Futek LCM300) coaxial with the screw was used to measure the compressive contact force, F, between the screw and the moving edge block. A Keyence LK-G157 laser placed on the right-hand side (not shown in the figure) was used to measure the displacement δ_x and the variation of force and displacement with time were measured with a Vishay System 7000 data logger. The scanning frequency was 128 samples per second during loading and unloading and 10 per minute when the displacement was held constant. The data samples were averaged using a window of 20 data points to reduce noise.

3.4.2 Experimental procedure

StratoFilm 420 is orthotropic due to the non-uniform biaxial stretching during production. The directions of orthotropy are the machine direction, i.e. the direction in which the film is rolled, and the transverse direction. All experiments were carried out with the directions of orthotropy of the film parallel to the direction of shearing. In experiments denoted with an “M” the machine direction of the film was parallel to the direction of shearing, whereas in experiments denoted with a “T” the transverse direction of the film was parallel to the direction of shearing. For each set of experiments there were two levels of displacement magnitudes, approximately 2 mm and 3 mm; in the second set the direction of motion was also reversed,

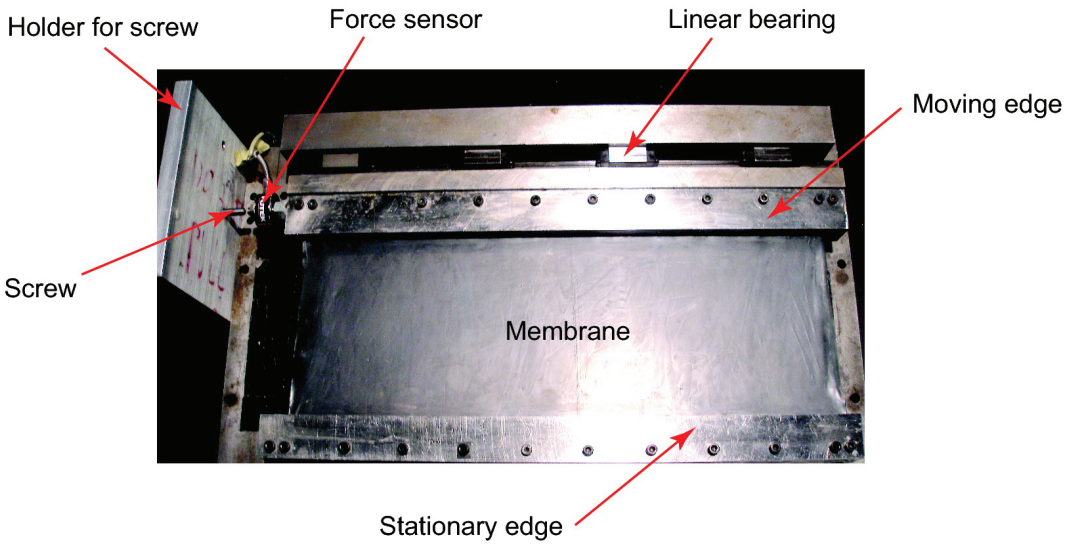

Figure 3.9: Shear rig.

after holding the displacement constant for a time T_C. The test parameters are summarized in Table 3.3.

It should be noted that at some point during the reversed direction of motion the reaction between the screw and the moving edge becomes tensile and at this point contact between the screw tip and the moving edge was lost. Hence, from this point on the motion of the moving edge was governed by the condition that the reaction force should be zero.

Table 3.3: Test parameters

Test No.	a	b	c	d
Direction of film	M	M	T	T
Displacement δ_x (mm)	2.31	3.36	2.39	3.34
Temperature T (K)	294.55	294.65	294.65	294.65
Loading type	Loading only	Loading only	Loading & unloading	Loading & unloading
Linear ramp duration t_L (s)	5.85	10.775	10.18	16.79
Constant displacement duration t_C (s)	15145.70	13582.83	22115.49	21962.0
Linear ramp duration t_U (s)	N.A.	N.A.	3.484	5.578

3.4.3 Correction for friction

The motion of the moving edge of the shear rig is resisted by friction in the linear bearings. It was assumed that the static and kinetic friction coefficients are equal and given by an expression of the type

$$f = f_0 + \mu P \tag{3.21}$$

where P is the total tension in the film, i.e. the total force in the direction perpendicular to the moving edge. f was measured on the shear rig without the film, by applying a known value of P and measuring the corresponding force needed to continuously move the sliding edge block.

The range of values of P that was considered was based on an ABAQUS simulation of the value corresponding to a film subject to a shear displacement $\delta_x = 3$ mm. Hence three levels of P were applied: 0 N, 11.121 N and 22.241 N. Since the friction force f has much smaller values than the horizontal force, a dynamic force sensor with higher precision, PCB Piezotronics Model 208C01, was used to measure the friction force.

Two sets of test results have been plotted in Figure 3.10. The linear fit, in Newtons, is given by

$$f = +1.2976 + 0.00421\ P \tag{3.22}$$

For simplicity the constant value $f = 1.298$ N was assumed, as it turned out that P is less than 22.241 N in all tests. In conclusion, the shear force acting on the film, S, can be obtained by correcting the total applied force F, measured by the force sensor during the test, see Figure 3.11 for details:

$$S = F - f \quad \text{if } \dot{\delta_x} > 0 \tag{3.23}$$

$$S = F + f \quad \text{if } \dot{\delta_x} < 0 \tag{3.24}$$

3.4.4 Results of shear tests

The wrinkling pattern observed on a film subject to a 3 mm shear displacement is shown in Figure 3.12. The wrinkles are almost evenly distributed in the central parallelogram region. The top left and bottom right corner regions are slack and so there are no wrinkles in these regions.

A correction to the measured total force has been applied, using Equations 3.23 and 3.24 with a constant friction value, have been applied to correct the shear force, respectively for the cases of loading and unloading. The results have been plotted in Figures 3.13 and 3.14.

A comparison between the shear force time variation between the four tests is shown in Figure 3.13. The increase in shear force is approximately linear during the loading ramp. Then it gradually decreases when the displacement remains constant and tends to a constant value.

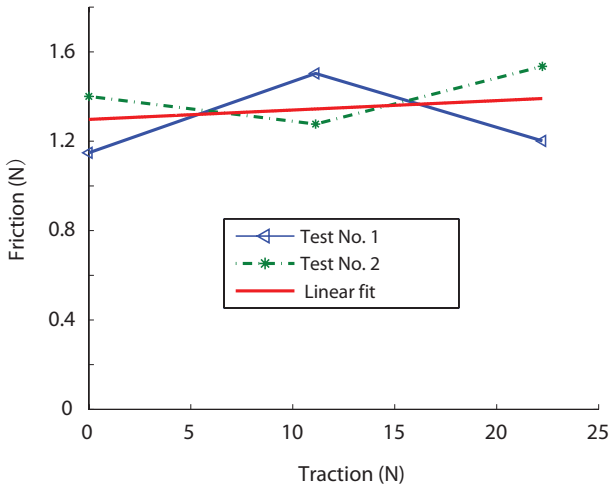

Figure 3.10: Fitting of friction force.

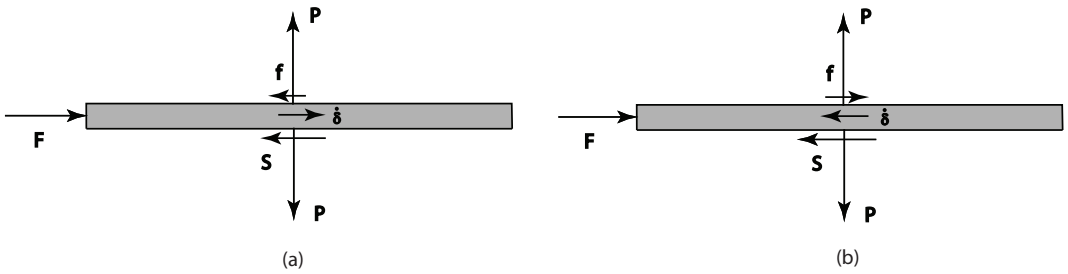

Figure 3.11: Free bodies of sliding edge block to derive correction of shear force.

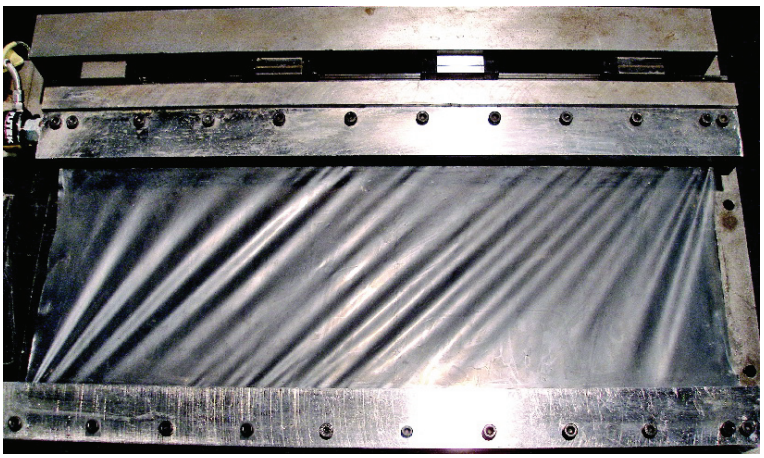

Figure 3.12: Wrinkling pattern for 38 micron thick Stratofilm 420 subject to 3 mm shear displacement.

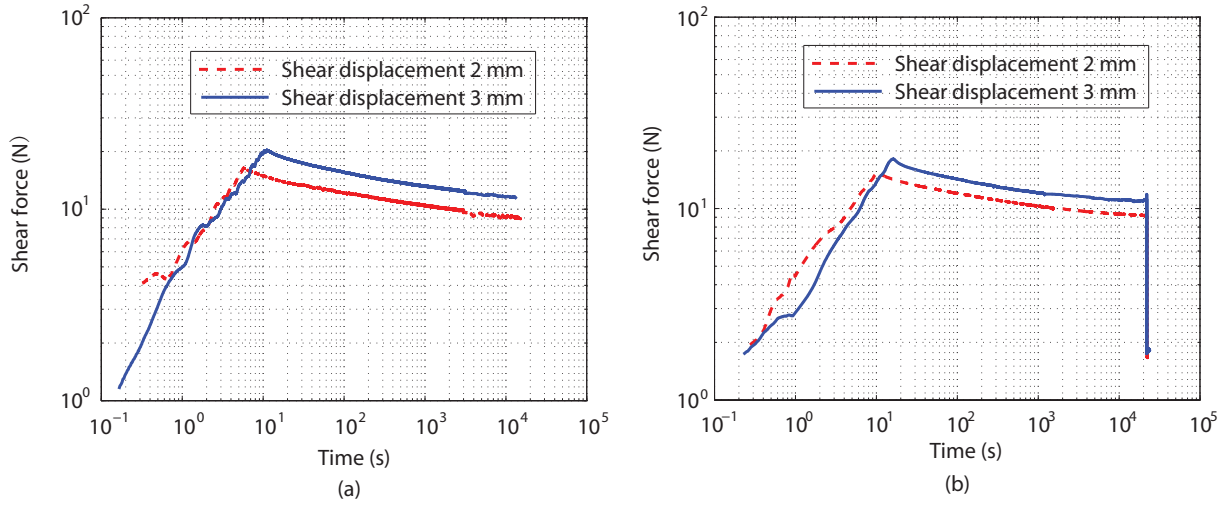

Figure 3.13: Measured time dependence of shear force, after correction for friction effects: (a) "M" machine direction parallel to direction of shearing; (b) "T" transverse direction parallel to direction of shearing.

The relationship between the shear force and displacement for the four tests is shown in Figure 3.14. The curves for total shear displacements of 2 mm and 3 mm generally follow the same shape and kinks appear at the point of initial unloading due to the shear force correction when the friction suddenly changes direction. Clearly the simplified friction correction model that has been used does not do a good job at the point of transition.

Since the differences in corresponding displacements are minor, the temperature did not change and the loading can be assumed quasi-static, it is interesting to compare the maximum shear forces in the four tests, see Table 3.4. With everything else fixed, one finds that the greater the shear displacement, the greater the shear force is. Also, for the same displacement, the film arranged with the machine direction parallel to the long edge carries a higher shear force than the film placed in the transverse direction; however the difference is generally less than 10%. This is because Stratofilm 420 has only a weak anisotropy.

Table 3.4: Maximum shear forces

Test No.	a	b	c	d
Direction of film	M	M	T	T
Displacement δ_x (mm)	2.31	3.36	2.39	3.34
Max total horizontal force F (N)	17.618	21.206	16.633	19.271
Max shear force S (N)	16.320	19.908	15.335	17.973

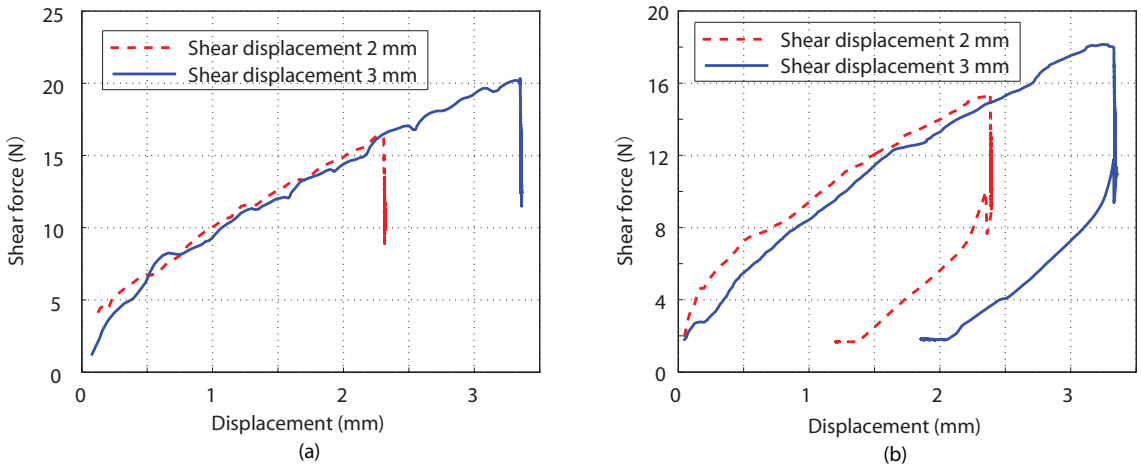

Figure 3.14: Measured force-displacement relationships, after correction for friction effects: (a) "M" machine direction parallel to direction of shearing; (b) "T" transverse direction parallel to direction of shearing.

3.5 Comparison of results and discussion

The general orthotropic viscoelastic membrane model can be tested by comparing the simulation results to the results from the experiments. The first issue is how many steps should be used to represent the time history of the imposed displacement. As an example, we have investigated the linear loading ramp for the M test with a displacement $\delta_x = 3.36$ mm, at the time $t_L = 10.775$ s. We have found that the total estimate for the shear force at this time increases from 16.445 N, to 18.970 N and 20.117 N for single-step, two-step and three-step approximations, respectively The first two results differ by 15% but the difference of the last two reduces to 6%. Taking 20.117 N as the correct solution, we have assumed that a two-step approximation for linear ramp loading is sufficiently accurate. The experimental measurement of the force at this time was 19.908 N, which confirm that the two-step solution is close to the physically correct value. At the stress-concentration corners of the membrane there is a maximum principal strain of 5.2%, which is at the limit of Rand's viscoelastic model [43, 44].

Based on this observation, Figure 3.15 shows the discretization technique that has been adopted for the actual displacement function, depending on where the chosen time t falls with respect to the ramp times.

The first thing to note from the simulation results is that the wrinkling angles are on average 44.6° and 48.3°, respectively, in the M and T cases. This difference is too small to be detected in the experiments. Figures 3.16 and 3.17 compare the relationships between total shear force and time obtained from the simulations with both uncorrected and friction corrected experimental results. During the initial loading, especially the first 1 s, the comparison shows significant differences however this is not surprising. The differences are due to the presence of inertia forces in the experimental results, due to the mass of the

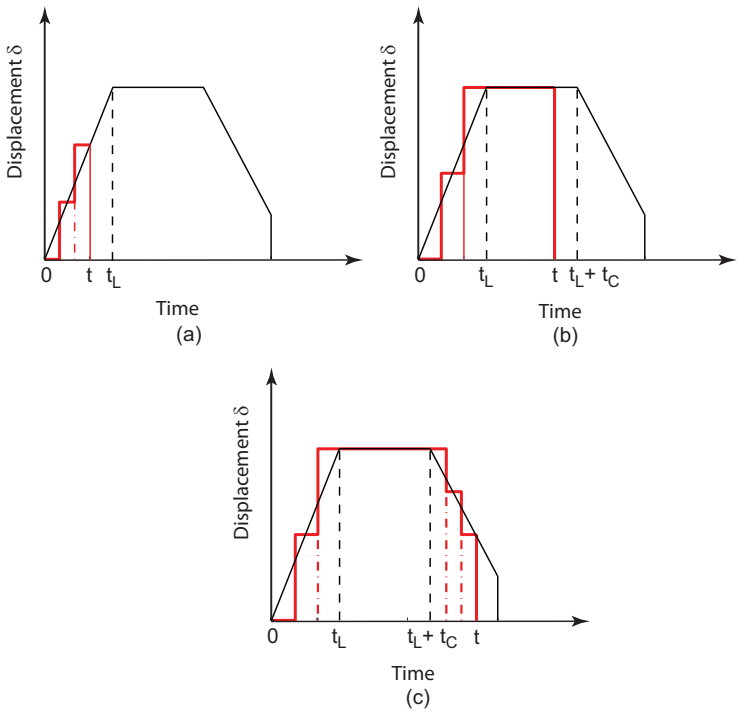

Figure 3.15: Discretization of displacement function using two-steps for each ramp; (a) case $t < t_L$; (b) case $t_L < t < t_L + t_C$; (c) case $t_L + t_C < t < t_L + t_C + t_U$.

edge block that was not included in the finite-element model, and to the fact that when the shear forces are small the force sensor is less accurate and also friction is comparatively large and so our rather rough technique for removing friction effects is not accurate. The simulations and the experimental results are much closer from $t \approx 2$ s onwards and particularly for the case $\delta_x = 3$ mm. In Figure 3.16(b) during the constant displacement phase the maximum difference between simulation and friction-corrected measured shear forces is 0.83 N, or 7.15%. In Figure 3.17(b1), the maximum difference the maximum difference is 0.58 N, or 5.28%. Figure 3.17(b2) shows a detail of the unloading part of the plot shown in Figure 3.17(b1), to provide a more detailed comparison of the unloading curves. In this range the maximum difference is 0.74 N.

Figure 3.18 shows the hysteretic relationship between shear force and displacement. Different loading and unloading paths result from the cumulative effects of viscoelasticity, which has a significant influence on the behavior of the wrinkled films.

Viscoelastic simulations based on the convolution integral would be computationally expensive for large structures undergoing large geometry changes, such as the deployment of balloons. Moreover, computing intermediate results at many stages of deployment of a balloon is of little interest as the stresses remain small until the balloon reaches its final configuration and begins to pressurize. This chapter has shown that for the balloon film SF 420 acceptable results are obtained by pseudoelastic simulations based on a two-step

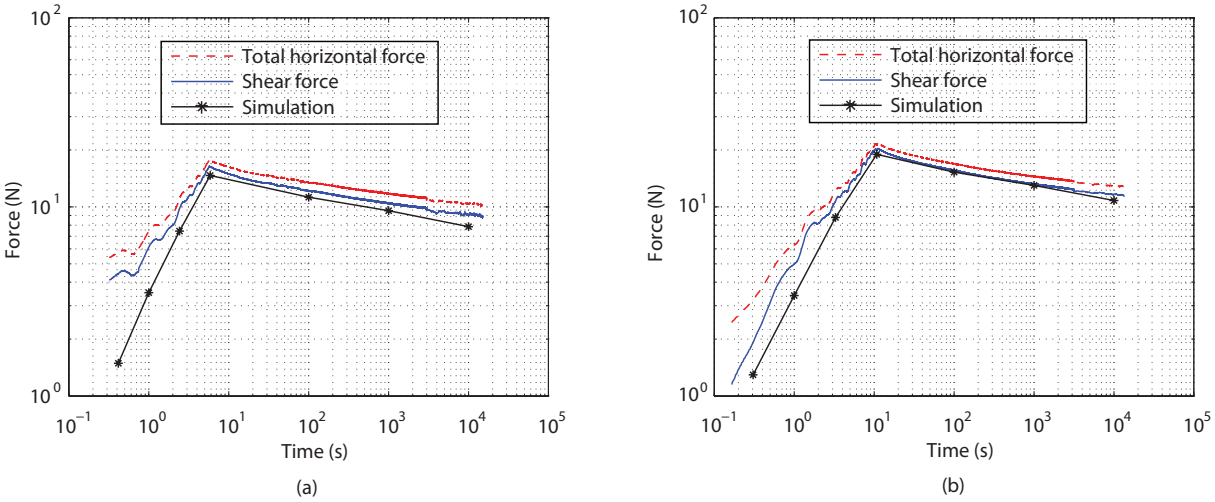

Figure 3.16: Comparison between simulation and measurement for "M" test: (a) maximum shear displacement 2 mm; (b) maximum shear displacement 3 mm.

loading function and so extension of this approach to balloon simulations should be much more efficient than attempting to predict their detailed behavior using a more detailed representation of the loading.

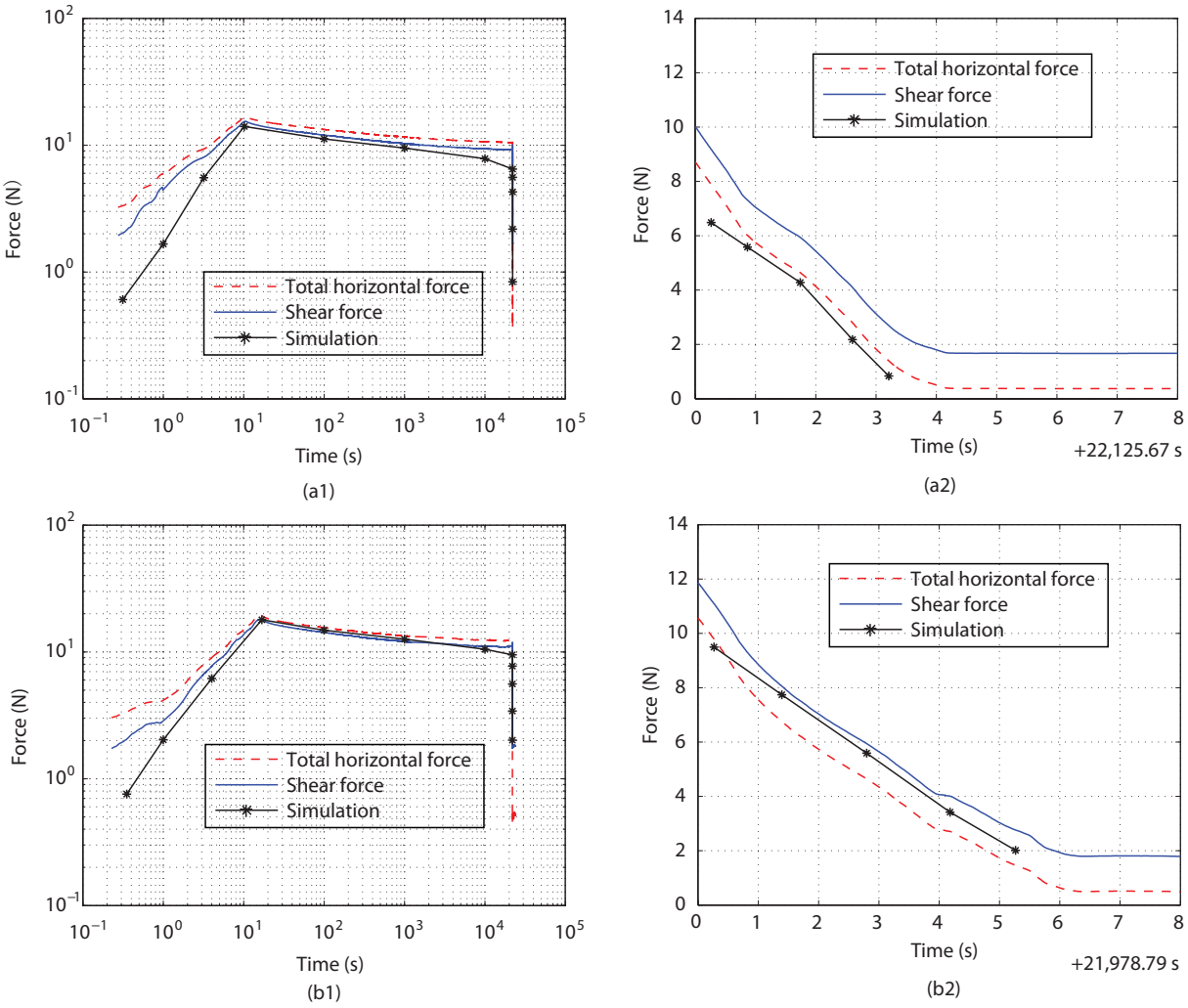

Figure 3.17: Comparison between simulation and experiment for "T" test: (a1) full behavior for maximum shear displacement 2 mm; (a2) unloading curve for maximum shear displacement 2 mm; (b1) full behavior for maximum shear displacement 3 mm; (b2) unloading curve for maximum shear displacement 3 mm.

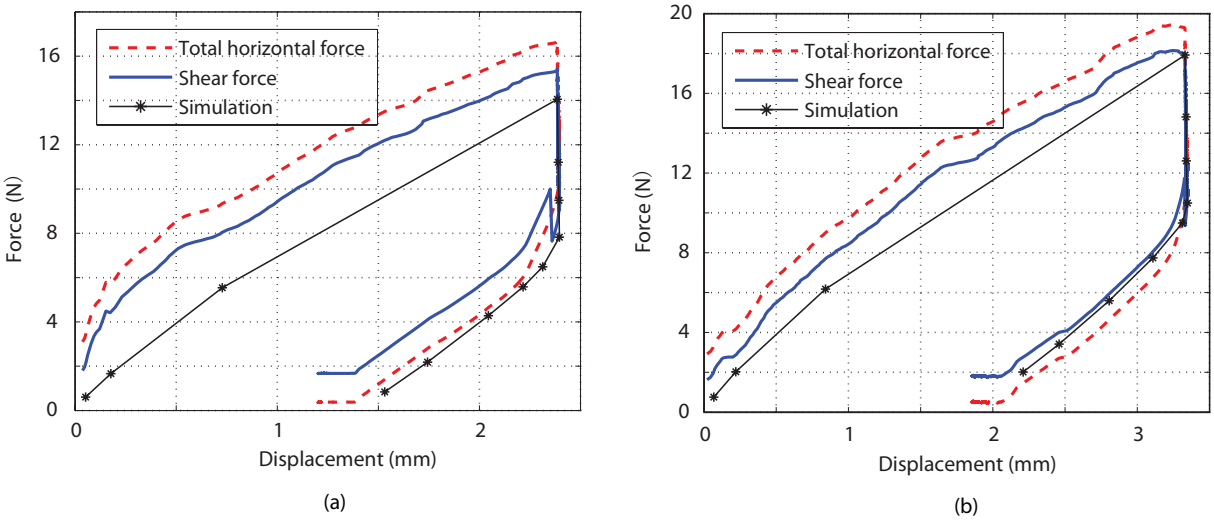

Figure 3.18: Comparison between simulation and experiment for "T" test: (a) maximum shear displacement 2 mm; (b) maximum shear displacement 3 mm.

Chapter 4

Deflation and inflation simulations of superpressure balloons

This chapter presents a fully three-dimensional finite element model of balloon structures. The model is incorporating wrinkling and frictionless contact, and is able to simulate the shapes taken up by the balloons during the final stages of their ascent and pressurization. The starting configuration for these simulations is obtained by deflating an initially symmetric balloon subject to uniform pressure. During deflation extensive wrinkling occurs and this is followed by the formation of many clefts throughout the balloon, as large amounts of balloon film are ingested within the balloon envelope. During this simulation the geometry of the balloon loses its initial symmetry. The deflation simulation is continued until the differential pressure at the bottom of the balloon has become negative, at which point the balloon is extensively clefted. The balloon is then inflated by increasing the bottom pressure while maintaining a uniform vertical pressure gradient, and the evolution of the shape and stress distribution of the balloon is studied. It is found that, depending on the particular design of the balloon, the inflation process either mirrors the deflation and so the geometry of the balloon is again symmetric at the end of the inflation, or doesn't. In the latter case, the balloon has inflated into an alternate, clefted equilibrium shape.

A set of indoor inflation experiments on one-third scale models of flight balloons was carried out in 2007 by the NASA Balloon Program Office [14]. Two of these balloons are investigated: a flat facet balloon # 6 and a hybrid design balloon # 1 where the lobe cutting pattern combines a constant bulge angle with a constant bulge radius approach, with maximum bulge angle of 98.1 ° and maximum bulge radius of 0.284 m. These two balloons show different kinds of behaviors during our simulation.

4.1 Finite element modeling

ABAQUS/Explicit is a finite element software computes the dynamic response of a structure subject to time-varying loads or boundary conditions. However, by ensuring that the loading rate is sufficiently slow, dynamic effects are sufficiently small that the response becomes effectively quasi-static. Thus the results

provided here were obtained by carrying out the quickest possible quasi-static simulations while ensuring that the kinetic energy is only a small fraction of the strain energy. Note, however, that a small amount of kinetic energy is required to allow large deformations of the balloon to take place in a reasonable amount of time, hence introducing an excessive amount of damping may lead to inaccurate results. Our finite element model incorporates several features that are specific to the analysis of balloon structures, as discussed below.

In our simulations, we consider a linearly varying distribution of differential pressure. Defining a global coordinate system with the X-axis directed upwards, the pressure is given by

$$\Delta p(X) = \Delta\rho g(X - X_D) + \Delta p_D \tag{4.1}$$

where X_D is the X-coordinate of the bottom apex, $\Delta\rho$ is the difference between the outer gas density, ρ_{out}, and the inner gas density, ρ_{in}, and Δp_D is the differential pressure at the bottom of the balloon. By varying the value of Δp_D we simulate deflation or inflation of the balloon (Δp_D decreasing or increasing, respectively).

4.1.1 Wrinkling and contact

A clefted shape of the balloon is a stable equilibrium shape that is associated with both wrinkling in the film of the balloon and contact between different parts of the balloon. A user-defined subroutine (Vumat) was used to model wrinkling in the film and thus avoid compressive stresses. A mixed wrinkling criterion based on the variable Poisson's ratio method [30], [1] was adopted. Denoting the constitutive model for the membrane by $\{\sigma\} = [D]\{\varepsilon\}$, and the major and minor principal stresses by σ_1, σ_2, this subroutine iteratively modifies the matrix D according to the state (wrinkled, taut or slack) of each element, as follows.

- $\sigma_2 > 0$: the membrane is *taut*, hence

$$D_t = \frac{E}{1-\nu^2}\begin{bmatrix} 1 & \nu & 0 \\ \nu & 1 & 0 \\ 0 & 0 & (1-\nu)/2 \end{bmatrix} \tag{4.2}$$

- $\sigma_2 \leq 0$ and $\varepsilon_1 > 0$: the membrane is *wrinkled*, hence

$$D_w = \frac{E}{4}\begin{bmatrix} 2(1+P) & 0 & Q \\ 0 & 2(1-P) & Q \\ Q & Q & 1 \end{bmatrix} \tag{4.3}$$

where $P = (\epsilon_x - \epsilon_y)/(\epsilon_1 - \epsilon_2)$ and $Q = \gamma_{xy}/(\epsilon_1 - \epsilon_2)$

- $\varepsilon_1 \leq 0$ and $\sigma_2 < 0$: the membrane is *slack* and hence $D_s = 0$

It is also essential to model contact, to prevent the penetration of any parts of the balloon through other parts. ABAQUS/Explicit can handle contact in two different ways, contact pairs and general contact. The latter was used: general contact was defined for the surface of the balloon interacting with itself, using the option "*Contact Inclusions". Unlike ABAQUS/Standard, Explicit is able to handle multiple contact surfaces without a significant overhead.

4.1.2 "No compression" for tendons

The tendons adjoining two adjacent lobes are modeled with pin-jointed two node truss elements (T3D2). A user subroutine (Vumat) is defined to simulate the tendons with no compression. The constitutive model for the tendon is given by $\sigma = D\epsilon$, where σ is uniaxial stress, ϵ is uniaxial strain, and stiffness D is iteratively updated according to the state (taut or slack) of each element, as follows.

- $\sigma > 0$: the tendon is *taut*, hence $D_t = E$
- $\sigma \leq 0$: the tendon is *slack*, hence $D_s = 0$

4.1.3 Time stepping

The central difference operator used in ABAQUS/Explicit is only conditionally stable and a conservative estimate of the stable time increment is calculated from

$$\Delta t_{stable} \leq \frac{L_{min}}{C_d}(\sqrt{1+\varepsilon_{max}^2} - \varepsilon_{max}) \tag{4.4}$$

where L_{min} is the smallest element length anywhere in the mesh, ε_{max} is the fraction of critical damping in the mode with the highest frequency and C_d is the dilatational wave speed. The dilatational wave speed C_d can be expressed for a linear elastic material as

$$C_d = \sqrt{\frac{E(1-\nu)}{\rho(1+\nu)(1-2\nu)}} \tag{4.5}$$

where ν is the Poisson's ratio, E is the Young's modulus and ρ is the current material density. Normally, Explicit will automatically calculate stable time increments. Hence when L_{min} is decreased, e.g. as an effect of existing wrinkling, or damping is increased, a smaller stable time increment will significantly extend the amount time required to carry out a simulation.

4.1.4 Bulk viscosity

The effect of bulk viscosity is to introduce damping associated with volumetric straining. ABAQUS/Explicit provides two forms of bulk viscosity: linear bulk viscosity and quadratic viscosity. Linear bulk viscosity is

found in all elements and is introduced to damp the highest element frequency. This damping is referred to as truncation frequency damping. It generates a bulk viscosity pressure p_{bv1} that is linear in the volumetric strain rate and has the form

$$p_{bv1} = b_1 \rho c_d L_e \dot{\epsilon_{vol}} \tag{4.6}$$

where b_1 is a damping coefficient (ABAQUS default=0.06), L_e is an element characteristic length, and $\dot{\epsilon_{vol}}$ is the volumetric strain rate.

ABAQUS/Explicit provides also a quadratic bulk viscosity, but only for solid continuum elements. This type of viscosity smears a shock front across several elements and is introduced to prevent elements from collapsing under extremely high velocity gradients. The resisting pressure p_{bv2} is quadratic in the volumetric strain rate

$$p_{bv2} = \rho(b_2 L_e \dot{\epsilon_{vol}})^2 \tag{4.7}$$

where b_2 is also a damping coefficient (default=1.2). The quadratic bulk viscosity is applied only if the volumetric strain rate is compressive. In Abaqus/Explicit, the damping coefficient b_1 and b_2 can be redefined from step to step. Because no solid elements are included in the balloon model, b_2 is set to zero. Linear bulk viscosity can effectively prevent high distortion of membrane elements in the wrinkled region and damp the oscillation of kinetic energy.

4.1.5 Element choice

The balloon film is modeled with thin membrane elements, which provide stiffness in the plane of the element but have no bending stiffness. Two types of membrane elements that can work with the user-defined wrinkling subroutine are available in Abaqus/Explicit: M3D3 and M3D4R. M3D4R is a 4-node quadrilateral element with reduced integration and hourglass control; M3D3 is a 3-node triangular element with full integration. Both elements have three degrees of freedom at each node. The command line "*Membrane section" can be used to define a constant section thickness. Reduced integration in the element M3D4R is primarily used to reduce the computational expense. Each reduced integration element contains only one integration point. However, the use of the reduced-integration scheme has a drawback: it can result in mesh instability, commonly referred to as "hourglass". The hourglass mode does not cause any strain and hence doesn't contribute to the energy integral. The element is unable to resist this type of deformation since it has no stiffness in this mode. In coarse meshes this zero-energy mode can propagate through the mesh, producing meaningless results. ABAQUS provides a utility tool, the enhanced hourglass control, as a remedy for hourglass problems. To activate the enhanced hourglass control, one uses the option "*SECTION CONTROLS,HOURGLASS = enhanced". This introduces a small amount of artificial "hourglass stiffness" in first-order reduced-integration elements to limit the propagation of hourglass modes.

In our simulations, a mesh of triangular elements is much preferred to a mesh of quadrilateral elements because it has higher resistance to element distortion and re-meshing can be implemented more conveniently, to improve the behavior of largely distorted elements. However, the stress distribution produced by a triangular mesh is much less smooth, even for symmetrically inflated balloons. The stress distribution predicted by the triangular mesh shows a characteristic checkerboard pattern whereas the stress distribution produced by the quadrilateral mesh is smooth, see Figure 4.1. The reason is the greater symmetry of the initial quadrilateral mesh than triangular mesh.

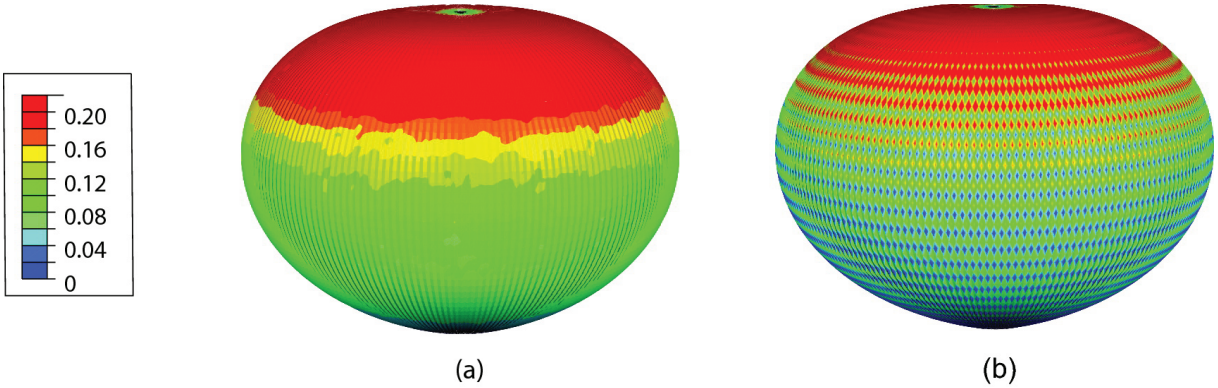

Figure 4.1: Comparison of hoop stress distribution: (a) quadrilateral element M3D4R; (b) triangular element M3D3 (Units: MPa).

4.1.6 Meshing and re-meshing

It was found that deflation simulations tend to slow down when $\Delta p_D < 0$, because the time step used in the dynamic integration became very small at this stage. Two possible reasons were investigated: first, the initial mesh is not optimized and, second, the quality of the mesh deteriorates in heavily wrinkled regions.

The reason for the first problem is that our current mesh has equal element edge lengths in the meridional direction, which leads to rather narrow elements in the polar regions. The overall quality of the mesh could be improved by designing a mesh with uniform edge length ratios, but this would require a larger number of elements which was not feasible in the present study.

The second problem can be explained as follows. Consider the element ABC shown in Figure 4.2, AB and BC are aligned with the hoop and meridional directions respectively. As the bottom pressure Δp_D decreases, the meridional tension keeps the length of BC essentially unchanged. However, if the hoop stress gradually decreases and finally becomes zero, then AB is allowed to contract and a series of meridional wrinkles will then form. As a measure of the distortion of the element, consider the aspect ratio AR, defined as the ratio between the radius of the circumcircle of the element and the radius of the inscribed circle

$$AR = \frac{r_c}{r_i} \tag{4.8}$$

The best value of AR is 0.5, for the case of an equilateral triangle, and the worst is infinite, for a triangle so elongated that one edge length is zero. In general, larger values of AR indicate more distortion from an optimal mesh.

As Δp_D is decreased in our simulation, more and more spare film becomes available in the hoop direction and if this spare material becomes concentrated in a few elements, then the aspect ratio of these elements can approach zero, as shown schematically in Figure 4.2.

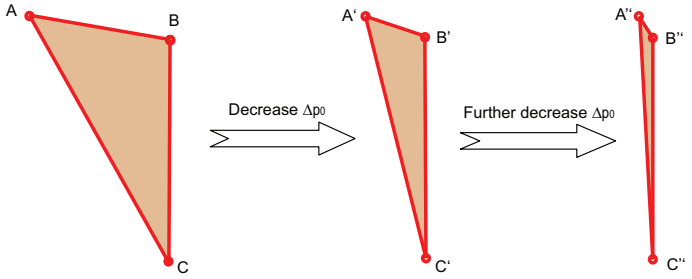

Figure 4.2: Deterioration of element aspect ratio during deflation simulation.

One possible solution is to improve the aspect ratio of this particular element by remeshing. Of the various remeshing methods, the method of element subdivision or enrichment (which is directly applicable to triangular elements) is easy to implement. The basic idea is to divide an element into elements of smaller size while keeping the original elements boundaries intact. However, excessive enrichment may reduce the overall efficiency of the analysis, hence we re-mesh only in regions where one of the edge lengths of an element has collapsed. The procedure of mesh enrichment is as follows:

1. Evaluate aspect ratio AR and minimal size L_{min} of target elements.
2. Specify maximum number of iterations and begin iteration:
   (a) Extract element I with largest AR and minimal edge length L_{min} greater than L_{lim};
   (b) Find longest edge E of element I: *If* edge E is on the boundary, split E by introducing mid-node N and then split element I, see Figure 4.3 (a); *Else* split edge E by introducing the mid-node, then split element I and also neighboring element J, see Figure 4.3 (b);
   (c) If a bar element is attached to edge E, split the bar element as well.
   (d) Calculate coordinates of new elements in reference configuration, by linear interpolation.
3. Stop when maximum number of iterations is reached or L_{min} of all target elements becomes smaller than L_{lim}.

Consider the triangles ABC and CDE in Figure 4.4. They are similar triangles and hence they have the same aspect ratio, so why is it advantageous to subdivide element ABC? The reason is explained in

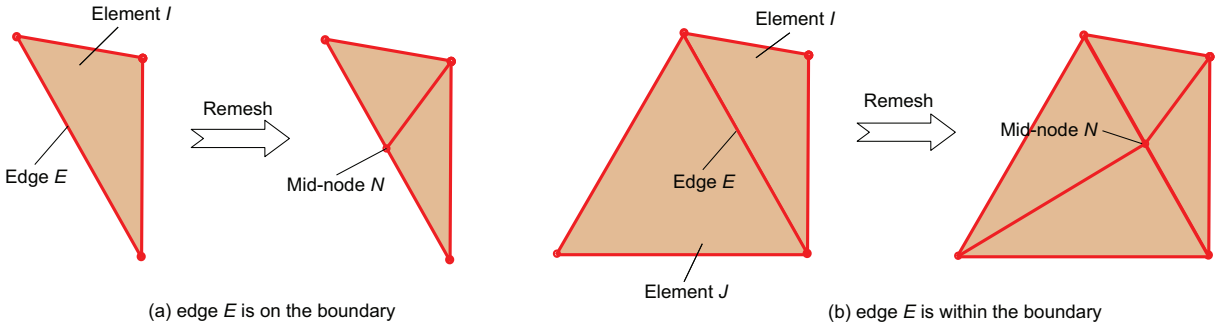

Figure 4.3: Mesh enrichment scheme.

Figure 4.4 and requires us to think about a wrinkled element where the largest principal stress, S_{max}, is about to become aligned with the meridional direction, shown by the double-arrowed dash line, and the smallest principal stress, S_{min}, is about to become zero.

When this element approaches the wrinkled state, S_{min} gradually decreases to zero, and S_{max} rotates towards the meridional direction. If we keep the original mesh, Figure 4.4(a), S_{max} will suddenly increase when Δp_D is decreased to a critical value as S_{max} becomes approximately aligned with the meridional direction. Hence, as a wrinkle is allowed to form, the distance AB in the hoop direction is allowed to shrink and so element ABC becomes highly distorted. If mesh enrichment is implemented, the biaxial stiffness of each enriched element is slightly different, e.g. element ABD has better AR and is less inclined to high distortion, so S_{max} in each of the three elements deviates somewhat from the meridional direction. Hence, the enriched region ABC is less likely to collapse because the three interacting elements have different directions of S_{max}, see Figure 4.4(b).

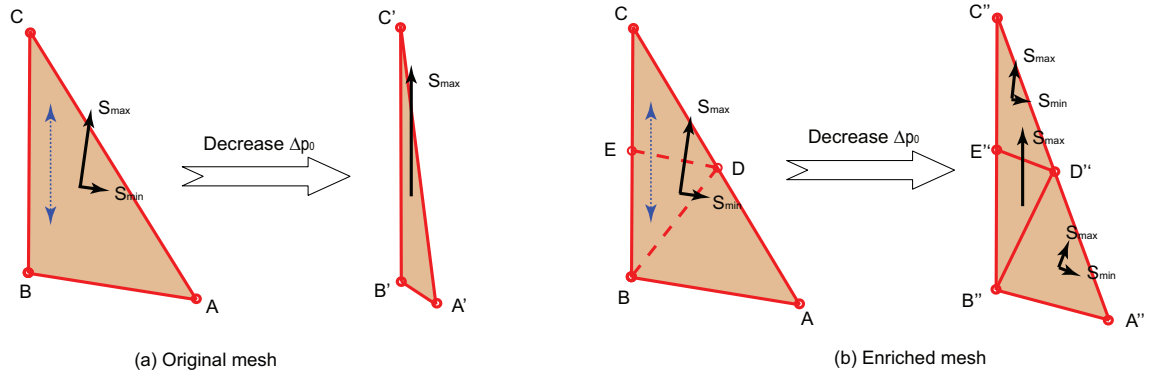

Figure 4.4: Mechanism of mesh enrichment for an element on the point of wrinkling.

4.1.7 Initial mesh geometry

The finite element simulation starts from a cyclically symmetric balloon subject to uniform pressure. The expected result of this initial analysis is a symmetrically deformed shape, however, the applied pressure should not be too high otherwise the balloon will buckle into a 3-up-3-down or 4-up-4-down mode [35].

To achieve a symmetric inflated shape, the initial mesh for the gore cutting pattern is required to be symmetric about the x-axis and the z-axis and all lobes should be identical. Different initial meshes can be considered, see Figure 4.5. In this study, scheme (b) was chosen for the triangular mesh because the triangles form tessellation of rhombuses which distributes the stiffness of the elements more uniformly. In addition, great care is needed in defining the edges of the cutting pattern accurately, because even small amounts of extra material near the apex region can substantially decrease the critical buckling pressure of the balloon.

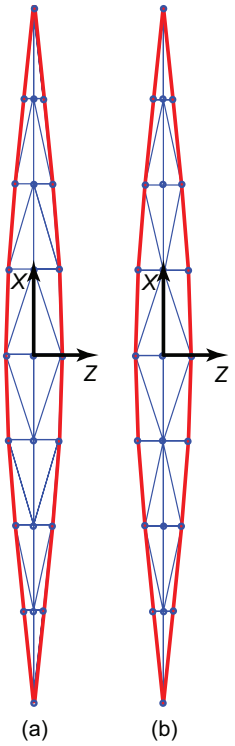

Figure 4.5: Schemes of initial triangular mesh.

4.1.8 Mapping

To define the lobe geometry, the initial geometry of the lobe was mapped onto the flat cutting pattern of the lobe (in the reference coordinate system) using the command:"Initial conditions, Type=Ref Coordinate". This command sets up a one-to-one correspondence between elements in the two coordinate systems, see Figure 4.6. The initial stresses and strains in the initial configuration are computed automatically.

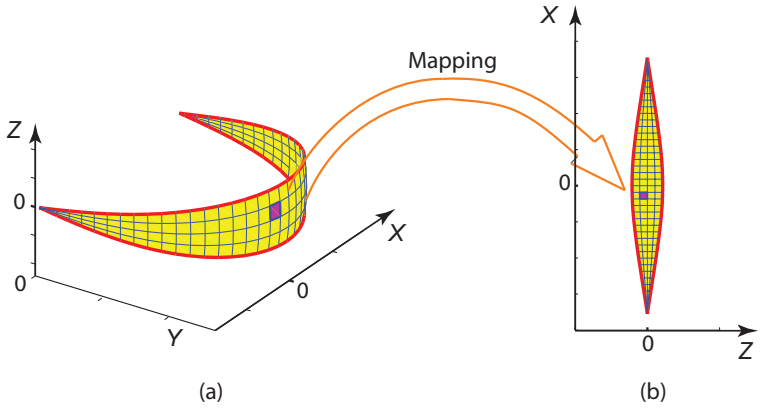

Figure 4.6: Initial geometry and reference geometry.

4.2 Special simulation techniques

This section presents a variety of techniques that have been devised to achieve better results from the simulations.

4.2.1 Large distortion of elements

As discussed in Section 4.1, some wrinkled elements collapse into a line during deflation, when the differential pressure at bottom of the balloon becomes negative and also during the subsequent inflation. Element collapse may stop the computation because ABAQUS/Explicit stops when any element is excessively distorted.

Excessive dynamic behavior during the simulation will compound this effect as very large dynamic distortions of the elements may occur. Numerical damping is used to reduce excessive oscillation, through the linear viscosity coefficient (option "*Bulk Viscosity" in ABAQUS/Explicit).

Also, elements with lower values of the aspect ratio become increasingly distorted when more wrinkles appear. If a wrinkled element has $AR > 6.7$, re-meshing will be implemented on this element and its neighbors; otherwise the element is simply deleted. In subsequent steps, the AR of elements that have been deleted is checked and any elements whose AR has become smaller than 10 are restored.

Meanwhile, the stable time increment, Δt_{stable}, is automatically decreased by ABAQUS by decreasing the minimum element size, because of wrinkling and mesh enrichment, and by increasing the viscosity coefficient, ε_{max}, according to Equation 4.4.

Note that when element enrichment and deletion are implemented, a new model with the updated geometry is constructed but the stresses are set to zero everywhere. By updating the initial mesh geometry in the reference configuration, the next analysis step will calculate the correct shape and corresponding stress distribution, for the current pressure.

4.2.2 Reversal of curvature

During inflation an axi-symmetric region of negative gaussian curvature develops near the bottom of the balloon, which leads to the formation of a roughly conical surface separated from the upper part of the balloon by a ring-like region with a high hoop stress. We have not seen these shapes in any experiments and so at present we are unsure if this behavior is physically realistic. Because the high hoop stress ring tends to prevent the formation of continuous clefts linking the bottom of the balloon to the top we have developed an iterative procedure to reduce this localized deformation.

Our basic idea to eliminate this localization is to replace the vertical constraint at the bottom of the balloon with a reaction force and to reset the stress distribution to zero throughout the balloon. While doing this we monitor the height of the balloon (which should decrease if this localized deformation region is absorbed into the smoothly curved envelope) and the largest radius of the balloon (which should decrease). This step cannot be allowed to continue indefinitely because the pressure loading on the balloon is defined in a spatial frame rather than a material frame (this is the only option currently available in ABAQUS/Explicit). Hence, even a small change in z_D will result in a change in buoyancy that needs to be equilibrated by changing the reaction at the bottom. This is addressed by an iterative algorithm to correct the pressure as follows, see also Figure 4.7:

1. Release constraint at bottom of balloon and apply vertical force equal to reaction;
2. Run simulation: balloon starts to move up and pressure distribution changes;
3. Activate constraint, apply corrected pressure and run simulation again.

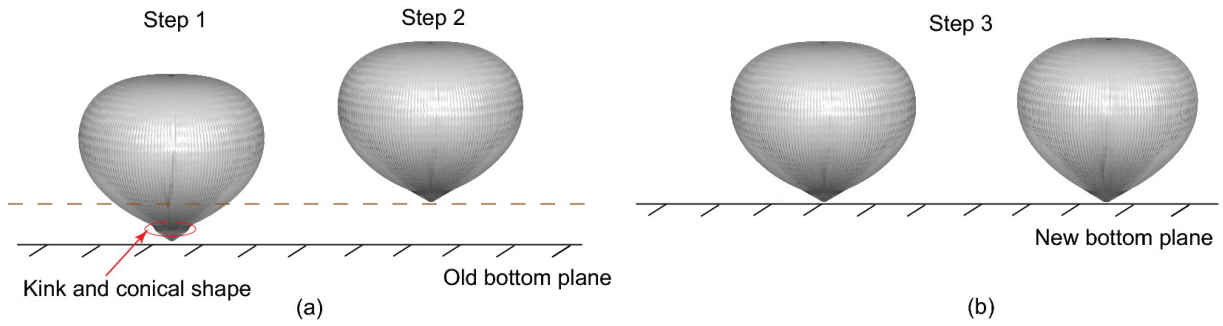

Figure 4.7: Iteration that corrects for curvature reversal: (a) Step 1 and 2 (b) Step 3.

During step 2 the pressure distribution is still referenced to the old bottom plane, and so as the balloon lifts up the pressure becomes incorrect and the buoyancy tends to increase, the kinetic energy will also rapidly increase. To avoid problems, the duration of step 2 is set sufficiently short to avoid large vertical motions of balloon. In step 3, the correct pressure distribution is again applied, with reference to the new bottom plane.

4.2.3 Convergence of balloon shapes

The shape of the cyclically symmetric balloon is varied by changing the bottom pressure Δp_D in a smooth way, but even application of the pressure change as a "smooth step" is not enough to guarantee that any shape produced by the simulation is completely converged. Hence, to test the convergence of a balloon configuration subject to a certain pressure, it is necessary to run a few additional steps with constant loading. We take a fully deployed 48 flat facet balloon as an example. During the first step, a uniform pressure is applied on the balloon surface, and the pressure magnitude is increased with a smooth step from 0 Pa to 10 Pa. Then we carry out three additional steps at a constant pressure of 10 Pa. At the beginning of each step, the stress is reset to zero and is calculated by mapping from the reference configuration to 3D balloon surface and stress equilibrium. The energy variation of the four-step simulations is shown in Figure 4.8. Although the viscous dissipation and kinetic energy are small in step 1, the simulation has not fully converged, because a large oscillation of the energy occurs in step 2 when the structure is excited by large initial out-of-balance forces. From step 2 to step 4, the dynamic effects and the viscous dissipation are suppressed, and the strain energy is gradually decreased. At the end of step 4 the structure appears to have converged in the sense that the kinetic energy and the dissipation energy are only a small portion of the strain energy, and all the energies remain almost constant with little oscillation.

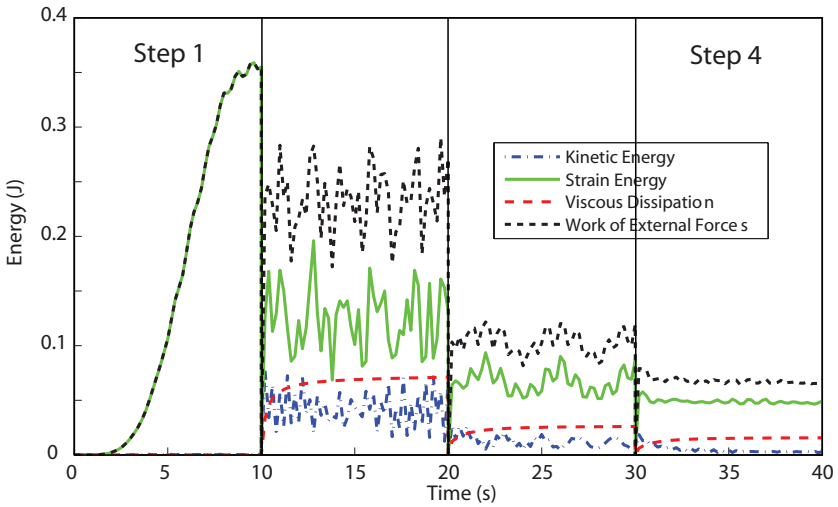

Figure 4.8: Energy variation of a fully deployed balloon.

Figure 4.9 compares the meridional and hoop stress distribution at step 1 and step 4. Initially the hoop stress is much smaller than the meridional stress, see the stress distribution at the end of step 1, as the flat facet balloon is under a uniaxial stress state. At the end of step 4, the balloon is under a biaxial stress state because the hoop stress is close to the meridional stress. This result shows that for a fully converged cyclically symmetric balloon configuration, the strain energy is minimized by biaxial tension of membrane elements rather than pure tension in the meridional direction.

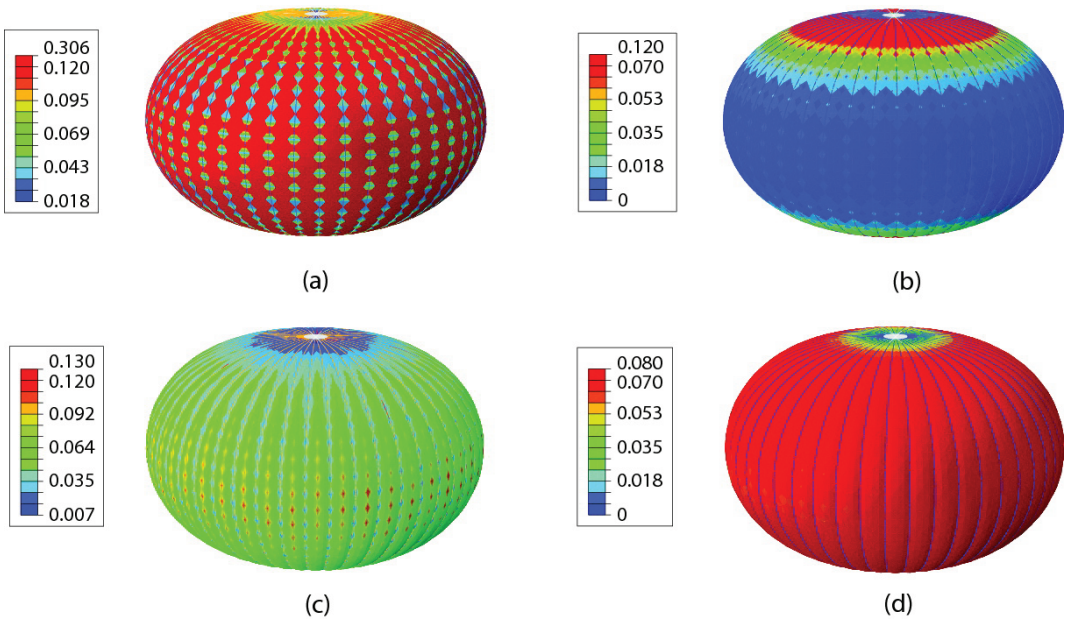

Figure 4.9: Stress distribution at step 1: (a) meridional stress; (b) hoop stress; Stress distribution at step 4: (c) meridional stress; (d) hoop stress (Units: MPa).

4.3 Construction of FE models

A simple description of the geometry of two balloons can be obtained by placing the tendons on the revolution surface of Taylor curve (i.e. the equilibrium shape of a balloon that carries uniform pressure only through meridional stress [12, 55] and by designing the gore cutting patterns such that the lobes either form circular arcs or span straight across the tendons. The following relationships [25] exist between the equatorial radius, R, and its height, X_h, volume, V, and meridional arc length, S_0:

$$X_h = 2 \times 0.5991 \times R \tag{4.9}$$

$$V = 2.7458 \times R^3 \tag{4.10}$$

$$S_0 = 2.6221 \times R \tag{4.11}$$

The values of these parameters are presented in Table 4.1. For large local meridional radius and large lobe number, the lobe shape can be described by a circular arc. As illustrated in Figure 4.10(b), r is the bulge radius. θ measures the subtended angle between adjacent meridians while α measures the bulge angle. Note that for a flat facet lobe, $R = r, \theta = \alpha$, whereas for highly lobed balloon, the above four parameters are related by

$$r \sin(\frac{\alpha}{2}) = R \sin(\frac{\theta}{2}) \tag{4.12}$$

For the case of 200 lobes, the subtended angle is $\theta = 360/200 = 1.8°$. The actual cutting pattern for the highly lobed balloon shown in Figure 4.10(c) was provided by Aerostar. Extra materials is added beyond the minimum enclosure spanning across the neighboring tendons. The nodal coordinates on the 3D balloon surface is obtained by measuring the width of the flat cutting pattern and then fitting the circular arc. Finally the lobe is copied and rotated $n - 1$ times to form a periodically symmetric surface, see Figure 4.10(a).

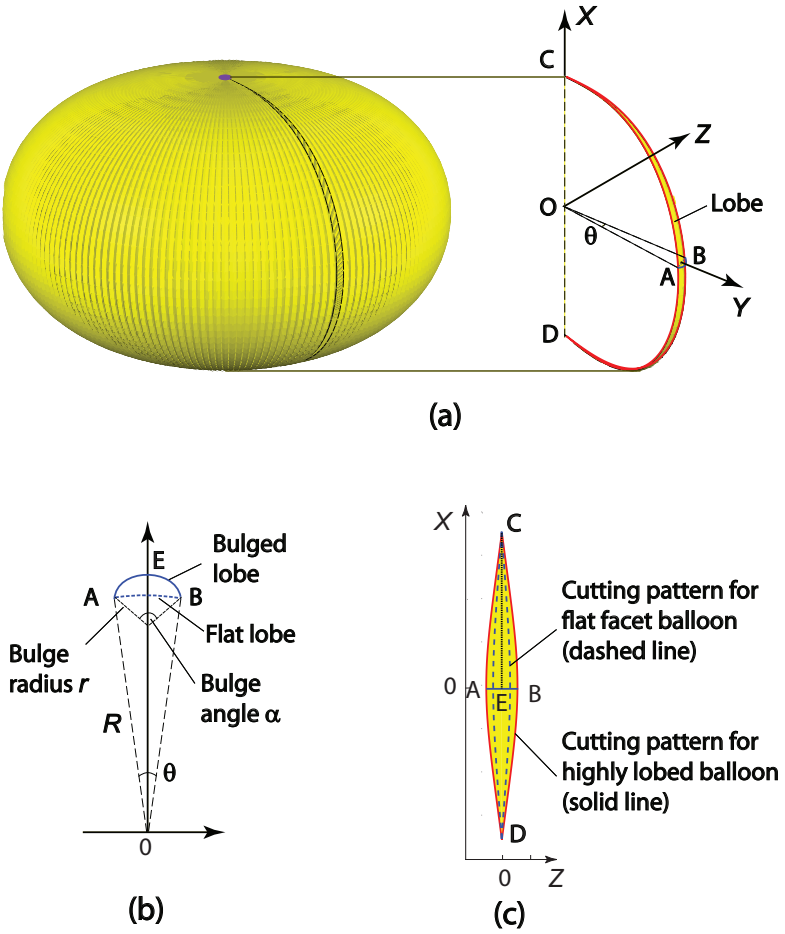

Figure 4.10: Schematic of 200-lobe balloon: (a) Initial geometry of the whole balloon (3D); (b) Equatorial cross section of one lobe; (c) Flat cutting pattern (2D).

The mesh for each lobe consists of a uniform subdivision into 68 elements between the two end fittings in the x-direction, with up to 4 triangular elements across the width. The test balloon was made of linear low density polyethylene (LLDPE) for the film and braided PBO for the tendons; their properties are given in Table 4.2.

Table 4.1: Balloon geometries

Balloon Design	Highly lobed	Flat facet
Diameter (m)	27.28	27.41
Height (m), z_h	16.20	16.42
Gore Length (m), S_0	35.45	35.93
Volume (m^3), V	6846	7060
Radius of apex plate (m)	0.406	0.406

Table 4.2: Material properties

Balloon Design	Highly lobed	Flat facet
LLDPE film		
Thickness of film, (mm)	0.013	0.013
Young's Modulus, (N/mm^2)	101	138.7
Poisson's ratio, ν	0.73	0.56
Density, ρ (kg/m^3)	920	920
PBO tendons		
Stiffness EA, (kN)	85	170
Density, ρ (kg/m)	0.006	0.012

4.4 Study of 27 m highly lobed balloon # 1

A "highly lobed" balloon with a diameter of approximately 27 m and consisting of 200 identical lobes was recently tested indoors by the NASA Superpressure Balloon team. The cutting pattern was designed to achieve an equatorial bulge angle α of 98.1° and a maximum bulge radius r of 0.284 m. The balloon was initially filled with 18.3 kg of helium at atmospheric pressure and then fully inflated by adding air. The fully inflated volume was approximately 7000 m^3 and the corresponding differential density between the air outside and the mixed helium and air inside the balloon was $\Delta\rho = 0.162$ kg/m^3. The gas inside the balloon was slowly pumped out from an orifice in the bottom plate and the shape of the balloon was observed during the ensuing deflation process. When the bottom pressure had decreased to a certain value, mixed gas (air and helium) was pumped back to fully inflate and pressurize the balloon. The test produced a visibly clefted inflated shape.

4.4.1 Results

Starting from a symmetrically inflated balloon with a uniform pressure of 10 Pa, a constant pressure gradient of 0.162 Pa/m was imposed and the bottom differential pressure was decreased in steps of decreasing size, down to −2.0 Pa. Then the balloon was gradually inflated and the bottom pressure was increased to 30 Pa while maintaining a constant pressure gradient to see to see whether the balloon would be restored to a cyclically symmetric shape.

The simulation steps are presented in Table 4.3. Note that element re-meshing was implemented at step 8

Table 4.3: Deflation and inflation simulation steps for highly lobed balloon

Step No.		Bottom pressure	Pressure gradient (Pa/m)		Loading time (s)		Viscosity coefficient b_1	
deflation	inflation	(Pa)	deflation	inflation	deflation	inflation	deflation	inflation
	31-40	30	0.162			10		0.5
	28-30	20	0.162			10		1.0
	26-27	14	0.162			5		2.0
1	23-25	10	0	0.162	20	5	0.002	2.0
2	20-22	7	0.162		20	5	0.002	2.0
3	17-19	4	0.162		20	5	0.002	2.0
4	16	1	0.162		20	5+1×5[a]	0.002	2.0
5	15	0.5	0.162		10+5[b]	5	0.005	2.0
6	14	0	0.162		10+5[b]	5+1×5[a]	0.01	2.0
7	13	-0.5	0.162		10	2.5+1×2[a]	0.025	3.0
8	12	-1	0.162		10	5	0.025	1.0
9	11	-1.5	0.162		10	5	0.10	1.2
10		-2	0.162		10		1.0	

[a]Iterations to eliminate bottom conical shape.
[b]The additional 5 seconds are at constant pressure, to test stability of result.

and step 9. The linear viscosity coefficient was kept as small as possible to avoid affecting the equilibrium shape of the structure, however its value had to be increased when the bottom pressure became negative to avoid that the computation would stop due to large distortion of the elements.

Figures 4.12 and Figures 4.13 show the corresponding distributions of meridional and hoop stress in the membrane. When the bottom pressure approaches zero, the hoop stress in the bottom region is quite small but there is a region of hoop tension near the crown of the balloon keeping the wrinkles away from the top. The formation of clefts requires the disappearance of this stabilizing "tension ring" at the top of the balloon. Once the hoop tension ring is broken at step 9 of the deflation simulation, five main clefts with bulges protruding up in the top regions appear at step 9. The bulges in the upper part of the balloon have relatively high stress, but the stress is quite low in the regions between the bulges. The inflation simulation initiates at the end of step 10 and soon the bottom part of balloon forms a surface of negative gaussian curvature. As the bottom pressure turns positive, the hoop stress increases and tensions the surface of the balloon in the hoop direction, which removes the clefts. Note that during the inflation simulation the tensile stress in the tropical region is abnormally high; the reason is not yet known. One explanation may be due to the way ABAQUS/Explicit interprets the equilibrium equations. Due to much smaller out-of-plane stiffness than in-plane stiffness for membrane elements, a large time increment is required for convergence. Even at the final pressure $\Delta p_D = 30$ Pa, the balloon remains clefted.

A visual comparison with the test observations is shown in Figure 4.11. Figure 4.11(a) compares the simulation results at the end of Step 10, which is the most clefted shape that we have simulated, with a photo taken when the pressure at the bottom of the balloon was still negative. Figure 4.11(b) compares the

simulation results at the end of Step 19. Figure 4.11(c) shows that the final shape remained clefted. These intermediate results are in agrement with the tests that had been conducted by the NASA Balloon Program, but the final shape of the clefts in our simulation does not agree with the experimental observations.

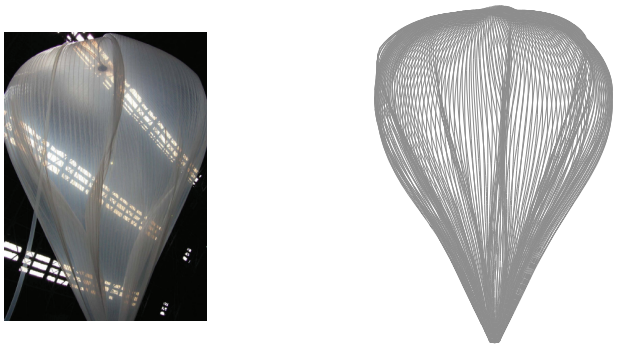

(a) Highly clefted shape

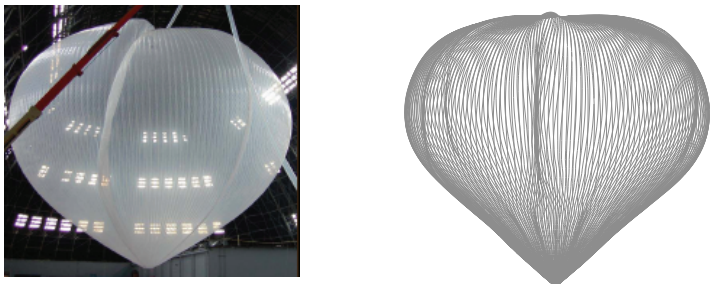

(b) Partially inflated shape

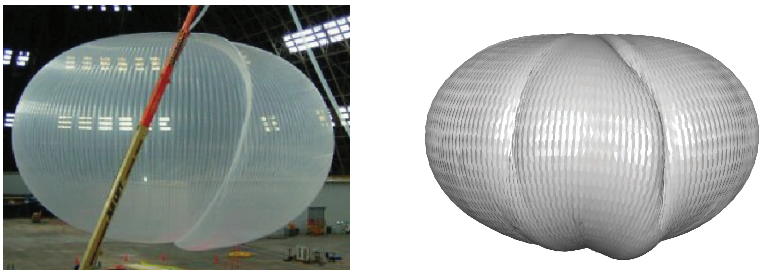

(c) Fully inflated shape

Figure 4.11: Shape comparisons for highly lobed balloon.

The key parameters that describe the shape of the highly lobed balloon quantitatively during inflation and deflation are presented in Figure 4.14. In contrast with the case of the completely deployed balloons, deflation and inflation simulations follow clearly different paths. Hence it can be argued that its inflated shapes is NOT solely determined by differential pressure. The non-uniqueness of its loading path leads to the conclusion that incomplete deployment of initial axi-symmetric shape is to be expected.

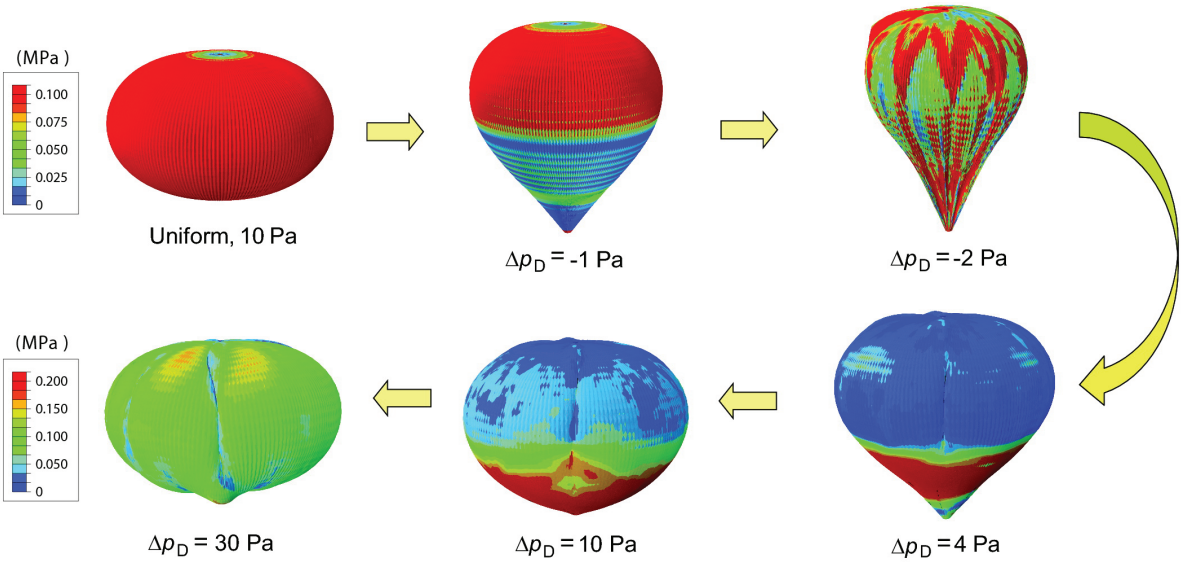

Figure 4.12: Distribution of meridional stress in highly lobed balloon (Units: MPa).

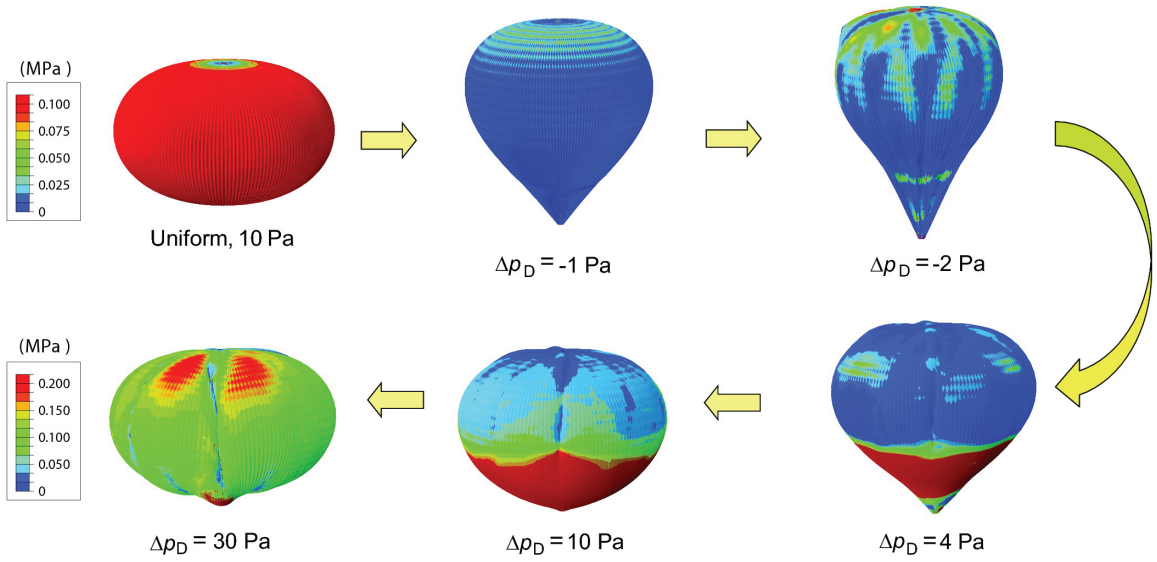

Figure 4.13: Distribution of hoop stress in highly lobed balloon (Units: MPa).

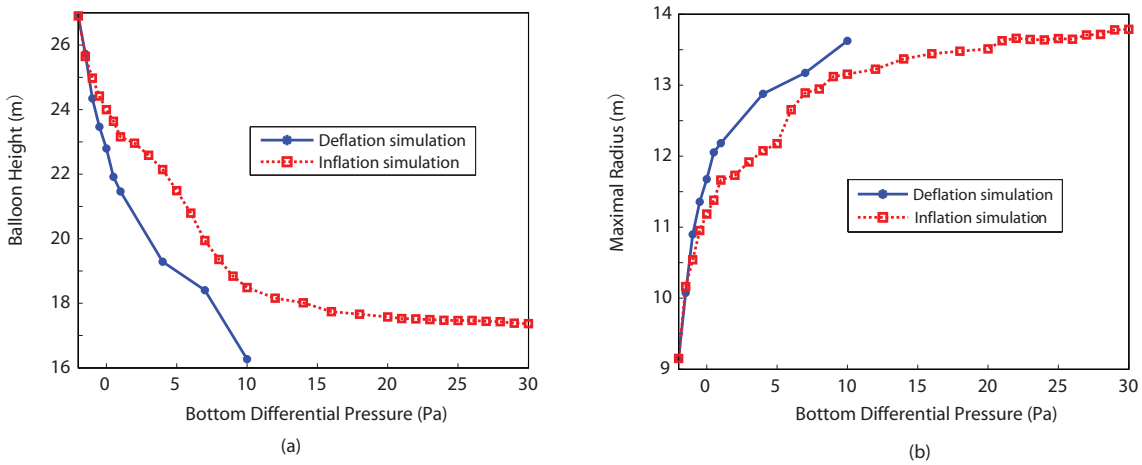

Figure 4.14: Comparison between key shape parameters of highly lobed balloon during deflation vs. inflation.

4.5 Study of 27 m flat facet balloon

A "flat facet" balloon with a diameter of approximately 27 m and consisting of 200 identical lobes was also recently tested by the NASA Superpressure Balloon team. This balloon was initially filled with 18.3 kg of helium at atmospheric pressure and then fully inflated by adding air. The fully inflated volume was approximately 7000 m^3 and the corresponding differential density between the air outside and the mixed helium and air inside the balloon was $\Delta\rho = 0.162$ kg/m^3. The indoor deflation and inflation procedure was similar to that of the highly lobed balloon; however the flat facet balloon completely deploy when it was fully pressurized.

4.5.1 Results

Starting from the fully-inflated balloon subject to a uniform pressure of 10 Pa, a constant pressure gradient of 0.162 Pa/m was imposed and then the bottom differential pressure was decreased in steps of decreasing size down to -1.5 Pa. Then the inflation simulation was started, raising the bottom pressure to -1 Pa and then tracing the reverse path back to the uniform pressure of 10 Pa, to see whether the balloon would be restored to a cyclically symmetric shape. Details on the simulation steps are presented in Table 4.4.

The linear viscosity coefficient was kept as small as possible to avoid affecting the equilibrium shape of the structure, however its value had to be increased when the bottom pressure became negative to avoid that the computation would stop due to large distortion of the elements. In general, a model using M3D3 triangular elements requires less numerical damping than a model using quadrilateral elements. A comparison between the energy variation during deflation with the two models is shown in Figure 4.15 (a) and (b). Note that the artificial energy is used to control hourglassing in the reduced integration M3D4R elements but is unnecessary in the fully integrated elements. For the quadrilateral mesh, the viscous energy, which is used

Table 4.4: Simulation steps for flat facet balloon

Step No.		Bottom pressure	Pressure gradient	Loading time (s)		Viscosity coefficient	
deflation	inflation	(Pa)	(Pa/m)	deflation	inflation	deflation	inflation
1	13	10	0	20	10+1×8[a]	0.001	0.02
2	12	7	0.162	20	10+1×8[a]	0.001	0.02
3	11	4	0.162	20	20+1×8[a]	0.002	0.02
4	10	1	0.162	20	15+3×8[a]	0.002	0.02
5		0	0.162	10+5[b]		0.002	
6	9	-0.5	0.162	15+5[b]	10	0.02	0.04
7		-1	0.162	10		0.025	
8		-1.5	0.162	10		0.025	

[a]Iterations to eliminate bottom conical shape.
[b]The additional 5 seconds are at constant pressure, to test stability of results.

to keep the simulation going and contributes mostly to the difference between the work of the external forces and the strain energy, gradually increases as the balloon becomes more unstable with more and more clefts. In contrast, in the triangular mesh the work of the external forces and the strain energy are generally in good agreement. During inflation, the constraint at the bottom of the balloon is alternately deactivated and reactivated; this induces a rather violent shaking of the bottom of the balloon which leads to rapid increases of kinetic energy, accompanied by dramatic increases and then reductions of work done and strain energy, as shown in Figure 4.15 (c).

Figures 4.16 and 4.17 show the corresponding distributions of meridional and hoop stress in the membrane. An interesting observation from these figures is that the balloon was still essentially axisymmetric at Step 5, i.e. when the bottom pressure had become zero. Also note that, although much of the balloon is wrinkled, as the hoop stress has vanished, there is still a region of hoop tension near the crown of the balloon, keeping the wrinkles away from the top. Loss of symmetry and the onset of clefting occur when the hoop stress in this upper region becomes zero. It can be seen that an S-cleft appears at step 7 and remains through step 8 but many additional, smaller wrinkles also appear. Both the S-cleft and the wrinkles gradually disappear during inflation until the surface becomes flat and the balloon regains its symmetric shape during step 13.

Table 4.5 and Figure 4.18 provide quantitative details of the deformed balloon during inflation and deflation. Although the details of the individual clefts and the wrinkle distribution are somewhat different, the overall shapes of the balloon at a given pressure, but during deflation and inflation, are very close, i.e. the deformation of the flat lobe balloon follows the same loading and unloading paths.

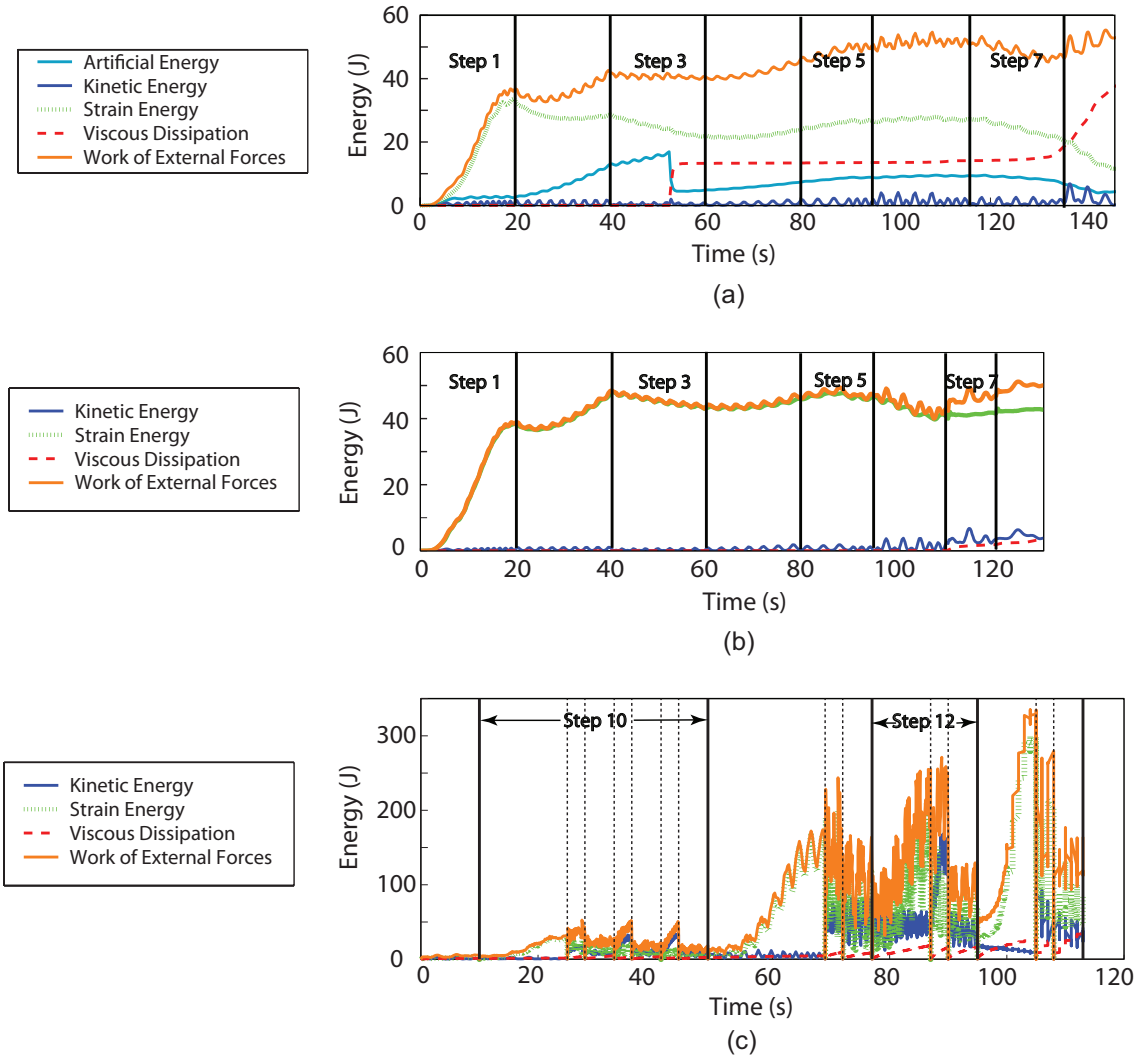

Figure 4.15: Comparison of energy variation for flat facet balloon: (a) deflation simulation using quadrilateral elements; (b) deflation simulation using triangular elements: (c) inflation simulation using triangular elements.

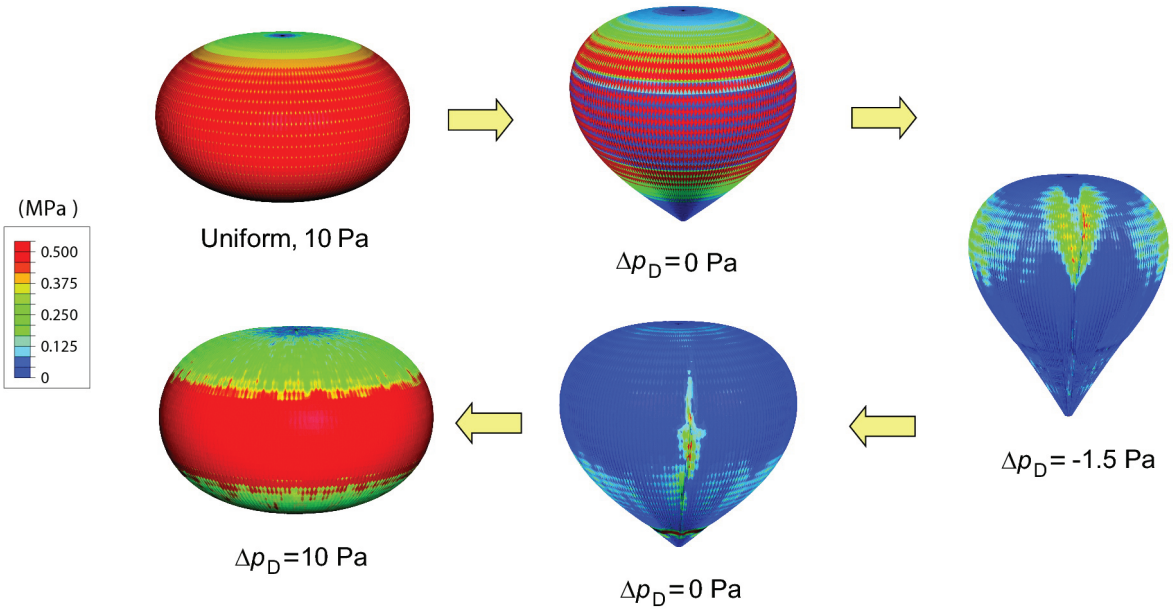

Figure 4.16: Distribution of meridional stress in flat facet balloon (Units: MPa).

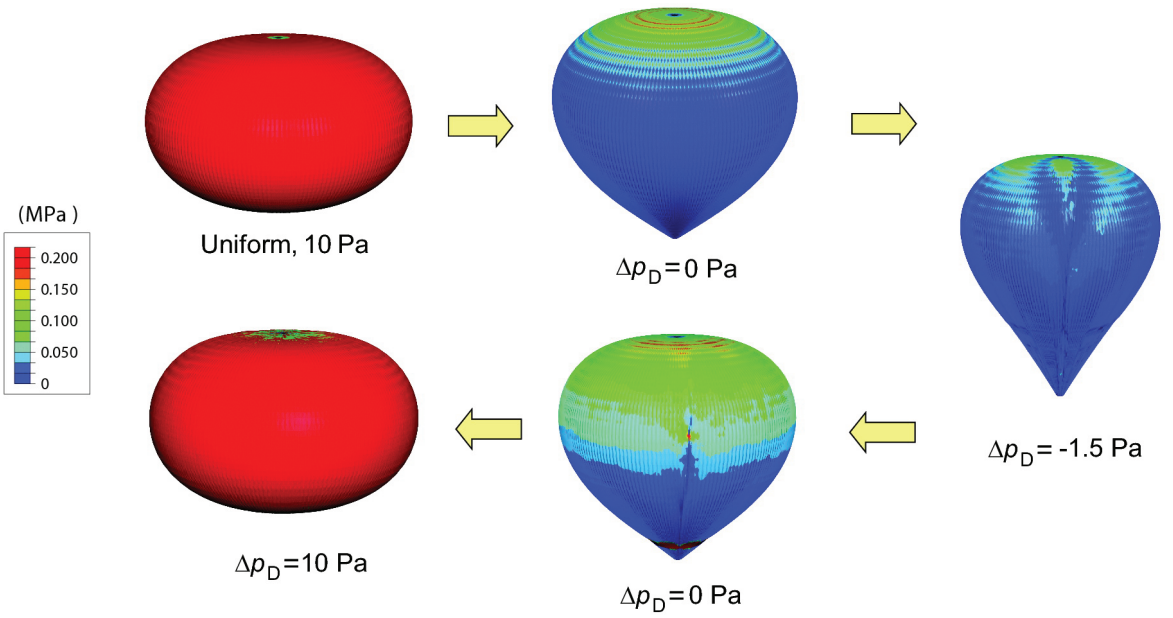

Figure 4.17: Distribution of hoop stress in flat facet balloon (Units: MPa).

Table 4.5: Predictions of key parameters of flat facet balloon

Step No.		Volume V (m^3)		Max radius (m)		Height (m)	
inflation	deflation	inflation	deflation	inflation	deflation	inflation	deflation
1	13	7078.86	7089.79	13.61	13.42	16.77	17.08
2	12	6968.69	6949.30	13.22	13.03	18.81	19.13
3	11	6847.22	6783.74	13.00	12.72	19.68	20.01
4	10	6381.72	6259.48	12.35	12.14	21.70	22.13
5		5877.62		11.77		23.12	
6	9	5565.98	5877.70	11.44	11.77	23.81	23.06
7		5029.10		10.90		24.85	
8		4315.20		10.22		25.99	

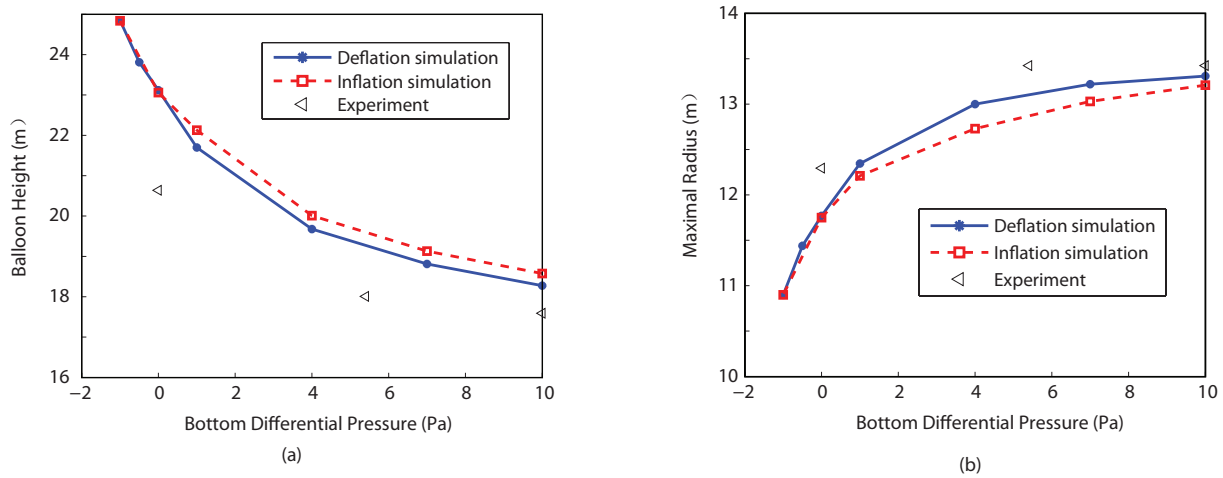

Figure 4.18: Comparison between key shape parameters of flat facet balloon during deflation vs. inflation.

Chapter 5

Clefting test

In Chapter 4, we have attacked the problem of clefting by carrying out partial deflation and reinflation simulations that start from the cyclically symmetric inflated shape. This technique was applied to 200 lobe balloons with different lobe designs, to investigate the uniqueness of their inflated shape. It was found that balloons with flatter lobes return to their original, symmetric shape while others do not. At the end of the deflation-reinflation cycle, a clefted shape was obtained for the balloon with a high lobe angle. However, the shape of the cleft did not fully agree with the experimental observations. In addition, although this analysis method produces detailed snapshots of the final stages of the inflation process that are useful to better understand clefting behavior, it is computationally quite onerous and hence unsuitable for the analysis of multiple balloon design configurations.

The purpose of this chapter is to establish a computational clefting test that can be applied to any given balloon design. The test consists in setting up the balloon in its symmetrically inflated configuration, then breaking the symmetry of this shape by artificially introducing a clefting imperfection, and finally determining the equilibrium shape of the balloon. The clefting imperfection is computed by shifting the constraint at the bottom of the balloon and removing the pressure in the bottom region, below the shifted constraint. Thus the equilibrium shape of the balloon becomes asymmetric and a large cleft appears. Once this disturbance has been introduced, the bottom constraint is returned to the bottom apex and a uniform pressure is applied to the whole balloon. Wrinkling and frictionless contact are included in the analysis.

Three representative examples from the set of one-third scale models tested by NASA Balloon Program Office have been chosen for our clefting test: (1) balloon # 1 with maximum bulge angle of 98.1° and maximum bulge radius of 0.284 m; (2) balloon # 4 with maximum bulge angle of 55°; (3) balloon # 5 with maximum bulge angle of 90°. In the tests balloon # 1 remained clefted, with a typical S-cleft at a pressure of 10 Pa, while the other two balloons deployed completely.

5.1 Finite element modeling

The finite element model incorporates similar modeling features and special simulation techniques to those discussed in Section 4.1 and Section 4.2. The initial balloon shape is assumed to be n-fold symmetric. The geometric parameters of the three test balloons are presented in Table 5.1. The balloon film is made of Linear Low Density Polyethylene (LLDPE), which is a visco-elastic material, whose behavior depends on stress σ, temperature T and loading time t. Rand [43, 44] developed a nonlinear viscoelastic constitutive model for this film material based on Schapery's theory and in Section 3.1.1 we introduced an approximate pseudo-elastic constitutive model that allows for visco-elastic effects in a simplified way. The anisotropy of the balloon film is sufficiently weak that an isotropic wrinkling model can be assumed. The Young's Modulus and Poisson's ratio are averaged between the machine direction and the transverse direction of the film. In the present case we have determined that for a balloon subject to uniform pressure $\Delta p = 10$ Pa, at room temperature $T = 293$ K for $t = 1$ hour an isotropic pseudo-elastic modulus of approximately 250 MPa can be assumed. The tendons are made of braided PBO. Their material properties are given in Table 5.2. Details of the finite element model of a balloon have been presented are shown in Section 4.3.

Table 5.1: Geometry of super-pressure balloons

Balloon No.	1	4	5
Bulge angle	98°	55°	90°
Diameter (m)	27.25	27.50	27.46
Height (m), z_h	16.20	16.42	16.35
Gore Length (m), S_0	35.45	35.93	35.78
Volume (m^3), V	6842	7092	7021
Radius of apex plate (m)	0.406	0.406	0.406

Table 5.2: Pseudo-elastic material properties

LLDPE film	
Thickness of film, (mm)	0.013
Young's Modulus, (N/mm^2)	250
Poisson's ratio, ν	0.678
Density, ρ (kg/m^3)	920
PBO tendons	
Stiffness EA, (kN)	85
Density, ρ (kg/m)	0.006

5.1.1 Constraint shift method

The implementation of the constraint shift method for the clefting test can be divided into two steps, as follows. In Step 1 of the analysis, a clefting perturbation is introduced by the following steps: (i) the balloon

is constrained at a single offset point F, at a radial distance from the axis of one-third the radius at the equator; (ii) a positive lift is created by assigning the non-uniform pressure $\Delta p = \Delta p_D + \gamma(x - x_D)$ where D is the bottom apex point and $\gamma = \Delta\rho g$, where $\Delta\rho$ is the relative density of the balloon gas, and g is the gravity acceleration; and (iii) the symmetric equilibrium shape is destabilized by setting $\Delta p = 0$ in the bottom region Ω_1, shown in Figure 5.1. Step 1 of our analysis consists in finding the equilibrium shape of the balloon for these conditions. In step 2 of the analysis the constraint is moved to the central point O at the bottom of the balloon and the non-zero pressure distribution Δp is applied to the whole balloon, to determine if a clefted shape is a possible equilibrium configuration for the balloon. This step is actually divided into a series of sub-steps with gradually decreasing numerical damping, until convergence to the final equilibrium shape is obtained.

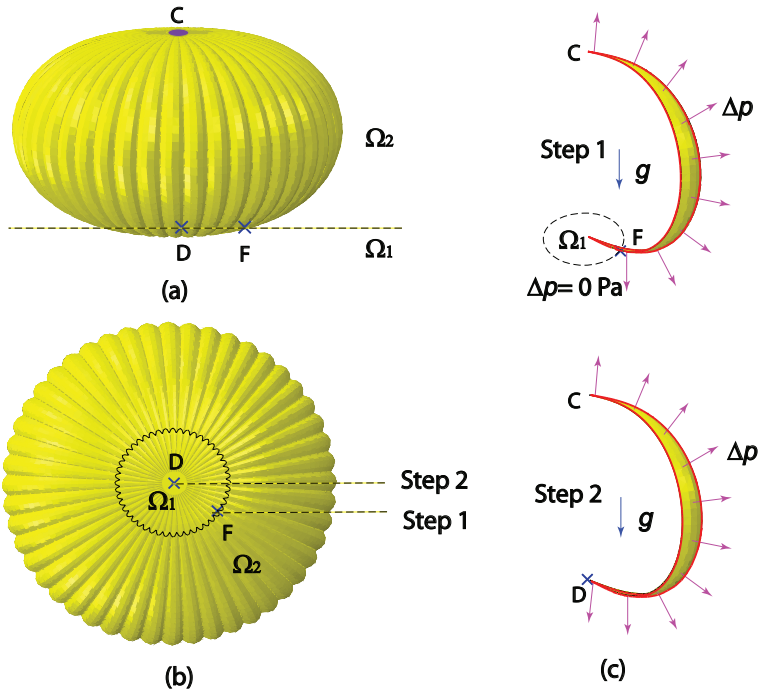

Figure 5.1: Schematic of loading and boundary conditions: (a) side view; (b) bottom view; (c) pressure Δp on one lobe.

5.1.2 Simulation details

The test balloon was modeled using the full integration three-dimensional, triangular elements M3D3 for the balloon film and three-dimensional, two-node pin-jointed bars T3D2 for the tendons. The mesh for each lobe consisted of a uniform subdivision into 68 elements between the two end fittings in the x-direction, with up to 4 triangular elements across the width.

Boundary conditions for the unperturbed model were as follows: the three translational degrees of freedom of the node at the bottom of the balloon were fixed. The two in-plane translational degrees of freedom of

the node at the crown of balloon were also fixed. All other degrees of freedom were left unrestrained.

To define the lobe geometry, the initial geometry of the lobe was mapped onto the flat cutting pattern of the lobe (in the reference coordinate system) using the command:"Initial conditions, Type=Ref Coordinate". This command sets up a one-to-one correspondence between elements in the two coordinate systems so that the initial stresses and strains in the initial configuration are computed automatically.

A user-defined subroutine (Vumat) for ABAQUS/Explicit was used to model wrinkling in the film and thus avoid compressive stresses. The mixed wrinkling criterion based on the variable Poisson's ratio method, presented in Section 4.1.1, was adopted. Also the user subroutine (Vumat) defined no compression model for the truss elements T3D2 to simulate the tendons, presented in Section 4.1.2.

It is also essential to model contact, to prevent the penetration of different parts of the membrane through other parts. General contact was defined for the surface of the balloon interacting with itself, using the option "*Contact Inclusions".

During the simulation the rate of variation of any loads has to be sufficiently slow that the kinetic energy in the whole structure is negligibly small; also, the time-step increment has to be sufficiently small as explained in Section 4.1.3. ABAQUS/Explicit will automatically calculate these increments. Linear bulk viscosity, defined by the linear viscosity coefficient b_1 defined in Section 4.1.4, is introduced to dampen any oscillations. This enhances the stability of the computation but requires smaller time increments.

It was found that the simulations tend to slow down when the initial axi-symmetric configuration was perturbed by clefting, because the time increment used in the dynamic integration became very small at this stage. The main reason was that the quality of the mesh deteriorates in heavily wrinkled regions, as was explained in detail in Section 4.1.6. Elements with acceptable values of AR initially may become increasingly distorted during the course of the simulation. If a wrinkled element has $AR > 10$ it is simply deleted. In subsequent steps, the AR of elements that have been deleted is checked and any elements whose AR has become smaller than 6.7 are restored.

Note that when element deletion is implemented, a new model with the updated geometry is constructed and the stresses are set to zero everywhere. By updating the initial mesh geometry in the reference configuration, the next analysis step will calculate the correct shape and corresponding stress distribution, for the current pressure. The dynamic disturbance introduced by this procedure is usually due to the stress having been set to zero, because the current configuration is largely unchanged, only the element mesh has been altered. Compared to the deflation and inflation method, we don't reach a heavily wrinkled configuration with large change of overall shape as initial perturbed configuration for the second step, hence the simulation becomes smoother because the elements are less distorted. Therefore, the special simulation technique to deal with remeshing and reversal of curvature are no longer necessary.

Table 5.3: Constraint shift simulation steps for balloon # 1

Step		Loading time (s)	Viscosity coefficient
Step No.	Substep No.		
1	1	8.0	0.4
2	2	5.0	2.0
	3	5.0	1.0
	4	5.0	0.5

5.2 Results for Balloon # 1 with 98° Bulge Angle

Following the procedures described in Sections 5.1.1, in step 1 of the analysis the bottom pressure was set at $\Delta p_D = 10$ Pa and a constant gradient 0.162 Pa/m was imposed in the domain Ω_1, while in step 2, the same pressure distribution was applied over the whole domain $\Omega_1 \bigcap \Omega_2$. Gravity g= 9.8m/s^2 was also included in both steps. Step 2 was actually divided into a series of substeps with gradually decreased viscosity coefficients until the final equilibrium shape was obtained. The simulation steps are presented in Table 5.3.

Figure 5.2 shows the energy variation during the two-step simulations. The bottom pressure Δp varies smoothly from 0 Pa to 10 Pa during step 1 and then remains constant. Oscillations in the kinetic energy and viscous dissipation indicate that the simulation results during step 1 are unstable. The subsequent three substeps were restarted by constructing a new model with the updated geometry from the end of the previous substep while setting the stress to zero everywhere. The strain energy remained nearly constant while the kinetic energy was stabilized.

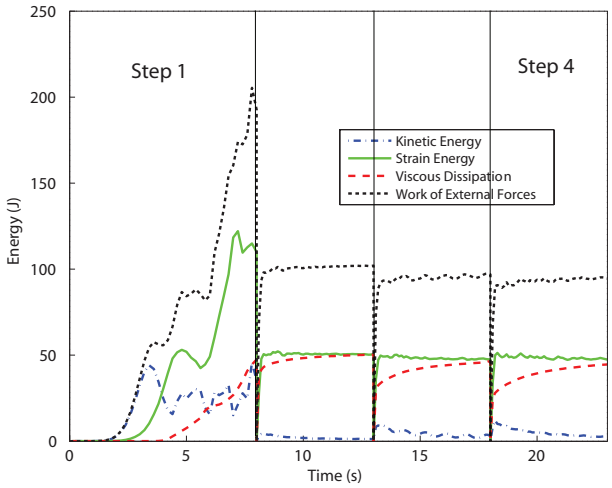

Figure 5.2: Energy variation for balloon # 1.

For the deformed configuration, the top end fitting doesn't move, whereas the bottom end fitting has a large sideways shift Δr =0.259 m from X-axis considering the radius of the bottom apex is 0.406 m. Also both of the end fittings have no rotation. The 3D cartesian coordinates of each node are converted to

cylindrical coordinates. The cylindrical coordinates are corrected due to the slip of the vertical axis linking between the centers of top and bottom end fittings. The center of each cross section of the balloon is obtained by linear interpolation between the coordinates of the top and bottom apex. A detailed understanding of the deformation from the original, symmetric shape to the final clefted configuration can be obtained from the plots in Figure 5.3(a-c), showing the components of the nodal displacements in the cylindrical coordinate system X, r, θ.

The plot of axial displacement ΔX, Figure 5.3(a), shows a high degree of localization near the cleft, upward by around 0.8 m (red) on the left and downward by around 0.7 m (blue) on the right. The plot of Δr, Figure 5.3(b), shows that the balloon has expanded radially almost everywhere: the average values of Δr are $\overline{\Delta r} = +0.018$ m over $\theta = (-180, -20)$ and $\overline{\Delta r} = +0.020$ m over $(25, 180)$ deg. However, the cleft involves a mostly inward displacement, with $\overline{\Delta r} = -0.907$ m over the large blue region, and a smaller outward displacement, with $\overline{\Delta r} = +0.0209$ m over the dark red region. The plot of change in azimuth angle, Figure 5.3(c), shows an approximately linear variation in the circumferential direction, in the range -9 deg to $+6.5$ deg. The jump of 15.5 deg across the cleft indicates that approximately $15.5 \times 200/360 = 8.6$ lobes have been ingested in the cleft.

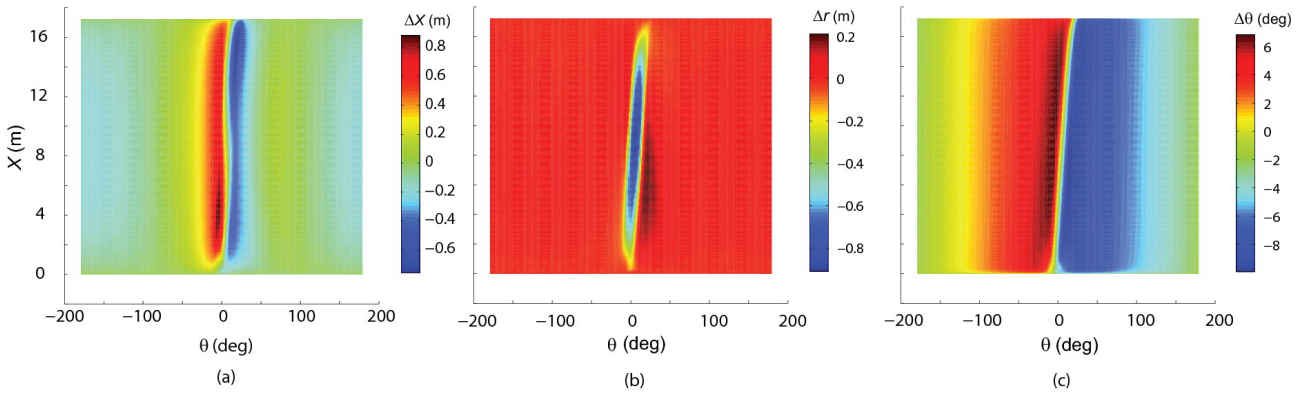

Figure 5.3: Displacement field with respect to undeformed configuration of Balloon #1: (a) variation of vertical coordinate ΔX; (b) radius Δr; (c) azimuth angle $\Delta\theta$.

Figure 5.4(a) shows a plot of the volume variation between the deformed geometry and the undeformed geometry for each small element i, ΔV_i, given by the expression $\Delta V_i = \overline{S}_i \cdot \overline{d}_i$, where $\overline{S}_i$ is the vector of area for one finite element and $\overline{d}_i$ is displacement vector from the center of undeformed element to the center of deformed element. The sum of each increased volume represents the total volume variation from the undeformed configuration to the deformed configuration. Thus we have

$$\Delta V = \sum_i \Delta V_i = 62.18 \text{ m}^3 \tag{5.1}$$

Figure 5.4(b) shows the distribution of summation of elementary volume increase for each lobe $\sum \Delta V_i$

across the azimuth angle θ. It can be verified that integration of $\sum \Delta V_i$ over θ is equal to 62.18 m^3.

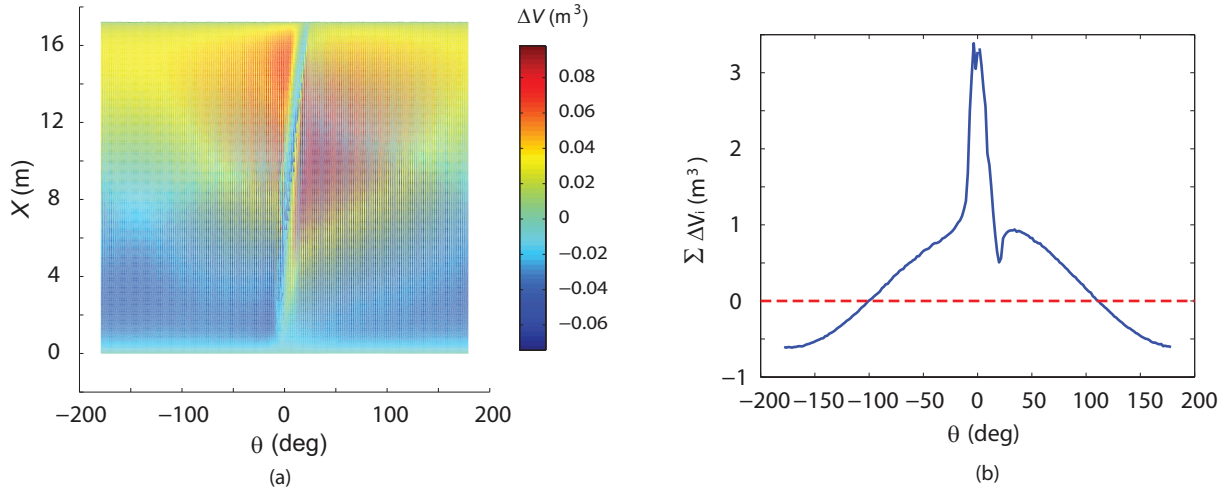

Figure 5.4: Distribution of volume variation from undeformed configuration of Balloon #1 (a) elementary volume increase ΔV_i; (b) distribution of volume variation in each lobe $\sum \Delta V_i$ vs. θ .

Figure 5.5 shows the in-plane deformation of three selected tendons on either side of the cleft. The tendon at the center of the cleft, labeled 0, has deformed symmetrically; the tendons on the left (labeled L1, L2, etc.) have sheared upwards and the tendons to the right (R1, R2, etc.) have sheared downwards. The amount of shearing is greatest for the fourth tendons (L4 and R4) and decays to almost zero in the twelfth tendons (L12 and R12). It can be seen each tendon has the same values of azimuth angle θ at both end-fittings, and that most of the tendons start off from these fittings at an angle of about +/- 5 deg to the radius. Figure 5.5(b)-(h) shows r-X profiles of these characteristic tendons. Red solid lines denote the current configuration of clefted tendons, while black dash lines denote the reference configuration of the original unclefted tendons. Asterisks mark equator. We can now see, e.g., that there are large displacements when the tendons are inside the cleft. Tendons on the left move upwards, whereas tendons on the right move downwards.

Figure 5.6 and Figure 5.7 show the deformed field by means of a horizontal grid. There are 68 uniformly spaced divisions along the meridional direction of tendons, i.e., 69 horizontal grid lines in total. The mid-line at equator is labeled as "0", and the top and the bottom tendons are labeled as "T" and "B" respectively. Every 8 intervals a grid line is marked with a bold line. We can see from both 2D and 3D figures that the left tendons in the top region bulge outwards, whereas the right tendons in the bottom region bulge outwards. Note that large amount of shearing occurs in the cleft.

Figure 5.8 shows the migration towards the cleft of 25 tendons. These tendons show very similar deformation features: the points at either end of each tendon cannot move and so the tendons bow towards the cleft by 6 to 8 deg; when they reach the cleft, they turn and follow the cleft direction. The lines marking the tendons in this plot have been color-coded to show the variation in the force magnitude: away from the cleft

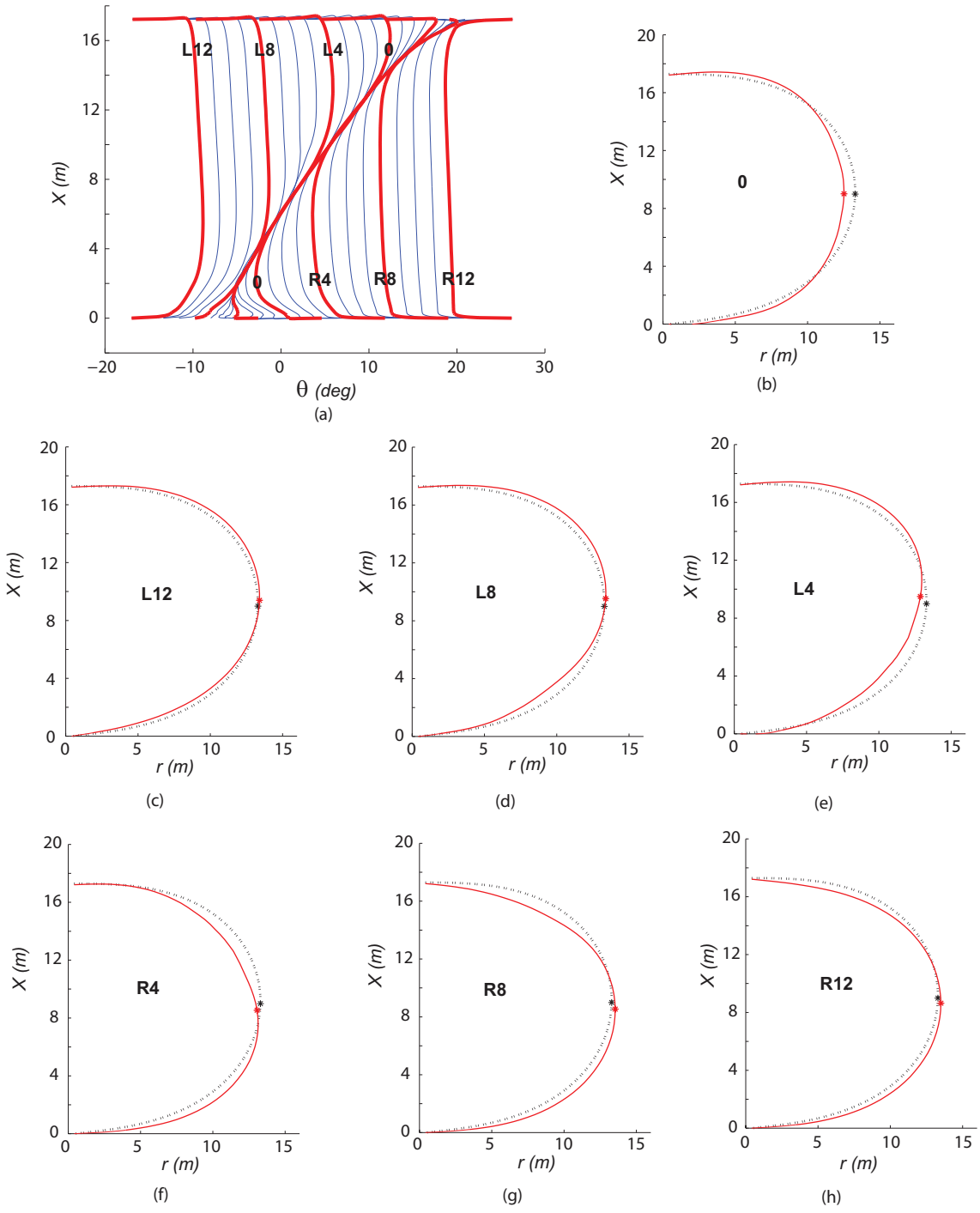

Figure 5.5: Geometry of clefted tendons for Balloon #1: (a) θ vs. X; (b)-(h) r vs. X.

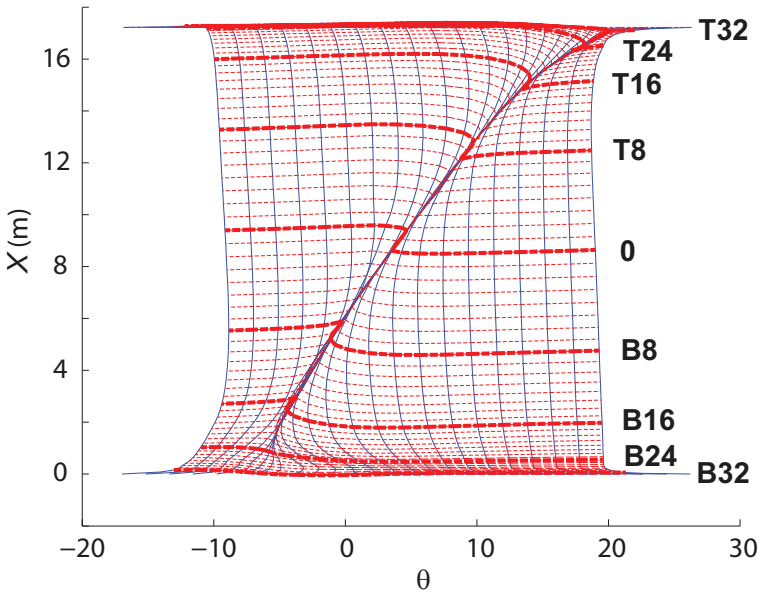

Figure 5.6: 2D geometry of clefted tendons with horizontal grid (θ vs. X relation).

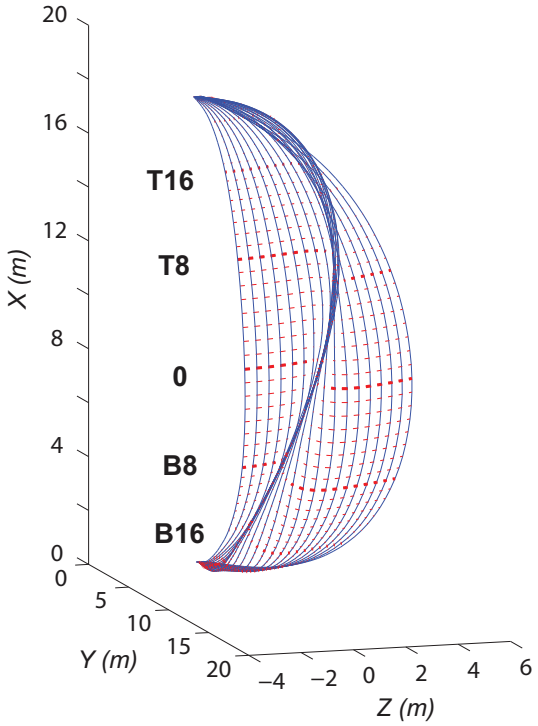

Figure 5.7: 3D geometry of clefted tendons with horizontal grid (Cartesian coordinate).

the tendon force is ≈ 30 N and its value decreases near the cleft and actually drops to ≈ 0 when a tendon joins the cleft.

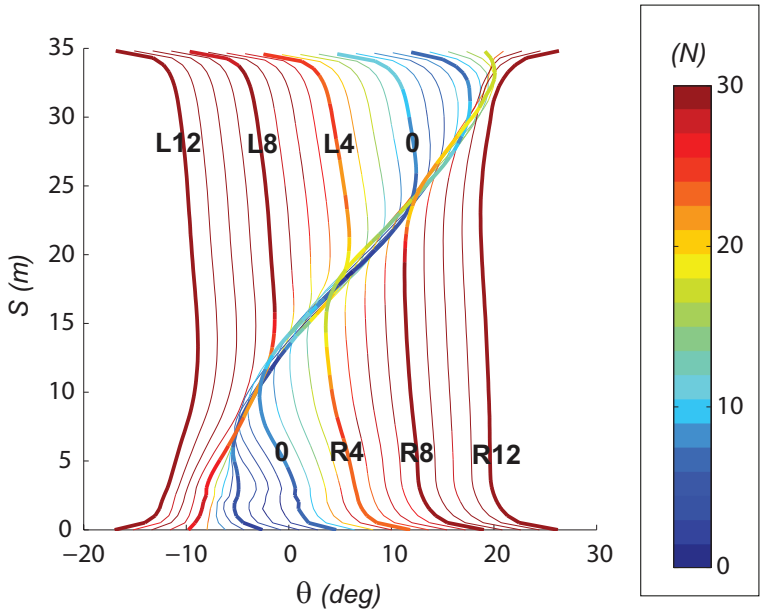

Figure 5.8: 2D stress distribution of clefted tendons.

The film stress distribution at step 1 and step 2 are presented in Figures 5.9 and 5.10 respectively. At step 1, a cleft appears as soon as the stress in the bottom region is relaxed and the bottom end fitting is offset from the X-axis. Along the cleft, the film is tensioned in the meridional direction but unstressed in the hoop direction. Once the cleft has formed, the second step resets the bottom constraint to the apex and reapplies the pressure over the whole region. Compared to the axi-symmetric configuration, the height of the clefted balloon is nearly the same but its volume is slightly increased.

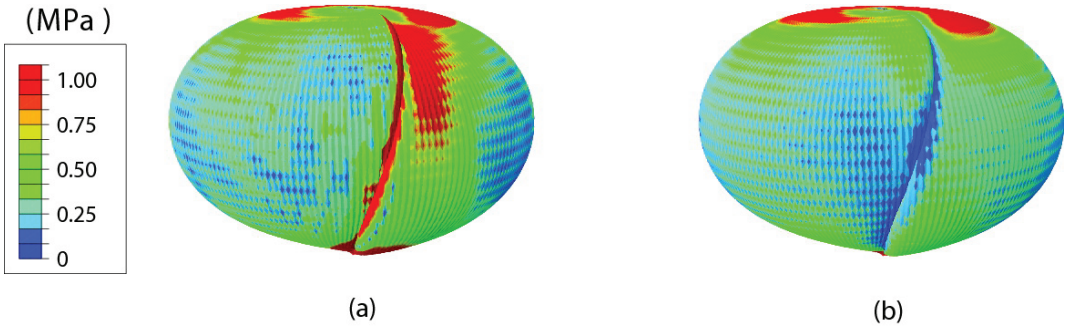

Figure 5.9: Stress distribution at step 1: (a) meridional stress; (b) hoop stress (Units: MPa).

Figures 5.11 and 5.12 show the evolution of the stress distribution from a 200-cyclically symmetric shape to two different S-clefted configurations. Using a different viscosity coefficient, 0.8 instead of 0.4, an

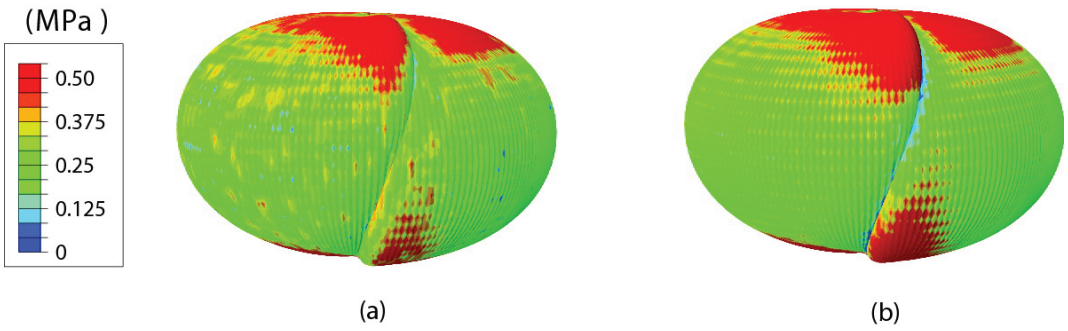

Figure 5.10: Stress distribution at step 2: (a) meridional stress; (b) hoop stress (Units: MPa).

alternative S-cleft tilting to the left is produced by the simulation, which illustrates that the tilting direction of S-cleft is randomly picked. In the intermediate steps, a symmetric cleft with "Y" shape occurs, then either the left branch or the right branch gradually vanish, and finally it forms the S-cleft.

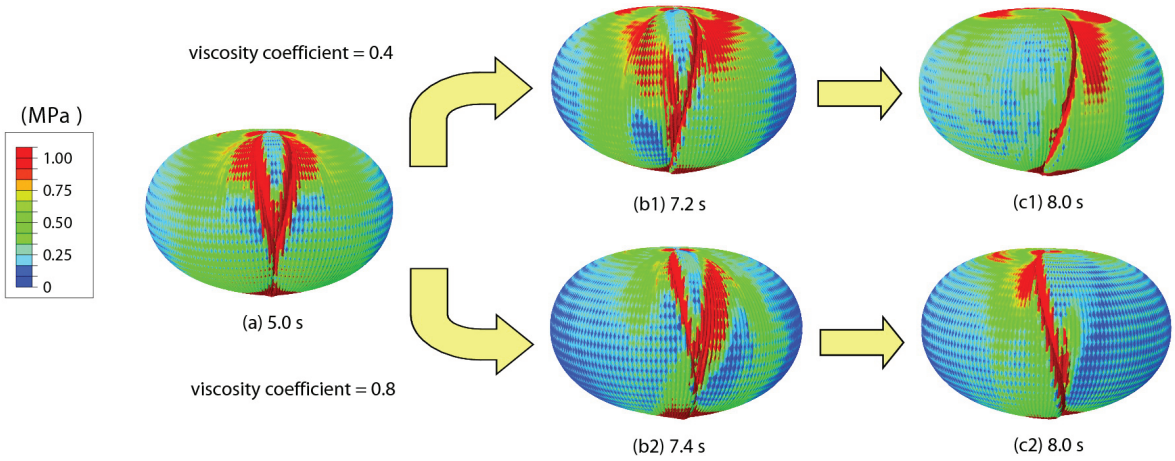

Figure 5.11: Intermediate meridional stress distribution at step 1: (a)-(b1)-(c1) for viscosity coefficient 0.4; (a)-(b2)-(c2) for viscosity coefficient 0.8.

A visual comparison, in Figure 5.13, shows that the simulation result agree remarkably well with the test observation. This it the first time that an S-cleft has been captured computationally.

Of the many factors that may contribute to the formation of S-clefts, it has been conjectured that self-contact within the balloon may play a leading role. We can use our simulation to explore this conjecture and see what happens if the balloon is "magically" allowed to pass through itself. This was investigated by removing the contact option from the simulation.

The results of this modified simulation are presented in Figure 5.14. This new configuration is still clefted but not in the typical S-shape. Instead of forming an S-cleft, the balloon has formed a meridional cleft with the spare film arranged around a kind of inner tube attached to the balloon. Severe overclosure of the gap

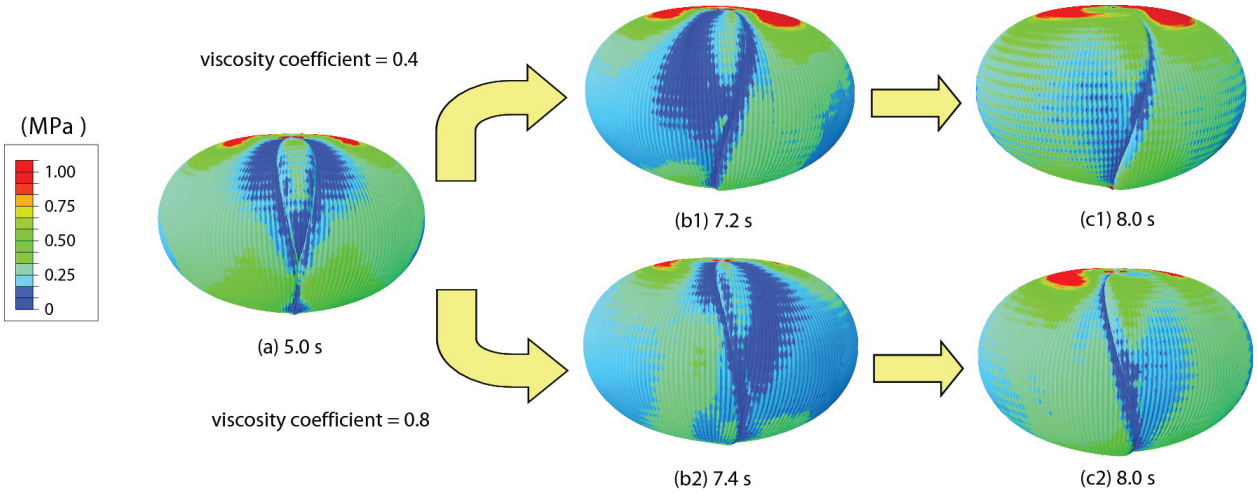

Figure 5.12: Intermediate hoop stress distribution at step 1: (a)-(b1)-(c1) for viscosity coefficient 0.4; (a)-(b2)-(c2) for viscosity coefficient 0.8.

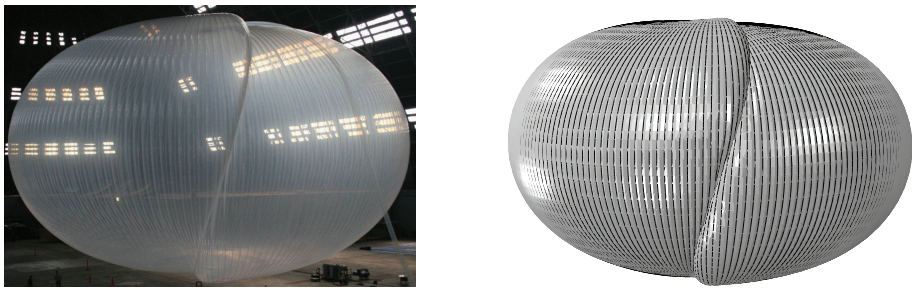

Figure 5.13: Comparison of clefted shapes for balloon # 1 (a) NASA test; (b) simulation.

across the contact surfaces has occurred because the membrane has been allowed to penetrate through itself. Compared to the previous analysis, the strain energy of this balloon model is higher.

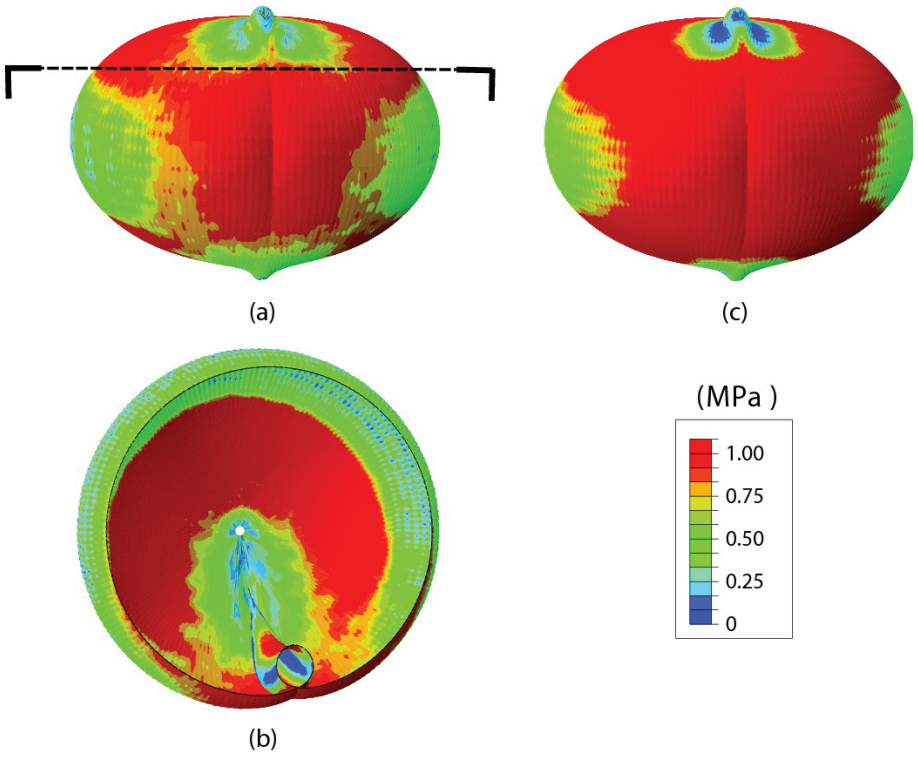

Figure 5.14: Stress distribution of clefted configuration without contact: (a) meridional stress; (b) meridional stress (Cross section); (c) hoop stress (Units: MPa).

The variation of the total potential energy is a useful tool to study the stability of clefted configurations. Ignoring material dissipation and heat transfer, the variation of total potential energy $\Delta\varepsilon$ is given by

$$\Delta\varepsilon = \Delta\varepsilon_P + \Delta\varepsilon_M \tag{5.2}$$

where $\Delta\varepsilon_P$ is the variation of the potential energy of the lifting gas, written as $\Delta\varepsilon_P = -\Delta p \Delta V$. $\Delta\varepsilon_M$ is the variation of the strain energy of film and tendons.

The volume of the balloon, V, is defined as the inner space enclosed by the film and is calculated from

$$V = \sum_{i=1}^{m} (\mathrm{Sign}_i \times V_i) - V_{\mathrm{Oc}} \tag{5.3}$$

Here the summation is the algebraic sum of the volumes of the tetrahedra V_i, where m is the number of triangular elements that model the film. The i-th tetrahedron is constructed as follows: first we pick a fixed random point (x_0, y_0, z_0) within the enclosed region as the top vertex of the tetrahedron, then we choose the i-th triangular element as its base; the Cartesian coordinates of the three nodes are $(x_{i,1}, y_{i,1}, z_{i,1})$,

$(x_{i,2}, y_{i,2}, z_{i,2})$ and $(x_{i,3}, y_{i,3}, z_{i,3})$, see Figure 5.15. Therefore the volume of this tetrahedron is

$$V_i = \frac{1}{6}\begin{bmatrix} x_0 & y_0 & z_0 & 1 \\ x_{i,1} & y_{i,1} & z_{i,1} & 1 \\ x_{i,2} & y_{i,2} & z_{i,2} & 1 \\ x_{i,3} & y_{i,3} & z_{i,3} & 1 \end{bmatrix}, i = 1, 2...m\cdot \tag{5.4}$$

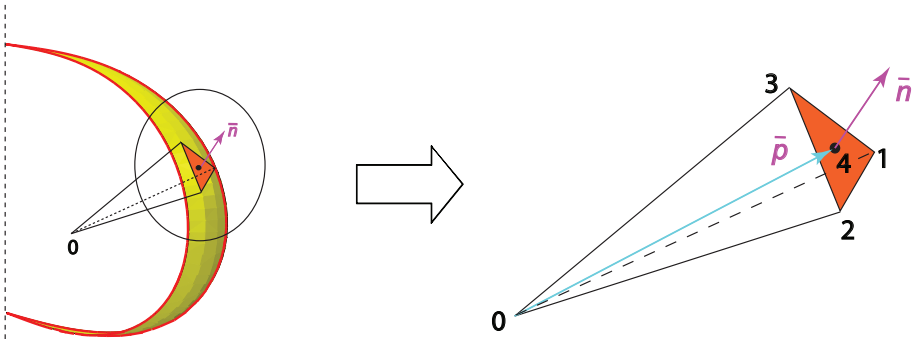

Figure 5.15: Schematic of volume calculation.

In Figure 5.15, $\overline{n}$ defines the normal vector to the surface element, and $\overline{p}$ defines the vector pointing from the top vertex O to the centroid of the base 4. Sign_i, the sign of the tetrahedron, is $+1$ when $\overline{p} \bullet \overline{n} \geq 0$, whereas it is -1 when $\overline{p} \bullet \overline{n} < 0$. Hence, the negative sign applies when the surface is non-convex, e.g., the contact surface is concave. Overclosure occurs in a clefted configuration obtained without including contact model in the simulation. The volume of the overclosure V_{oc} is the volume of the inner tube in the clefted configuration obtained in this case, and is zero for the other two cases.

Table 5.4 compares the variation of the total potential energy with reference to the axi-symmetric configuration. $\Delta\varepsilon_P$, i.e. ΔV, is a more significant contributor to $\Delta\varepsilon$ than $\Delta\varepsilon_M$.

If the variation of the potential energy of the lifting gas $\Delta\varepsilon_P$ is neglected, then the principle of minimum strain energy would indicate that the axi-symmetric configuration is the most stable configuration. The clefted configuration ignoring the kinematic constraints imposed by contact gives the minimum total potential energy but this solution is physically infeasible. The clefted configuration obtained by including the contact model has a total potential energy intermediate between the above two models, and hence it is more stable than the axi-symmetric configuration.

Next, we use the simulation to answer the following question of great practical importance. Does the cleft disappear if we significantly increase the base pressure? We have computed the equilibrium shape for $p_D \rightarrow 100$ Pa while keeping the pressure gradient constant and the results are shown in Figure 5.16. The stress levels are higher but, instead of unfolding the S-cleft has moved inwards and the indentation has becomes even deeper. Recall that the total volume V was 6939 m^3 at Δp_D=10 Pa, and it increases to

Table 5.4: Variation of total potential energy for balloon # 1

	Strain energy ε_M (J)	Variation of strain energy $\Delta\varepsilon_M$ (J)	Volume V (m^3)	Variation of potential energy of lifting gas $\Delta\varepsilon_P$ (J)	Variation of total potential energy $\Delta\varepsilon$ (J)
Axi-symmetric config.	45.84	0	6876	0	0
Clefted config. (with contact)	48.45	2.61	6939	-711.9	-709.3
Clefted config. (without contact)	75.15	29.31	7195	-3604.7	-3575.4

7448 m^3 at Δp_D=100 Pa. Also, the total potential energy ε has decreased, which indicates that this more highly pressurized configuration is even more stable. This result shows the irreversibility of the S-cleft by applying a higher pressure.

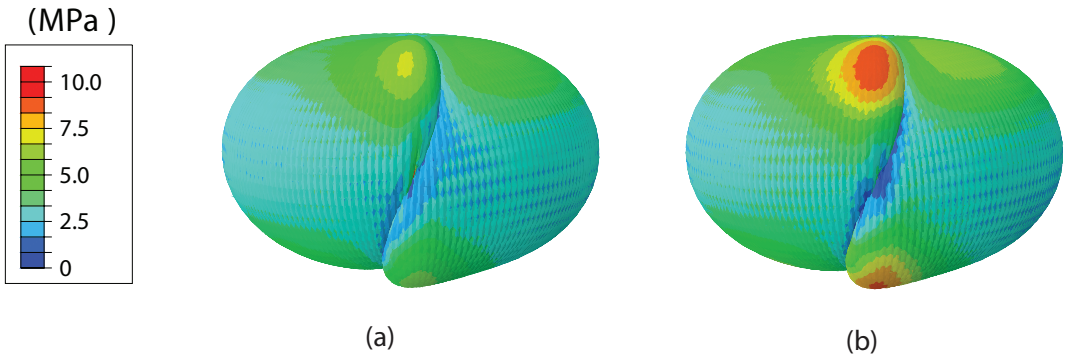

Figure 5.16: Stress distribution at Δp_D=100 Pa: (a) meridional stress; (b) hoop stress (Units: MPa).

5.3 Results for Balloon # 4 with 55° Bulge Angle

The analysis for this balloon followed exactly the same steps described in Section 5.2 and the simulation steps are presented in Table 5.5. Complete deployment of this balloon had been observed during the indoor test. Considering that no clefts existed in the final configuration, a much smaller viscosity coefficient was applied to achieve the greatest possible stability in the simulations. Hence, see Figure 5.17(a), more substeps were required to achieve full convergence at the end of the simulation. The large oscillations in the kinetic energy decreased throughout the substeps of step 2. Figure 5.17(b) and (c) show large variation of stress distribution due to high oscillation of kinetic energy at step 2.

In Figure 5.18, note that after the constraint shift in step 1, the stress distribution becomes quite asymmetric and the balloon takes up a clefted configuration. The shape at the end of step 2 is nearly axi-symmetric with only a small change of stress in a small region near the bottom apex, as shown in Figure 5.19.

Table 5.5: Constraint shift simulation steps for balloon # 4

Step		Loading time (s)	Viscosity coefficient
Step No.	Substep No.		
1	1	10.0	0.8
2	2	5.0	0.8
	3	5.0	0.2
	4	5.0	0.05
	5	5.0	0.02
	6	5.0	0.02
	7	5.0	0.01
	8	5.0	0.01

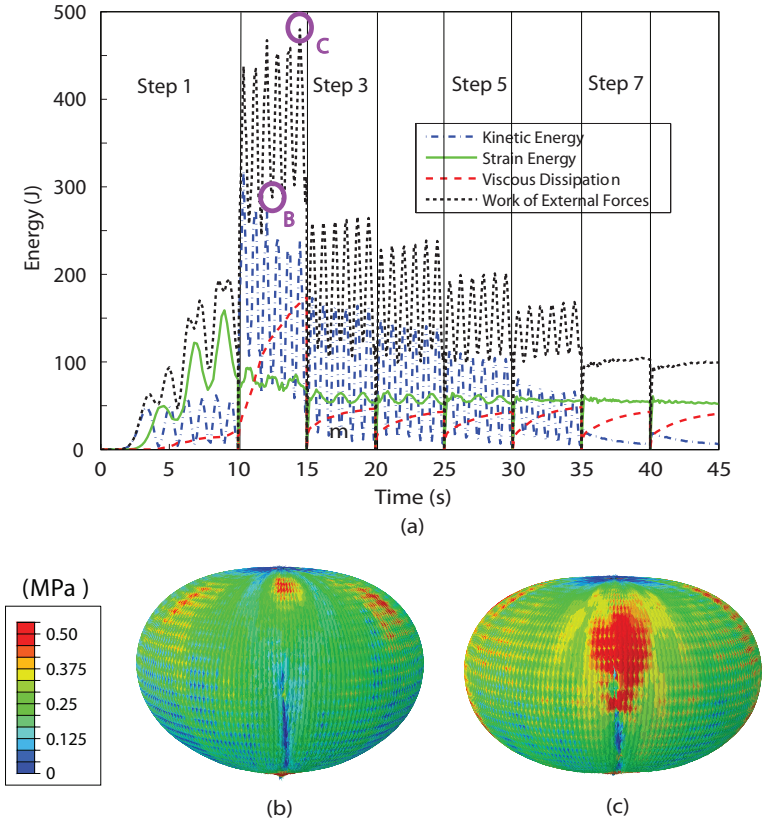

Figure 5.17: (a) Energy variation for balloon # 4; (b)-(c) hoop stress distribution at different time of step 2.

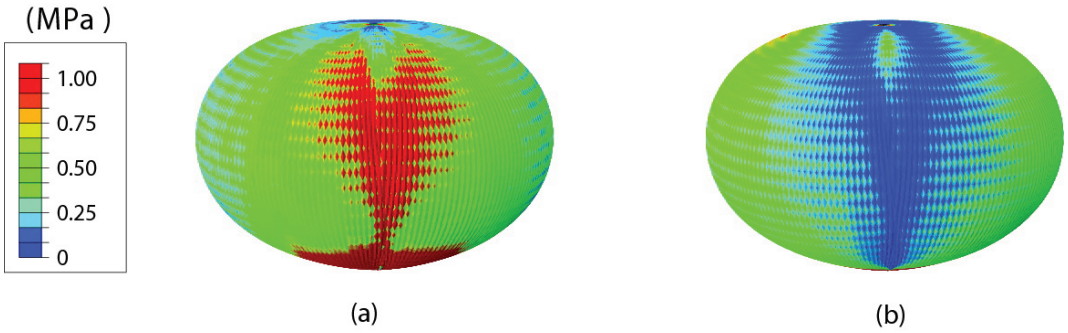

Figure 5.18: Stress distribution of balloon # 4 at step 1: (a) meridional stress; (b) hoop stress (Units: MPa).

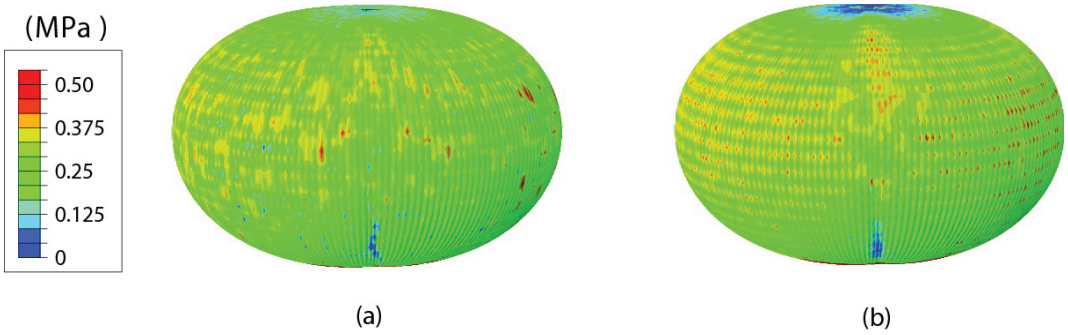

Figure 5.19: Stress distribution of balloon # 4 at step 2: (a) meridional stress; (b) hoop stress (Units: MPa).

Figure 5.20 provides a visual comparison between the simulation result and the test. They generally agree well: no cleft was observed in the experiment, whereas the simulation shows a deployed shape with only a tiny residual distortion.

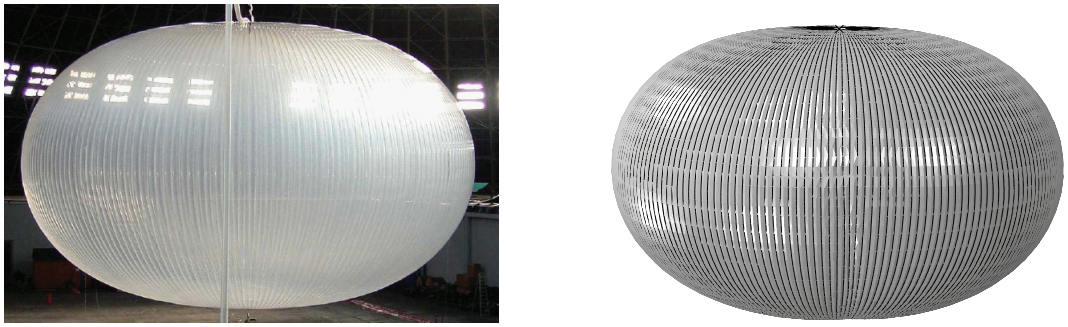

(a) (b)

Figure 5.20: Shape comparisons for balloon # 4.

Again we removed the general contact from the original model and obtained the stress distribution shown in Figure 5.21. Compared to the corresponding results for the original model, we have complete deployment in both cases, but the model without contact shows a bit more residual distortion. Table 5.6 confirms the similarity of their shapes by the very close values of the enclosed volumes. The small variation of total potential energy between the results for the two models, also shown in Table 5.6, proves that the 55 degree bulge angle balloon will achieve an axi-symmetric configuration after pressurization.

Table 5.6: Variation of total potential energy of balloon # 4

	Strain energy ε_M (J)	Variation of strain energy $\Delta\varepsilon_M$ (J)	Volume V (m^3)	Variation of potential energy of lifting gas $\Delta\varepsilon_P$ (J)	Variation of total potential energy $\Delta\varepsilon$ (J)
Axi-symmetric config.	50.78	0	7239.7	0	0
Unclefted config. (with contact)	52.18	1.4	7240.3	-6.78	-5.38
Unclefted config. (without contact)	52.71	1.93	7246.3	-74.58	-72.65

5.4 Results for Balloon# 5 with 90^o Bulge Angle

In this section we investigate a third balloon that, although very close in design to Balloon #1, was actually sufficiently different that when it was tested it took up an axi-symmetric configuration after full pressurization. Therefore this balloon provides a stringent test for our clefting test. We follow the same loading

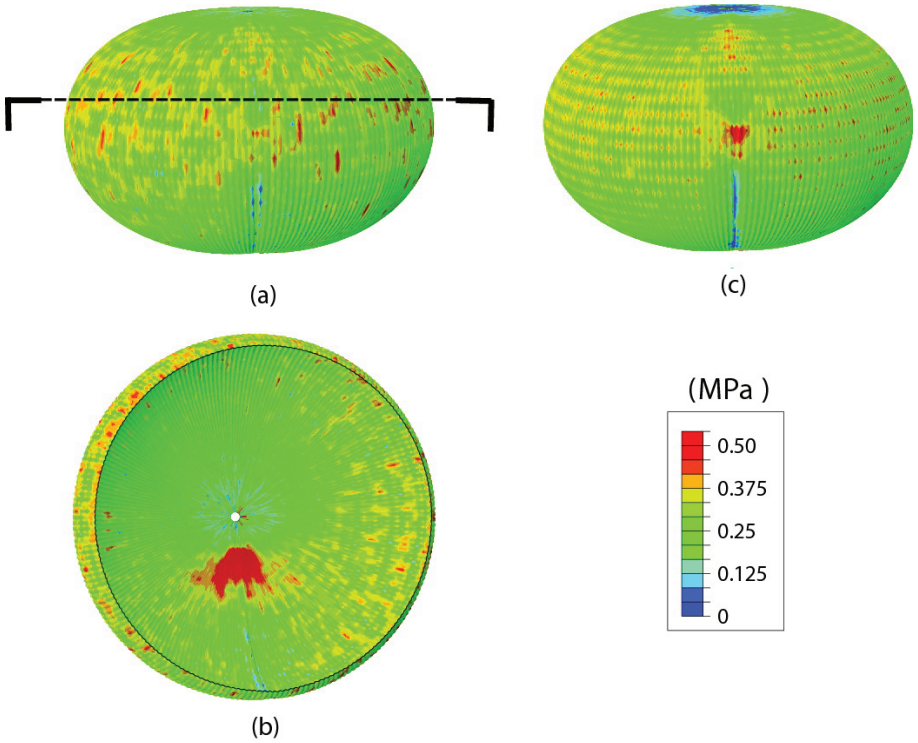

Figure 5.21: Stress distribution of balloon # 4 without contact: (a) meridional stress; (b) meridional stress (cross section); (c) hoop stress (Units: MPa).

Table 5.7: Constraint shift simulation steps for balloon # 5

Step		Loading time (s)	Viscosity coefficient
Step No.	Substep No.		
1	1	10.0	0.8
2	2	5.0	0.8
	3	5.0	0.4
	4	5.0	0.2
	5	5.0	0.1
	6	5.0	0.05
	7	5.0	0.02
	8	5.0	0.01

procedures as before and the two-step simulation are presented in Table 5.7. The energy variation is shown in Figure 5.22.

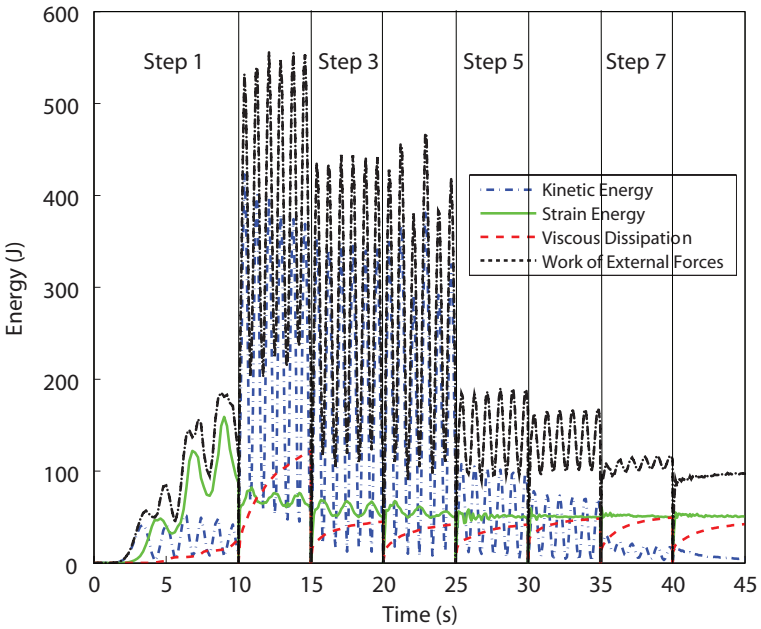

Figure 5.22: Energy variation of balloon # 5.

The symmetric stress distribution is broken in step 1, Figure 5.23, and its symmetry is finally recovered in Figure 5.24 at the end of step 2 except for a small distortion near the bottom apex.

In Figure 5.25 the simulation result is visually compared with the test observation. The results are consistent in predicting the completely deployed shape except for a small residual distortion shown in the simulation picture.

Repeating the analysis after removing the general contact definition from the model leads to the clefted configuration in Figure 5.26: overclosure can be seen in the cross section of the balloon, in contrast to the full deployment of the original model. Comparison of the variation of total potential energy, Table 5.8, reveals that contact plays a key role in producing the cleft: on the one hand, addition of general contact will increase

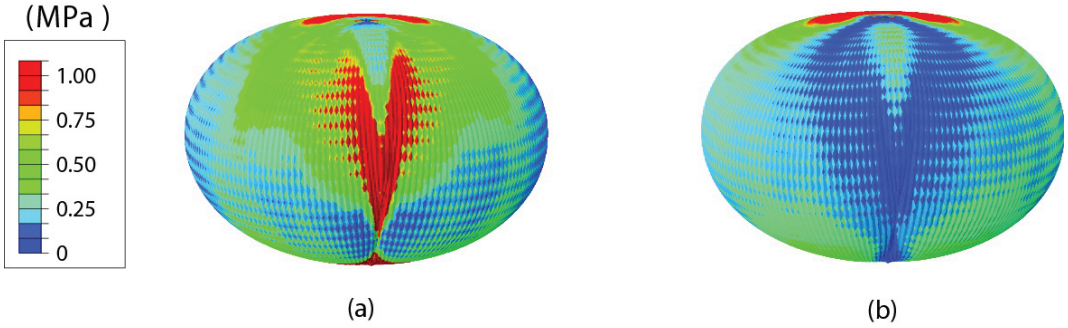

Figure 5.23: Stress distribution of balloon # 5 at step 1: (a) meridional stress; (b) hoop stress (Units: MPa).

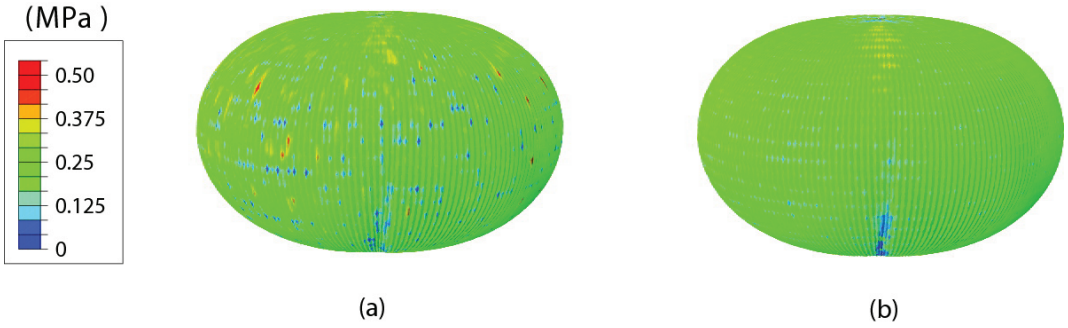

Figure 5.24: Stress distribution of balloon # 5 at step 2: (a) meridional stress; (b) hoop stress (Units: MPa).

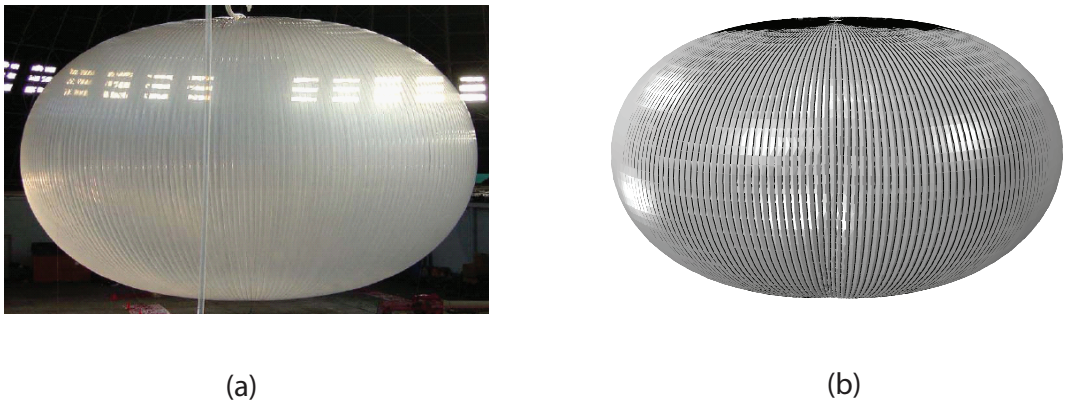

Figure 5.25: Shape comparison for balloon # 5.

the total potential energy; on the other hand, it helps to prevent clefting.

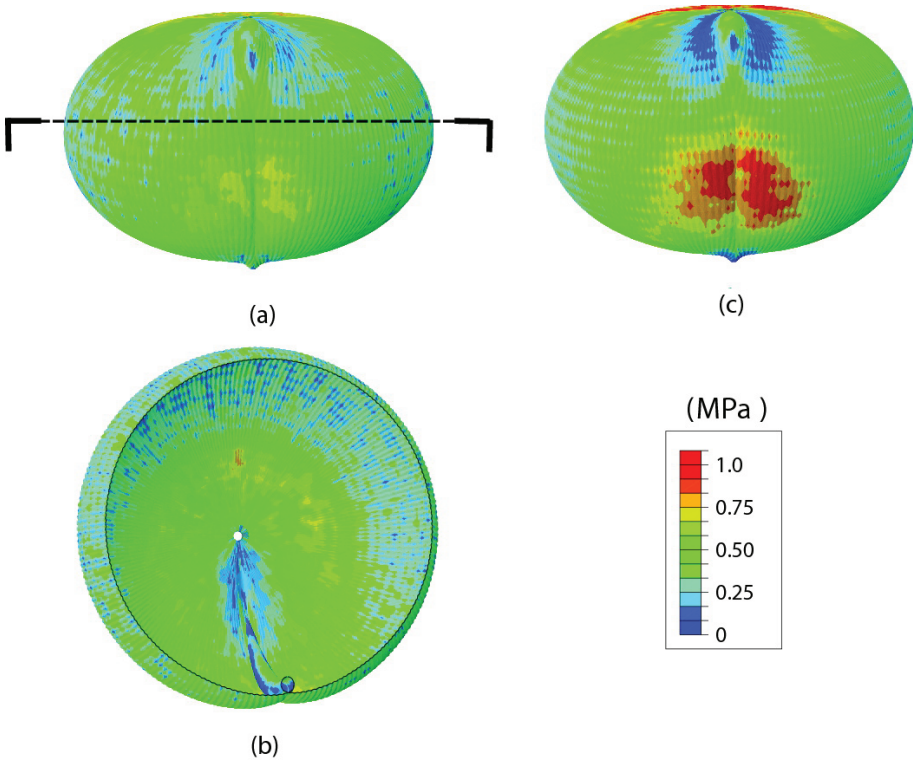

Figure 5.26: Stress distribution of balloon # 5 without contact: (a) meridional stress; (b) meridional stress (cross section); (c) hoop stress (Units: MPa).

Table 5.8: Variation of total potential energy for balloon # 5

	Strain energy ε_M (J)	Variation of strain energy $\Delta\varepsilon_M$ (J)	Volume V (m^3)	Variation of potential energy of the lifting gas $\Delta\varepsilon_P$ (J)	Variation of total potential energy $\Delta\varepsilon$ (J)
Axi-symmetric config.	48.33	0	7138	0	0
Unclefted config. (with contact)	50.28	1.95	7145	-79.81	-77.1
Clefted config. (without contact)	54.29	5.96	7278	-1582	-1576

Chapter 6

Dimensional analysis of clefting in constant-stress balloons

In the last chapter, we have developed an efficient numerical technique, the constraint shift method, to predict S-clefts; however for each clefting test simulation, it still takes one or two weeks to run on a 64-bit system with 12-core CPU. This chapter formulates through dimensional analysis a new cleft factor, CF_6, as an indicator of the tendency to S-cleft for a family of superpressure balloons based on constant-stress design. First, a complete list of design parameters for constant-stress (CS) balloons is made and categorized. With the introduction of some fundamental assumptions, 9 representative independent variables are chosen. It is assumed that CF_6 can be expressed by a power law relationship in terms of 6 dimensionless groups. Finally an example illustrates how to calculate the power coefficients of the analytical formula and analyze the sensitivity of clefting to changes in design parameters.

6.1 List of design parameters

6.1.1 Categories of parameters

This section derives a complete list of design parameters for constant-stress (CS) balloons. The parameters can be categorized into the following four groups (1) planetary environmental data; (2) material properties; (3) geometry and (4) clefting test parameters.

6.1.1.1 Planetary environmental data

The temperature-altitude relationship for the Earth's atmosphere has the expected, colder as you go up trend in the troposphere, but in the stratosphere there is a reversal of this trend. This reversal is a direct result of a concentration of ozone at 20 km altitude absorbing solar ultraviolet energy. The tropopause, i.e. the demarcation between troposphere and stratosphere, varies in altitude with season and location, the coldest occurring in the Australian desert in summer. BalloonAscent, a balloon flight simulation tool developed by Farley [17], can use up to 12 points to define the atmospheric temperature, and to determine pressure

Table 6.1: Planetary environmental data

No.	Parameter	Fundamental dimensions	Included in final list of independent variables
1	Design temperature ΔT_d	θ	N
2	Design pressure p_d	FL^{-2}	N
3	Design specific buoyancy b_d	FL^{-3}	N

Table 6.2: Material properties

No.	Parameter	Fundamental dimensions	Included in final list of independent variables
	Design hoop stress $\sigma_{d,h}$ Film thickness t_f		
1	$\sigma_{d,h} t_f$	FL^{-1}	N
	Hoop film modulus E_h Meridional film modulus E_m } Average film modulus E_f Film thickness t_f		
2	$E_f t_f$	FL^{-1}	Y
	Hoop Poisson's ratio ν_h Meridional Poisson's ratio ν_m } Average Poisson's ratio ν_f		
3	ν_f	1	N
4	Tendons stiffness EA	F	N
	Density of tendons ρ_t Gravity g Tendon area A		
5	$\gamma_t = \rho_t g A$	FL^{-1}	N
	Density of film ρ_f Gravity g Film thickness t_f		
6	$\gamma_f = \rho_f g t_f$	FL^{-2}	Y
	Hoop CTE of film $\kappa_{f,h}$ Meridional CTE of film $\kappa_{f,m}$ } Average CTE of film κ_f		
7	κ_f	θ^{-1}	Y
8	CTE of tendons κ_t	θ^{-1}	N

and density as a function of altitude. It is assumed that for a given mission, with given season and launch location, the design temperature ΔT_d, design pressure p_d, and design specific buoyancy b_d are fixed. These variables are listed in Table 6.1.

6.1.1.2 Material properties

The material parameters of the balloon film and tendons are listed in Table 6.2. Because the balloon film, made of LLDPE, shows only weak anisotropy, for simplicity it is reasonable to average its moduli and Poisson's ratios in the longitudinal and transverse directions and assume in-plane isotropic behavior.

Table 6.3: Geometry

No.	Parameter	Fundamental dimensions	Included in final list of independent variables
1	Unstressed gore length L_g	L	Y
2	Unstressed gore width w_g	L	Y
3	Number of lobes N	1	Y
4	Cap length L_{cap}	L	N
5	Radius of apex and nadir end fitting r_{ape}	L	N

Table 6.4: Clefting test parameters

No.	Parameter	Fundamental dimensions	Included in final list of independent variables
1	Cleft temperature ΔT_c	θ	Y
2	Cleft pressure p_c	FL^{-2}	Y
3	Cleft specific buoyancy b_c	FL^{-3}	Y

6.1.1.3 Geometry

Table 6.3 lists the geometric parameters of a superpressure balloon. A cap region normally covers 37% of the upper part of the hull and in this region the film thickness doubles to reduce the stress when the balloon is only partially inflated. Therefore once the gore length L_g is fixed, the cap length L_{cap} is assumed to be fixed. The radius of the end fittings is also assumed to be fixed. Compared to the total gore length, the radius of the end fittings is small and the effects of changing the end fitting radius on the overall behavior of the balloon can be neglected.

6.1.1.4 Clefting test parameters

The design scenario for constant-stress (CS) superpressure balloons is illustrated in Figure 6.1. Note that for a given design hoop stress, the cutting pattern of an optimized balloon with constant hoop stress is generated by BalloonAscent. After the first stage, axisymmetric analysis, we continue by running the clefting test with the input parameters listed in Table 6.4.

6.2 Determination of dimensionless groups

6.2.1 Smalley and Farley dimensionless parameters

Figure 6.2 shows the force balance of a balloon structure at equilibrium, and the relevant dimensional parameters are defined in Table 6.5. Additional lift beyond what it takes to lift the gross weight, the so-called free lift, is balanced by the aerodynamic drag. The free lift ratio, defined as $GI/G = 1 + F/G$, is in the 10% range (=1.1) for normal day launch, while free lift ratio is in the 25% range (=1.25) for night launch. The relations between the dimensional parameters in Table 6.5 are given by

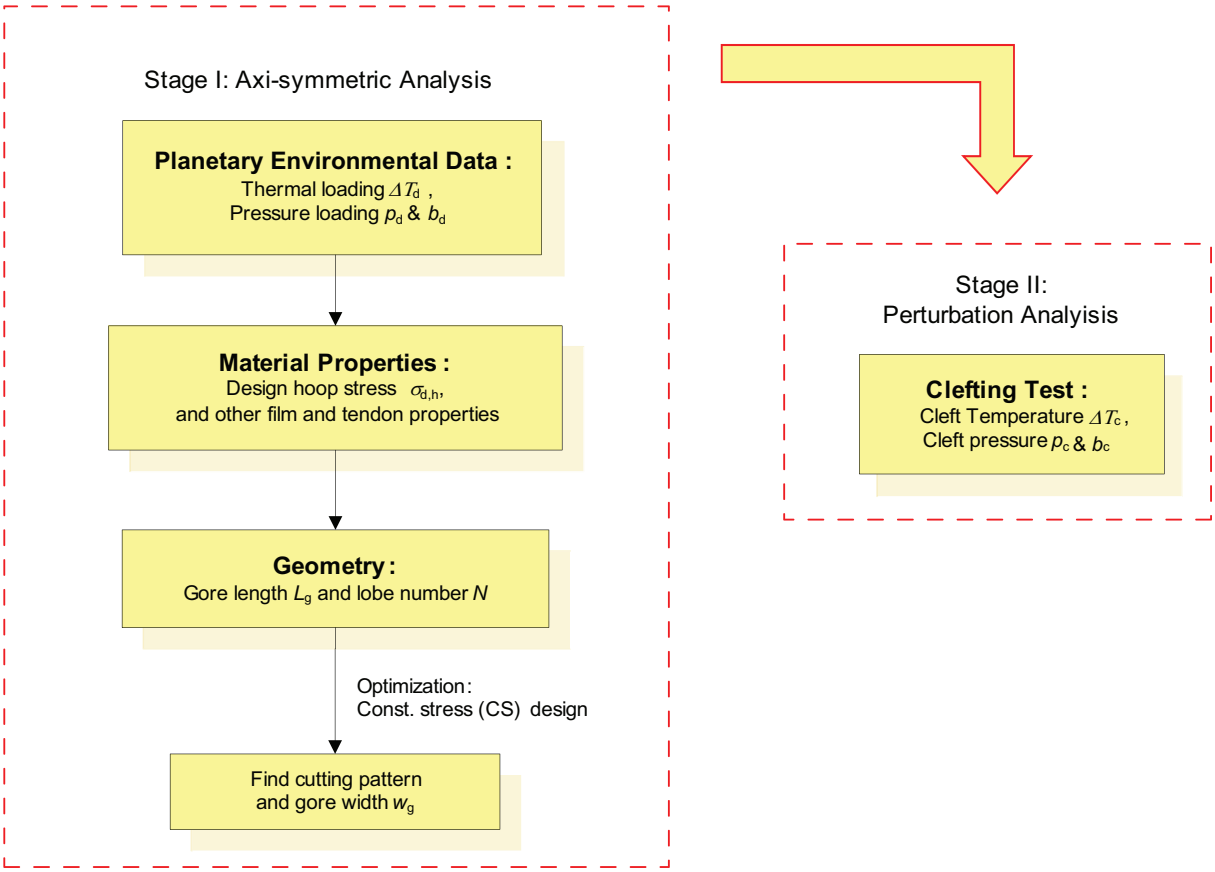

Figure 6.1: Flowchart of design scenario for constant-stress (CS) superpressure balloons.

Table 6.5: Dimensional parameters for balloon force balance

No.	Parameter	Fundamental dimensions
1	Volume V	L^3
2	Specific buoyancy $b = \Delta\rho g$	FL^{-3}
3	Gross inflation GI	F
4	Free lift F	F
5	Gross weight $G = GI - F$	F
6	Suspended load L	F
7	Balloon material weight (not including lift gas) W	F

$$GI = G + F = W + L + F = bV \tag{6.1}$$

$$G = W + L \tag{6.2}$$

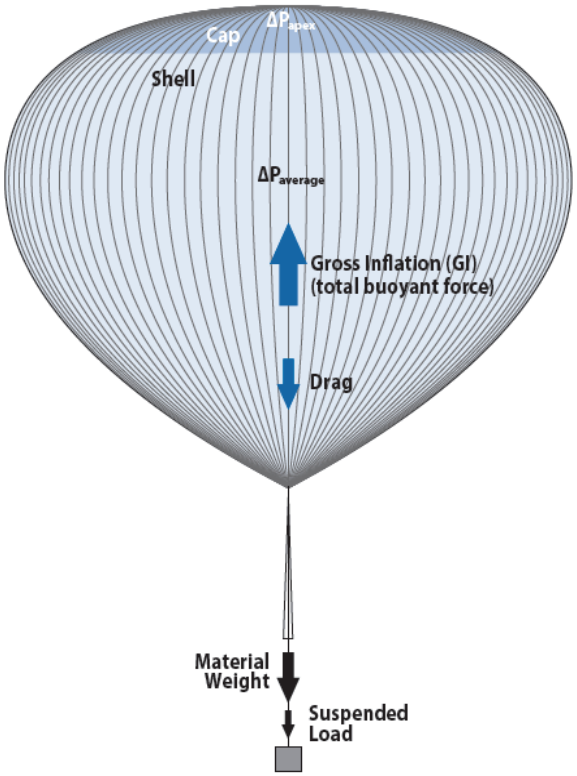

Figure 6.2: Balloon force balance (Courtesy of Rodger Farley).

In the 1950s and 1960s, balloon researchers [3, 49] considered the family of natural shape balloons, expressed in a non-dimensional form that removes the scale effects so that each family can be designated by ratios of forces and geometrical parameters. Different balloons with the same ratios have similar shapes

regardless of the actual size. Smalley [49] defined the "natural length" $\lambda_S = (L/b)^{1/3}$, which has dimensions of length and the dimensionless parameter, skin areal weight $\Sigma_S = (2\pi)^{1/3}(\frac{\gamma_f}{b\lambda_S})$. Farley [17] used the gross inflation GI to nondimensionalize the forces. The Farley "natural length" is defined as $\lambda_F = (GI/b)^{1/3} = V^{1/3}$, and therefore the Farley skin areal weight becomes $\Sigma_F = (2\pi)^{1/3}(\frac{\gamma_f}{b\lambda_F})$. The suspended load is nondimensionalized as $L_{bar} = L/GI$. Smalley's and Farley's parameters are related by the following relations

$$\lambda_S = \lambda_F L_{bar}^{1/3} \tag{6.3}$$

$$\Sigma_S = \Sigma_F / L_{bar}^{1/3} \tag{6.4}$$

Farley then considered a nondimensional parameter to predict S-clefting of superpressure balloons at any scale. By observing that clefts are a result of excessive circumferential material creating wrinkles, he assumed that meridional line loading was pro-cleft and circumferential line loading was anti-cleft, and thus concluded that the ratio of circumferential to meridional line loading determines the clefting behavior. To deal with a non-smooth lobed membrane structures, Farley considered that a virtual smooth-shape balloon that shared the geometry of the actual balloon only at the tendon attachments, as shown in Figure 6.3(a).

For the case of a n-lobed balloon, the angle subtended by a lobe is $\theta = 2\pi/n$, the bulged angle at the equator is α, r is the radius of the circular arc, and the equatorial radius of the balloon is denoted by R. Given the internal pressure Δp, the circumferential line loading N is

$$\Delta p = \frac{N}{r} \tag{6.5}$$

The component of N in the global circumferential direction of the virtual smooth surface, t_c, is

$$t_c = N \cos\left(\frac{\alpha - \theta}{2}\right) = \Delta p r \cos\left(\frac{\alpha - \theta}{2}\right) \tag{6.6}$$

The balloon radius R and the lobe bulge radius r are related by

$$r = R \frac{\sin\frac{\theta}{2}}{\sin\frac{\alpha}{2}} \tag{6.7}$$

Substituting Equation 6.7 into Equation 6.6 yields

$$t_c = \Delta p R \frac{\sin\frac{\theta}{2}}{\sin\frac{\alpha}{2}} \cos\left(\frac{\alpha - \theta}{2}\right) \tag{6.8}$$

The meridional line loading t_m was calculated by considering an equatorial cross section of the virtual smooth surface, as shown in Figure 6.3(b)

$$t_m = \Delta p R / 2 \tag{6.9}$$

Therefore the Farley cleft factor (CF), defined as 500 times the ratio of circumferential line loading to meridional line loading (t_c/t_m) in the virtual smooth surface, can be written as

$$CF = 500\,(t_c/t_m) = 1000\frac{\sin\frac{\theta}{2}}{\sin\frac{\alpha}{2}}\cos\left(\frac{\alpha-\theta}{2}\right) = 1000\frac{\sin\frac{\pi}{N}}{\sin\frac{\alpha}{2}}\cos\left(\frac{\theta}{2}-\frac{\pi}{N}\right) \tag{6.10}$$

Farley compared the values of CF for balloons with different designs and reached the conclusion that balloons should deploy when $CF \geq CF_{cr} = 16$. However he also found that the cleft factor CF based only on geometry didn't give the full story, and thus he defined a new cleft factor, CF_5, by modifying the original CF in Equation 6.10 by dividing CF by the Farley skin areal weight Σ_F

$$CF_5 = CF/\Sigma_F \tag{6.11}$$

Farley discovered that for safe design, $CF_5 > CF_{5,cr} = 120$.

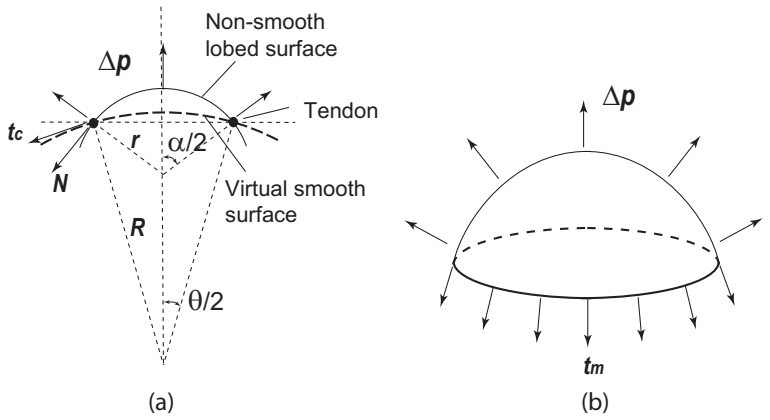

Figure 6.3: Schematic of derivation of Farley cleft factor: (a) circumferential line loading; (b) meridional line loading in a smooth surface.

6.2.2 Chosen independent variables

In Section 6.1, a long list was made of independent parameters that describe constant-stress (CS) design of superpressure balloons. To simplify our study, we introduce the following assumptions: (1) for a given mission, ΔT_d, p_d and b_d are fixed; (2) we can neglect the variation in the parameters ν_f, EA, γ_t, κ_t, L_{cap} and r_{ape} because according to NASA balloon designers these effects on clefting are negligible; (3) $\sigma_{d,h}$ and α are related hence only one of the two is independent. With these simplifications, the 9 chosen independent variables are listed in Table 6.6.

Table 6.6: Chosen independent variables

No.	Parameter	Fundamental dimensions
1	Unstressed gore length L_g	L
2	Unstressed gore width w_g	L
3	Number of lobes N	1
4	CTE of film κ_f	θ^{-1}
5	Cleft temperature ΔT_c	θ
6	Cleft pressure p_c	FL^{-2}
7	Cleft specific buoyancy b_c	FL^{-3}
8	$E_f t_f$	FL^{-1}
9	$\gamma_f = \rho_f g t_f$	FL^{-2}

6.2.3 Formulation of dimensionless groups

Fundamental relationships among dimensional parameters should be dimensionally consistent and unit-free. The central idea of dimensional analysis, also called *Vaschy-Buckingham Pi theorem*, is to express these relationship in terms of dimensionless groups. For a general relationship expressed in terms of dimensional variables, by appropriate changes of units we can establish a corresponding relationship in terms of dimensionless groups [36, 11]. For n independent variables and p fundamental dimensions, the number of independent dimensionless groups is $n - p$. Since the number of chosen independent variables n is 9, the number of fundamental dimensions is p=3 (F, L, θ), and therefore the number of dimensionless groups is 6. After arranging the variables, we define a clefting factor that can be written in terms of 6 dimensionless groups as

$$CF_6 = F\left(\frac{w_g}{L_g}, N, \frac{p_c L_g}{E_f t_f}, \frac{p_c}{\gamma_f}, \frac{\gamma_f}{b_c L_g}, \kappa_f \Delta T_c\right) \tag{6.12}$$

These six dimensionless groups are labeled from 1 to 6. Farley's dimensionless groups, CF and CF_5, overlap with our dimensionless group No. 1 and No. 2, while Farley's skin areal weight Σ_F is similar to dimensionless group No. 5. More dimensionless groups have been taken into account in our formula in view of thermal effects not reflected in Farley's cleft factor. Furthermore we assume a power law relation between the cleft factor and each dimensionless group, and thus the cleft factor expression can be simplified to

$$CF_6 = k\left(\frac{w_g}{L_g}\right)^{\alpha_1} N^{\alpha_2} \left(\frac{p_c L_g}{E_f t_f}\right)^{\alpha_3} \left(\frac{p_c}{\gamma_f}\right)^{\alpha_4} \left(\frac{\gamma_f}{b_c L_g}\right)^{\alpha_5} (-\kappa_f \Delta T_c)^{\alpha_6} \tag{6.13}$$

where k is a dimensionless constant.

Recalling that the balloon film is manufactured at room temperature and superpressure balloons deploy in a colder atmosphere, the cleft temperature ΔT_c is always negative as a result of cooling. For the purpose of power law fitting, a minus sign has been introduced in the sixth dimensionless group to make it positive. In reality, when the cleft temperature ΔT_c changes, the film modulus E_f calculated from the temperature-dependent pseudoelastic model also changes, so both dimensionless group No. 3 and No. 6 should be updated

coherently.

To define a cleft factor with a clear physical meaning, we expect CF_6 to be a continuous function that denotes the clefting properties of a balloon design. Hence a good choice for CF_6 is the volume increase in the configuration obtained after the clefting test divided by the corresponding cyclically configuration subject to the same loading and temperature conditions, i.e.,

$$CF_6 = (V_{cf}/V_{sym} - 1) \times 100 \tag{6.14}$$

A balloon is unclefted when $CF_6 = 0$, while it is highly clefted when the increased volume percentage is larger than certain value, that will be set to 0.8 in Section 6.3.2.

6.3 Example of dimensional analysis

A full scale NASA superpressure balloon with 114.7 m in diameter will be investigated. It has a total volume of 18.79 MCF (million cubic feet), maximum bulge angle 35.7 deg and consists of 280 lobes. The clefting test has shown that the base design of this balloon is expected to deploy into an axi-symmetric configuration, and we can use dimensional analysis to study the sensitivity of this design to clefting. The power coefficients α_i can be calculated when we vary only the i-th dimensionless group while keeping all the others fixed. For example, to calculate α_1, the only variable dimensionless group is w_g/L_g, and then the cleft factor can be written as

$$\log(CF_6) = \alpha_1 \log\left(\frac{w_g}{L_g}\right) + C \tag{6.15}$$

where the intercept C is a constant. For each variation of the i-th dimensionless group, at least two cases of clefting tests are required so that we have no less than three points (including one from the base design) to fit the slope of the straight line defined by Equation 6.15 to obtain the power coefficient α_i.

6.3.1 Implementation of dimensional analysis

Changes to the six dimensionless groups in Equation 6.13 can be made one at a time, as follows:

1. Dimensionless group 1 w_g/L_g: Change w_g and but keep L_g fixed;
2. Dimensionless group 2 N: Change N but keep w_g & L_g fixed;
3. Dimensionless group 3 $(p_c L_g)/(E_f t_f)$: Change E_f but keep w_g & L_g fixed;
4. Dimensionless group 4 p_c/γ_f: Change p_c and then E_f proportionally, but keep w_g & L_g fixed;
5. Dimensionless group 5 $\gamma_f/(b_c L_g)$: Change b_c and use the same design as base design;

6. Dimensionless group 6 $-\kappa_f \Delta T_c$: Change ΔT_c and use the same design as base design.

Note that when we vary the dimensionless group No. 1, the value of the unstressed gore width w_g can be increased but not be decreased as the base design has nearly flat lobes. Similarly, when we vary the dimensionless group No. 2, the number of lobes N can be increased by adding extra lobes and thus increase the total circumferential length, but cannot be decreased because the base design has nearly flat lobes; To vary the dimensionless group No. 3, the film modulus E_f is only increased by considering that at cold temperatures, E_f is generally greater than 230 MPa; To vary the dimensionless group No. 4, the cleft pressure p_c and the film modulus E_f are either increased or decreased; To vary dimensionless group No. 5, the cleft specific buoyancy b_c is either increased or decreased; Finally to vary dimensionless group No. 6, the cleft temperature ΔT_c is only increased because -72 deg for the base design is already the coldest temperature under extreme conditions.

The balloon flight simulation software, BalloonAscent [17], has been used to design optimized constant-stress flat cutting patterns for each of the cases listed above. The design parameters used as inputs for BalloonAscent and the resulting independent variables are shown in Table 6.7 and Table 6.8 respectively. In Table 6.7, the suspended load L is a control parameter for the gore length L_g, and the design hoop stress $\sigma_{d,h}$ controls the gore width w_g. Generally, a higher suspended load requires longer gore length and thus a larger size balloon. Also a higher design hoop stress allows a flatter cutting pattern with a smaller bulge angle, and thus a smaller gore width and less excess of material in the hoop direction. Note that for cases 5a, 5b, 6a and 6b, the same cutting patterns as the base design have been used.

Table 6.9 shows the results of 12 clefting tests carried out according to the procedure in Chapter 5. Seven of these tests were carried out by the present cluster on a Xeon 5680 workstation with 12 cores and took average 12 days of CPU time for each case. The remaining six tests were carried out by Adam Brown at Tensys, UK. The values of the dimensionless groups and the values of Farley modified cleft factor CF_5 are also presented. For case 6a and case 6b, the effects of temperature variation are ignored by CF_5, so CF_5 predicts the same results as for the base design.

6.3.2 Results of dimensional analysis

Table 6.10 shows the cleft factor CF_6 calculated for each case, using Equation 6.14. From all the results above, the minimum CF_6 for a clefted configuration is 0.978 and the maximum CF_6 for an unclefted configuration is 0.522. Therefore we use the average of the two values to design cleft factor of $CF_{6,cr} = 0.8$.

The fitting of the power coefficient for each variation of a dimensionless group is illustrated in Figure 6.4. Once each value of α_i had been obtained, see the values listed in Table 6.10, we substituted these values into Equation 6.13, and calculated k by substituting the remaining values for the base design. Substituting the results into Equation 6.13 we obtain

Table 6.7: Design parameters for dimensional analysis

	Control parameters						Design parameters (dependent)	
	L (kg)	$\sigma_{d,h}$ (MPa)	E_f (Pa)	t_f (m)	ρ_f (kg/m^3)	g (N/kg)	Envelope Volume V (m^3)	Bulge angle α (deg)
Base design	2273	9	2.3×10^8	3.81×10^{-5}	920	9.807	532032	35.7
Variation of dimensionless group 1								
Case 1a	2182	3.3	2.3×10^8	3.81×10^{-5}	920	9.807	536363	117.7
Case 1b	2225	4	2.3×10^8	3.81×10^{-5}	920	9.807	534961	89.7
Variation of dimensionless group 2								
Case 2a	2192.5	4.4	2.3×10^8	3.81×10^{-5}	920	9.807	533235	73.5
Case 2b	2062.3	2.93	2.3×10^8	3.81×10^{-5}	920	9.807	533496	110.4
Variation of dimensionless group 3								
Case 3a	2267	12	9.2×10^8	3.81×10^{-5}	920	9.807	529881	22.6
Case 3b	2262	12.5	1.6×10^9	3.81×10^{-5}	920	9.807	528867	19.4
Variation of dimensionless group 4								
Case 4a	2267	10.5	4.6×10^8	3.81×10^{-5}	920	9.807	531151	35.7
Case 4b	2270.4	7.2	1.1×10^8	3.81×10^{-5}	920	9.807	532075	46.5
Variation of dimensionless group 5								
Case 5a	2273	9	2.3×10^8	3.81×10^{-5}	920	9.807	532032	35.7
Case 5b	2273	9	2.3×10^8	3.81×10^{-5}	920	9.807	532032	35.7
Variation of dimensionless group 6								
Case 6a	2273	9	2.3×10^8	3.81×10^{-5}	920	9.807	532032	35.7
Case 6b	2273	9	2.3×10^8	3.81×10^{-5}	920	9.807	532032	35.7

Table 6.8: Independent variables for dimensional analysis

	L_g (m)	w_g (m)	N	κ_f (K^{-1})	ΔT_c (K)	p_c (Pa)	b_c (N/m^3)	$E_f t_f$ (N/m)	$\gamma_f = \rho_f g t_f$ (N/m^2)
Base design	148.89	1.306	280	0.00024325	-72	20	0.084887	8745.86	0.344
Variation of dimensionless group 1									
Case 1a	148.895	1.577	280	0.00024325	-72	20	0.084887	8745.86	0.344
Case 1b	148.886	1.453	280	0.00024325	-72	20	0.084887	8745.86	0.344
Variation of dimensionless group 2									
Case 2a	148.889	1.306	300	0.00024325	-72	20	0.084887	8745.86	0.344
Case 2a	148.904	1.306	330	0.00024325	-72	20	0.084887	8745.86	0.344
Variation of dimensionless group 3									
Case 3a	148.89	1.305	280	0.00024325	-72	20	0.084887	34983.42	0.344
Case 3b	148.89	1.305	280	0.00024325	-72	20	0.084887	61220.99	0.344
Variation of dimensionless group 4									
Case 4a	148.89	1.306	280	0.00024325	-72	40	0.084887	17491.71	0.344
Case 4b	148.89	1.305	280	0.00024325	-72	10	0.084887	4372.93	0.344
Variation of dimensionless group 5									
Case 5a	148.89	1.306	280	0.00024325	-72	20	0.169774	8745.86	0.344
Case 5b	148.89	1.306	280	0.00024325	-72	20	0.0424435	8745.86	0.344
Variation of dimensionless group 6									
Case 6a	148.89	1.306	280	0.00024325	-36	20	0.084887	8745.86	0.344
Case 6b	148.89	1.306	280	0.00024325	-18	20	0.084887	8745.86	0.344

Table 6.9: Dimensionless groups and clefting results for dimensional analysis

	Dimensionless groups						Clefting result	
	(1) $\frac{w_g}{L_g}$	(2) N	(3) $\frac{p_c L_g}{E_f t_f}$	(4) $\frac{p_c}{\gamma_f}$	(5) $\frac{\gamma_f}{b_c L_g}$	(6) $-\kappa_f \Delta T_c$	CF_5	Cleft or not
Base design	0.00877	280	0.340	58.2	0.0272	0.0175	193.2	N
Variation of dimensionless group 1								
Case 1a	0.0106	280	0.340	58.2	0.0272	0.0175	36	Y
Case 1b	0.00976	280	0.340	58.2	0.0272	0.0175	61	Y
Variation of dimensionless group 2								
Case 2a	0.00877	300	0.340	58.2	0.0272	0.0175	74.9	Y
Case 2b	0.00877	330	0.341	58.2	0.0272	0.0175	33.6	Y
Variation of dimensionless group 3								
Case 3a	0.00876	280	0.0851	58.2	0.0272	0.0175	309.9	N
Case 3b	0.00877	280	0.0486	58.2	0.0272	0.0175	360.6	N
Variation of dimensionless group 4								
Case 4a	0.00877	280	0.0340	116.36	0.0272	0.0175	243.6	N
Case 4b	0.00877	280	0.0340	29.09	0.0272	0.0175	145.4	N
Variation of dimensionless group 5								
Case 5a	0.00877	280	0.0340	58.2	0.0136	0.0175	386.4	N
Case 5b	0.00877	280	0.0340	58.2	0.0544	0.0175	96.6	Y
Variation of dimensionless group 6								
Case 6a	0.00877	280	0.034	58.2	0.0272	0.00876	193.2	N
Case 6b	0.00877	280	0.034	58.2	0.0272	0.00438	193.2	N

$$CF_6 = 4.876 \times 10^{-13} \times \left(\frac{w_g}{L_g}\right)^{13.75} N^{13.70} \left(\frac{p_c L_g}{E_f t_f}\right)^{0.729} \left(\frac{p_c}{\gamma_f}\right)^{0.418} \left(\frac{\gamma_f}{b_c L_g}\right)^{-2.317} (-\kappa_f \Delta T_c)^{-1.172} \quad (6.16)$$

Then expanding in terms of the independent variables

$$CF_6 = 4.876 \times 10^{-13} \times L^{-10.704} {w_g}^{13.75} N^{13.70} \kappa_f^{-1.172} (-\Delta T_c)^{-1.172} p_c^{1.147} b_c^{2.317} (E_f t_f)^{-0.729} (\gamma_f)^{-2.735} \quad (6.17)$$

The power coefficients of the independent design parameters are shown in Table 6.11. Starting from the base design, we can now study the effect of varying each individual independent variable from -20% to 20% on the cleft factor CF_6. The results are plotted in Figure 6.5. The first three variables L_g, w_g and N have an overwhelming influence on the cleft factor, i.e., geometric factors dominate deployment of the base design balloon. Although the base design was safe from clefting, as $CF_6 = 0.103 \ll 0.8$, Figure 6.5 shows that increasing the gore width w_g or the lobe number N by 16% causes CF_6 to reach the critical value. Also decreasing the gore length L_g by 17% causes CF_6 to become critical. This result can be understood by noting that a higher ratio of the total equatorial circumferential length to the gore length corresponds to more excess material.

Table 6.10: Cleft factor CF_6 and power coefficient α_i for dimensional analysis

	Axi-symmetric volume V_{sym} (m^3)	Clefted volume V_{cf} (m^3)	Cleft factor CF_6	Fitting cleft factor	Cleft or not	Power coefficient α_i
Base design	503096	503614	0.103	0.103	N	NA
Variation of dimensionless group 1						
Case 1a	521809	529342	1.44	1.39	Y	13.75
Case 1b	516199	517816	0.313	0.448	N	
Variation of dimensionless group 2						
Case 2a	513526	515022	0.291	0.265	N	13.70
Case 2b	517514	522620	0.987	0.978	Y	
Variation of dimensionless group 3						
Case 3a	402216	402373	0.0390	0.0375	N	0.729
Case 3b	389703	389799	0.0246	0.0249	N	
Variation of dimensionless group 4						
Case 4a	502687	503401	0.142	0.138	N	0.418
Case 4b	514421	514781	0.0796	0.0771	N	
Variation of dimensionless group 5						
Case 5a	498857	502139	0.658	0.513	N	-2.317
Case 5b	505372	505506	0.0265	0.021	N	
Variation of dimensionless group 6						
Case 6a	530692	531510	0.154	0.232	N	-1.172
Case 6b	536329	539126	0.522	0.522	N	

Table 6.11: Power coefficients of independent variables

No.	1	2	3	4	5	6	7	8	9
Parameter	L_g	w_g	N	κ_f	$-\Delta T_c$	p_c	b_c	$E_f t_f$	$\gamma_f = \rho_f g t_f$
Power coefficient	-10.704	13.75	13.70	-1.172	-1.172	1.147	2.317	-0.729	-2.735

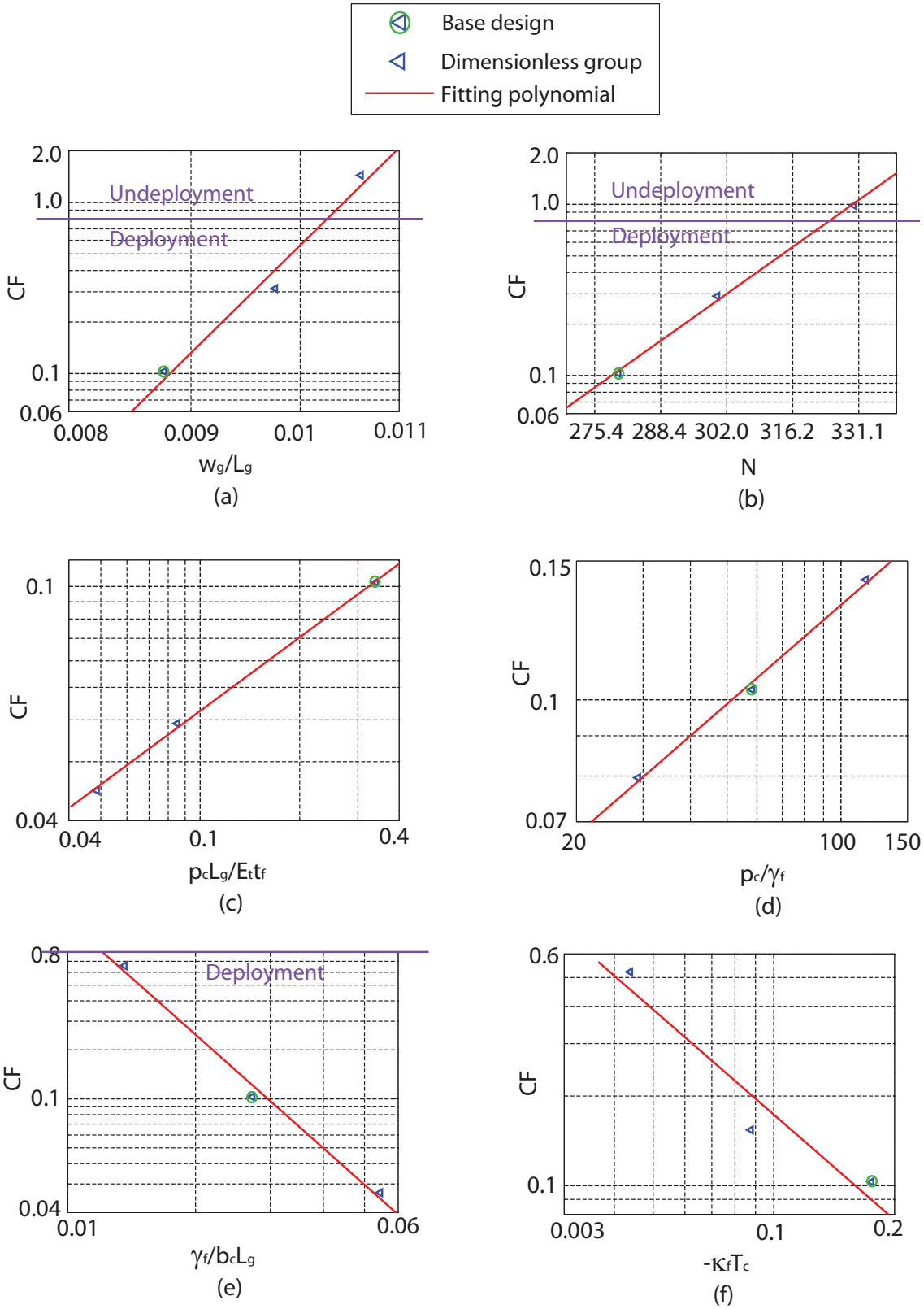

Figure 6.4: Fitting of power coefficients α_i: (a)-(f) for dimensionless group No.1 - No.6.

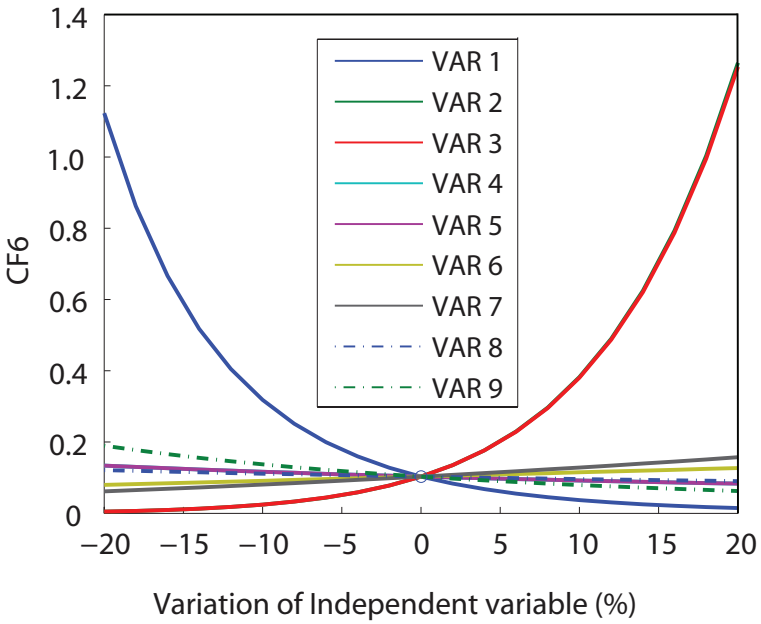

Figure 6.5: Sensitivity of independent variables.

Chapter 7

Conclusion

This thesis has presented a study of the deployment of superpressure balloon structures through numerical and analytical models. The lobed pumpkin shape of superpressure balloons that has been chosen for structural efficiency has led to complications during deployment: several balloons have not deployed into the expected, cyclically symmetrical equilibrium configuration, but have settled into unexpected asymmetric shapes. Clefts due to incomplete deployment were observed during early flight tests of these balloons. This puzzling shape anomaly consists of a single non-meridional cleft spanning from top to bottom of the balloon and involving several lobes. The design of balloon structures is based on axi-symmetric configurations of fully inflated balloons, so the occurrence of clefts was made their design uncertain. Clefting is a regular feature of balloons that are incompletely inflated, and is regularly seen during launch and ascent. Our particular interest is in clefts that remain once a balloon has reached its float altitude and is fully pressurized.

A detailed material model that allows for both anisotropy and visco-elasticity has been established. The method developed, based on a modification of the material stiffness matrix to incorporate the effects of orthotropic wrinkling and viscoelasticity, has been shown to be an effective way of capturing in a finite element simulation the behavior of a real plastic film. In the wrinkling model the state of a membrane element (taut, wrinkled, slack) is defined by a mixed wrinkling criterion. Once it has been established that a membrane element is wrinkled, an iterative scheme searches for the wrinkle orientation angle and the correct stress distribution, involving only uniaxial tension in the wrinkle direction, is then obtained.

This wrinkling model has been validated by a comparison with a published solution for the case of a time-independent isotropic membrane under simple shear. The model has then been applied to a particular type of viscoelastic balloon film, known as StratoFilm 420. Using the Rand-Schapery model for this film, a time-dependent pseudoelastic stiffness matrix was defined and so, instead of having to compute the convolution integral throughout the simulation, we were able to compute the behavior of a membrane structure by superposition of a series of incremental response functions. These calculations were implemented in standard finite element software.

Experimental tests on StratoFilm 420 under simple shear were carried out, including loading and unloading, and the experimental results were compared with ABAQUS/Explicit simulations. The results agree

very well once friction and dynamic effects are excluded. There are differences of about 10% in the shear forces measured on membranes arranged in different material directions, as StratoFilm 420 has only weak anisotropy and so the direction of the wrinkles changed by less than 4° when the film was rotated through 90°. Significant differences were seen between loading and unloading, indicating that viscoelastic behavior is a significant source of energy dissipation. It has been shown that for the SF 420 balloon film acceptable results are obtained by pseudoelastic simulations based on a two-step loading function and so extension of this approach to balloon simulations should be much more efficient than attempting to predict their detailed behavior using a more detailed representation of the loading.

A three-dimensional finite-element model that incorporates wrinkling and frictionless contact has been constructed to simulate the shapes taken up by the balloons during the final stages of their ascent and pressurization. The loading on the balloon is a non-uniform differential pressure with constant gradient along the height. The three-dimensional solutions are obtained with ABAQUS/Explicit, with a user-defined material subroutine for elastic isotropic wrinkling that implements a mixed stress-strain criterion. Frictionless contact is defined for the surface of balloon to prevent the penetration of the balloon through itself. The initial geometry of the lobes is mapped onto their (flat) cutting pattern, and this allows us to compute the initial stresses and strains with ease.

Two different methods have been considered to predict the clefts: (i) deflation and inflation method and (ii) constraint shift method. In method i, the starting configuration for the deflation simulation is obtained by deflating an initially symmetric balloon subject to uniform pressure. During deflation extensive wrinkling occurs and this is followed by the formation of many clefts throughout the balloon, as large amounts of balloon film are ingested within the balloon envelope. The geometry of the balloon loses its initial symmetry during this simulation. The deflation simulation is continued until the differential pressure at the bottom of the balloon has become negative, at which point the balloon is extensively clefted. The balloon is then inflated by increasing the bottom pressure while maintaining a uniform vertical pressure gradient, and the evolution of the shape and stress distribution of the balloon is studied. Two different designs of superpressure balloons have been investigated: a flat facet balloon and a lobed balloon with lobes that have a bulge radius of 0.284 m and an angle of 98.1° at the equator. A study of the flat facet balloon has shown that it follows essentially the same path during deflation and inflation, hence it can be argued that the inflated shape of this flat facet balloon is solely determined by differential pressure. The uniqueness of its loading path also leads to the conclusion that complete deployment into the design axi-symmetric shape is to be expected. A similar study of a highly lobed balloon has shown that inflation process doesn't mirror the deflation and so the geometry of the balloon has inflated into an alternate, clefted equilibrium shape.

Although the deflation and inflation method can produce detailed pictures of the loading paths for better understanding of the behavior of clefting, it is less computationally efficient for the requirement of multiple case studies. Assuming that material dissipation can be ignored, a perturbation method to artificially break the symmetry of a balloon and seeding a clefting perturbation has been presented. Gravity effects, isotropic

wrinkling of the film and frictionless self-contact in the balloon are all included in the analysis. The method has been shown to be an effective way of both capturing S-clefts and predicting clefting in balloons with different cutting pattern designs.

Seeding a clefting perturbation is the key step in our analysis; it has been implemented through the constraint-shift method, which has been divided into two steps. Starting from the cyclically symmetrical configuration of the balloon, in step 1, the balloon is constrained at a single offset point and the pressure is removed in the bottom region, below the shifted constraint. Thus the stress distribution becomes asymmetric and a single large cleft is allowed to appear. Once this disturbance has been introduced, in step 2 of the analysis the bottom apex constraint is moved back to the original apex and the non-uniform pressure is applied to the whole balloon.

The constraint-shift method has been tested on three 27 m diameter superpressure balloons that had been designed and tested by the NASA superpressure balloon team, Balloon # 1, # 4 and # 5. These balloons all had 200 lobes but the lobe bulge angles at the equator were respectively 98.1 °, 55 ° and 90 °. In the indoor tests Balloon # 1 had remained clefted, with a typical S-cleft at a pressure of 10 Pa, while the other two balloons had deployed completely. Visual comparisons between simulation results and test observations for the shape of the S-cleft occurring in Balloon # 1 have shown remarkable agreement and so it can be concluded that for the first time an S-cleft has been captured computationally. We have computed the total potential energy of this balloon in the clefted configuration and compared it to the energy in the axi-symmetric configuration; because the volume of the clefted balloon is larger, we have found that the clefted shape is more stable. Hence increasing the pressure in this balloon will not eliminate the cleft. We have also shown that the S-cleft will not disappear if the balloon is allowed to pass through itself. Instead of forming an S-cleft, the balloon formed a meridional cleft with the spare film arranged around a kind of inner tube attached to the balloon. The constraint-shift method has also successfully predicted the full deployment of Balloons # 4 and # 5.

To further reduce the computational load of future NASA balloon designs, a new cleft factor CF_6 as an indicator of the tendency to S-cleft for superpressure balloons based on constant-stress design has been formulated through dimensional analysis. Nine independent variables have been chosen from a complete list of design parameters and then combined into 6 independent dimensionless groups. An analytical expression for the cleft factor, defined as the ratio of clefted volume to cyclically symmetrical volume, has been formulated as a power law expression in terms of the dimensionless groups. An example illustrates how to calculate the power coefficients of the analytical formula and analyze sensitivity of clefting to changes in the values of the design parameters.

In conclusion, the thesis has characterized clefted equilibrium shapes of superpressure balloon structures. The kind of instability that we have investigated could not be captured using the general theory of elastic stability of structures. The key point of departure is that the alternative equilibrium shapes that have been investigated involve wrinkling of the film and slackening of the tendons. For NASA balloon designers, one

of the greatest challenges was finding a compromise between lower film stress, achieved by increasing the bulginess of the lobes and thus their transverse curvature, and a sufficiently stable shape that would deploy symmetrically. Our research work will hopefully improve the optimization of superpressure balloon design.

Bibliography

[1] A. L. Adler. *Finite element approaches for static and dynamic analysis of partially wrinkled membrane structures*. PhD thesis, University of Colorado at Boulder, 2000.

[2] H. Alexander. Tensile instability of initially spherical balloons. *Int. J. Engng. Sci.*, 6:151–162, 1968.

[3] Anonymous. *Research and development in the field of high altitude plastic ballooons*. NONR-710(01) Reports, University of Minnesota, Department of Physics, Minneapolis, MN, 1951-1956.

[4] F. Baginski. A mathematical model for a partially inflated balloon with periodic lobes. *Advances in Space Research*, 30:1167–1171, 2002.

[5] F. Baginski. On the design and analysis of inflated membranes: natural and pumpkin shaped balloons. *SIAM J. Appl. Math.*, 65:838–857, 2005.

[6] F. Baginski and K. Brakke. Exploring the stability lanscape of constant-stress pumpkin balloon designs. *Journal of Aircraft*, 47:849–857, 2010.

[7] F. Baginski, Q. Chen, and I. Waldman. Designing the shape of a large scientific balloon. *Appplied Mathematical Modeling*, 25:953–966, 2001.

[8] F. Baginski and W. Collier. Energy minimizing shapes of patially inflated large scientific baloons. *Advances in Space Research*, 21:975–978, 1998.

[9] F. Baginski and W. W. Schur. Undesired equilibria of self-deploying pneumatic envelopes. *Journal of Aircraft*, 42:1639–1642, 2005.

[10] F. E. Baginski, K. A. Brakke, and W. W. Schur. Cleft formation in pumpkin balloons. *Advances in Space Research*, 37:2070–2081, 2006.

[11] G. I. Barenblatt. *Scaling, self-similarity, and intermediate asymptotics*. Cambridge university press, 1996.

[12] C. R. Calladine. *Stability of the Endeavour balloon*. Elsevier Science Publisher, 1988.

[13] H. M. Cathey. Test flights of the nasa ultra-long duration balloon. *Advances in Space Research*, 33:1633–1641, 2004.

[14] H. M. Cathey. *ULDB 27 m diameter balloon indoor launch, inflation, and deployment test report.* Test report, Physical Science Laboratory, NASA BPO, May 2007.

[15] H. Chater and J. W. Hutchinson. On the propagation of bulges and buckles. *Journal of Applied Mechanics*, 18:1–9, 1984.

[16] M. Epstein and M. A. Forcinito. Anisotropic membrane wrinkling: theory and analysis. *International Journal of Solids and Structures*, 38:5253–5272, 2001.

[17] R. Farley. *Balloon ascent theory manual version 6.0c.* NASA Goddard space flight center, April 2011.

[18] T. Gerngross and S. Pellegrino. Implementation and validation of schapery-rand anisotropic viscoelasticity model for super-pressure balloons. In *AIAA Balloon Systems Conference, 21-24 May, 2007*, Williamsburg, VA, 2000.

[19] T. Gerngross and S. Pellegrino. Modelling of anisotropic viscoelastic behaviour in super-pressure balloons. In *48th AIAA/ASME/ASCE/AHS/ASC Structures, Structural Dynamics and Materials Conference*, Honolulu, Hawaii, 2007.

[20] T. Gerngross and S. Pellegrino. Anisotropic viscoelasticity and wrinkling of superpressure balloons: simulation and experimental verification. In *AIAA Balloon Systems Conference*, Seattle, WA, 2009.

[21] D. D. Gregory. Implementing new strategic plans for nasa long duration scientific balloons. *Advances in Space Research*, 37:2021–2025, 2006.

[22] H. Irvine. *Cable structure.* MIT Press, 1981.

[23] C. H. Jenkins, F. Haugen, and W. H. Spicher. Experimental measurement of wrinkling in membranes undergoing planar deformation. *Exp. Mech.*, 38:147–152, 1998.

[24] S. Kang and S. Im. Finite element analysis of wrinkling membranes. *Journal of Applied Mechanics*, 64:263–269, 1997.

[25] B. A. Lennon. *Equilibrium and Stability of Inflatable Membrane Structures.* PhD thesis, University of Cambridge, Department of Engineering, 2002.

[26] B. A. Lennon and S. Pellegrino. Stability of lobed inflatable structures. In *41st AIAA/ASME/ASCE/AHS/ASC Structures, Structural Dynamics, and Materials Conference*, number AIAA 2000-1728, 2000.

[27] E. H. Mansfield. Analysis of wrinkled membranes with anisotropic and non-linear elastic properties. *Proc. R. Soc. London A. 353*, pages 475–498, 1977.

[28] N. G. McCrum, C. P. Buckley, and C. B. Bucknall. *Principles of polymer engineering, 2nd edition.* Oxford science publications, Oxford, 2003.

[29] M. M. Mikulas. *Behavior of a flat stretched membrane wrinkled by the rotation of an attached hub.* NASA Technical Note TN D-2456, Langley Research Center, Langley Field, Va, 1964.

[30] R. K. Miller and J. M. Hedgepeth. An algorithm for finite element analysis of partly wrinkled membranes. *AIAA Journal*, 20:1761–1763, 1982.

[31] R. K. Miller, J. M. Hedgepeth, V. I. Weingarten, P. Das, and S. Kahyai. Finite element analysis of partly wrinkled membranes. *Computers & Structures*, 20:631–639, 1985.

[32] R. W. Ogden. *Non-Linear Elastic Deformations.* Dover Publications, Minneola, NY, 1997.

[33] M. Pagitz and S. Pellegrino. Buckling pressure of pumpkin balloons. *International Journal of Solids and Structures*, 44:6963–6986, 2007.

[34] M. Pagitz and S. Pellegrino. Maximally stable lobed balloons. *International Journal of Solids and Structures*, 47:1496–1507, 2010.

[35] M. E. Pagitz. *Analytical and numerical studies of superpressure balloons.* PhD thesis, University of Cambridge, Department of Engineering, 2007.

[36] A. C. Palmer. *Dimensional analysis and intelligent experimentation.* World Scientific Publishing Co. Pte. Ltd., 2008.

[37] W. H. Paulsen. What is the shape of a mylar balloon. *The American Mathematical Monthly*, 101:953–958, 1994.

[38] A. C. Pipkin. The relaxed energy density for isotropic elastic membranes. *IMA J. Appl. Math*, 36:85–99, 1986.

[39] A. C. Pipkin and D. J. Steigmann. Wrinkling of pressurized membranes. *Transactions of the ASME*, 56:624–628, 1989.

[40] T. Raible, K. Tegeler, S. Lohnert, and P. Wriggers. Development of a wrinkling algorithm for orthotropic membrane materials. *Computer Methods in Applied Mechanics and Engineering*, 194:2550–2568, 2005.

[41] E. L. Rainwater and M. S. Smith. Ultra high altitude balloons for medium-to-large payloads. *Advances in Space Research*, 33:1648–1652, 2004.

[42] J. L. Rand. *Shape and stress of an ascending balloon.* Report no. wii-9936-fr-01, NASA/Jet Propustion Lab, Pasadena, CA, 1987.

[43] J. L. Rand. *An improved constitutive equation for SF420, part I: the master curve.* Internal Report, Winzen Engineering Inc., 2008.

[44] J. L. Rand. *An improved constitutive equation for SF420, part II: the biaxial behavior*. Internal Report, Winzen Engineering Inc., 2008.

[45] E. Reissner. On tension field theory. In *Proceedings Fifth International Congress of Applied Mechanics*, pages 88–92, 1938.

[46] R. A. Schapery. On the characterization of nonlinear viscoelastic material. *Polymer engineering and science*, 9:295–310, 1969.

[47] R. A. Schapery. Nonlinear viscoelastic and viscoelastic constitutive equations based on thermodynamics. *Polymer engineering and science*, 1:209–240, 1997.

[48] W. W. Schur. Experimental investigation of undesired stable equilibria in pumpkin shape super-pressure balloon designs. *Advances in Space Research*, 33:1682–1687, 2003.

[49] J. H. Smalley. *Determination of the shape of a free balloon*. Scientific report no. 2, AFRL 64-374, Air Force Cambridge Research Labovatories, Bedford, MA, 1963.

[50] I. S. Jr. Smith. The nasa baalloon program: an overview. *Advances in Space Research*, 30:1087–1094, 2002.

[51] I. S. Jr. Smith. The nasa balloon program: looking to the future. *Advances in Space Research*, 33:1588–1593, 2004.

[52] M. S. Smith and E. L. Rainwater. Optimum designs for superpressure balloons. *Advances in Space Research*, 33:1688–1693, 2003.

[53] M. Stein and J. M. Hedgepeth. *Analysis of partly wrinkled membranes*. NASA Technical Note TN D-813, Langley Research Center, Langley Field, Va, 1961.

[54] J. M. Stubstad and G. J. Simitses. Bounding solutions of geometrically nonlinear viscoelastic problems. *AIAA Journal*, 24, 1986.

[55] G.I. Taylor. *The Scientific Papers of Sir G.I. Taylor*. Cambridge university press, 1963.

[56] I. M. Ward. *Mechanical properties of solid polymers, 2nd edition*. John Wiley & Sons, 1985.

[57] Y. W. Wong and S. Pellegrino. Wrinkled membranes. part i: experiments. journal of mechanics of materials and structures. *Journal of Mechanics of Materials and Structures*, 1:1–23, 2006.

[58] Y. W. Wong and S. Pellegrino. Wrinkled membranes. part ii: analytical models. journal of mechanics of materials and structures. *Journal of Mechanics of Materials and Structures*, 1:25–59, 2006.

[59] Y. W. Wong and S. Pellegrino. Wrinkled membranes. part iii: numerical simulations. journal of mechanics of materials and structures. *Journal of Mechanics of Materials and Structures*, 1:61–93, 2006.

[60] C. H. Wu. The wrinkled axisymmetric air bags made of inextensible membranes. *J. Appl. Mech.*, 41:963–968, 1974.

[61] C. H. Wu. Nonlinear wrinkling of nonlinear membranes of revolution. *J. Appl. Mech.*, 45:533–538, 1978.

[62] C. H. Wu and T. R. Canfield. Wrinkling in finite plane-stress theory. *Quart. Appl. Math.*, 39:179–199, 1981.

[63] Y. Xu. *A computational study of lobed balloons.* PhD thesis, University of Cambridge, Department of Engineering, 2007.

Appendix A

ABAQUS Details

This appendix provides ABAQUS commands regarding the finite element modeling of balloon structures incorporating frictionless contact and user subroutine to simulate isotropic wrinkling.

A.1 ABAQUS sample file

This is an abbreviated version of ABAQUS .inp file for a full scaled balloon structure incorporating frictionless contact subject to gradient pressure.

```
**
*include,input=node.txt
*include,input=elem_M3D3.txt
**Lobe
*ELSET, ELSET=FILM_LOBE, GENERATE
 1, 2
 .
 .
 .
 54801, 54802
*ELSET, ELSET=LOBE, GENERATE
 1, 2
 .
 .
 .
 55201, 55336, 1
*ELSET, ELSET=TENDON_LOBE, GENERATE
 55201, 55336, 1
*ELSET, ELSET=RIGID_UP_WHOLE, GENERATE
```

```
 1, 400, 1
*ELSET, ELSET=RIGID_DOWN_WHOLE, GENERATE
 54801, 55200, 1
*NSET, NSET=RIGID_UP_WHOLE, ELSET=RIGID_UP_WHOLE
*NSET, NSET=RIGID_DOWN_WHOLE, ELSET=RIGID_DOWN_WHOLE
*NSET, NSET=SLIDED
1
*NSET, NSET=FIXED
209
*ELSET, ELSET=SURF-1_SPOS, GENERATE
 1, 55200, 1
 .
 .
 .
*RIGID BODY, REF NODE=1, ELSET=RIGID_UP_WHOLE,TIE NSET=RIGID_UP_WHOLE
*RIGID BODY, REF NODE=209, ELSET=RIGID_DOWN_WHOLE,TIE NSET=RIGID_DOWN_WHOLE
*Surface, type=ELEMENT, name=SURF-1
SURF-1_SPOS, SPOS
** film
**
*MEMBRANE SECTION, ELSET=FILM, MATERIAL=LLDPE, controls=LLDPE
      1.32E-5,
**
** tendon
**
*SOLID SECTION, ELSET=TENDON, MATERIAL=PBO, controls=PBO
       2.E-5,
**
** rigid_shell
**
*SHELL SECTION, ELSET=RIGID_SHELL, MATERIAL=END_FITTING
      0.0001,       5
**
** LLDPE
**
*MATERIAL, NAME=LLDPE
```

```
**
*DENSITY
920.,
*DEPVAR
      4,
*USER MATERIAL, CONSTANT=2
 1.01e+08, 0.7325
**
** PBO
**
*MATERIAL, NAME=PBO
**
*DENSITY
        300.,
**
*ELASTIC, TYPE=ISO
     4.25E+9,       0.333
**
** END_FITTING
**
*MATERIAL, NAME=END_FITTING
**
*DENSITY
       1200.,
**
*ELASTIC, TYPE=ISO
      4.5E+9,        0.33
**
** INTERACTION PROPERTIES
**
*Surface Interaction, name=INTPROP-1
*Friction
0.,
*Surface Behavior, pressure-overclosure=HARD
**
** BOUNDARY CONDITIONS
```

```
**
** Name: Disp-BC-1 Type: Displacement/Rotation
*Boundary
FIXED, 1, 3
** Name: Disp-BC-2 Type: Displacement/Rotation
*Boundary
SLIDED, 2, 3
**
** INTERACTIONS
**
** Interaction: general_contact
*Contact, op=NEW
*Contact Inclusions
SURF-1 ,
*Contact property assignment
 ,  , INTPROP-1
*Amplitude, name=pressure1, definition=SMOOTH STEP
0., 0., 10.,1
**
*include,input=ref_coord.txt
**
** STEP: Step-1
**
*Step, name=Step-1
*Dynamic, Explicit
, 10
*Bulk Viscosity
0.05, 0
** LOADS
**
** Name: Pressure1   Type: Pressure
*Dsload, amplitude=pressure1
SURF-1, PNU, 1.
**
** OUTPUT REQUESTS
**
```

```
*Restart, write, number interval=50, time marks=NO
**
** FIELD OUTPUT: F-Output-1
**
*Output, field, time interval=0.20
*Node Output
A, COORD, RF, U, V
**
** FIELD OUTPUT: F-Output-2
**
*Element Output, directions=YES
LE, PE, PEEQ, S
**
** HISTORY OUTPUT: H-Output-1
**
*Output, history, time interval=0.20
*Contact Output, surface=SURF-1
CAREA, CFN, CFS, CFT, CMN, CMS, CMT, XN, XS, XT
*Energy Output
ALLAE, ALLKE, ALLSE, ALLVD, ALLWK, ETOTAL
*End Step
```

The following command is to specify non-uniformly distributed load with the option "PNU" using

```
*Dsload, amplitude=pressure1
SURF-1, PNU, 1.
```

For deflation and inflation simulations, the magnitude of non-uniform load is defined in user subroutine VDLOAD

```
value(km)=10+(curCoords(km,1)+8.209454)*0.163
```

where 10 is the differential bottom pressure, and 0.163 is the pressure gradient.

For clefting test, in Step 1, the bottom constraint is shifted from node 209 to the node group 194, 195 and 196 at a radial distance from the axis, which can be specified using

```
*NSET, NSET=FIXED
**209
194,195,196
```

The shifted constraints are applied on the three nodes so that the balanced forces are less concentrated on a very small region. Then we redefine the surface that is the whole balloon excluding the bottom region to apply the non-uniform pressure.

```
*ELSET, ELSET=_SURF-1_SPOS, GENERATE
1,51600,1
**1, 55200, 1
```

In Step 2, the bottom constraint is the constraint is moved to the central point O at the bottom of the balloon shown as follows

```
*NSET, NSET=FIXED
209
```

The non-zero pressure distribution Δp is applied to the whole balloon with the command

```
*ELSET, ELSET=_SURF-1_SPOS, GENERATE
1, 55200, 1
```

A.2 User subroutine Vumat

The user-defined material subroutine `Vumat`, which implements combined wrinkling criterion based on variable Poisson's ratio method, is used to incorporate the wrinkling effects into the balloon film model. In practice, the constitutive matrix D is updated at each increment according to different status of individual membrane element. The code is displayed as follows:

```
*USER SUBROUTINES
    subroutine vumat(
C Read only (unmodifiable)variables -
     1  nblock, ndir, nshr, nstatev, nfieldv, nprops, lanneal,
     2  stepTime, totalTime, dt, cmname, coordMp, charLength,
     3  props, density, strainInc, relSpinInc,
     4  tempOld, stretchOld, defgradOld, fieldOld,
     5  stressOld, stateOld, enerInternOld, enerInelasOld,
     6  tempNew, stretchNew, defgradNew, fieldNew,
C Write only (modifiable) variables -
     7  stressNew, stateNew, enerInternNew, enerInelasNew )
C
      include 'vaba_param.inc'
```

```
C
      dimension props(nprops), density(nblock), coordMp(nblock,*),
     1  charLength(nblock), strainInc(nblock,ndir+nshr),
     2  relSpinInc(nblock,nshr), tempOld(nblock),
     3  stretchOld(nblock,ndir+nshr),
     4  defgradOld(nblock,ndir+nshr+nshr),
     5  fieldOld(nblock,nfieldv), stressOld(nblock,ndir+nshr),
     6  stateOld(nblock,nstatev), enerInternOld(nblock),
     7  enerInelasOld(nblock), tempNew(nblock),
     8  stretchNew(nblock,ndir+nshr),
     8  defgradNew(nblock,ndir+nshr+nshr),
     9  fieldNew(nblock,nfieldv),
     1  stressNew(nblock,ndir+nshr), stateNew(nblock,nstatev),
     2  enerInternNew(nblock), enerInelasNew(nblock)

      character*80 cmname
      real DDSDDE(nblock,ndir+nshr,ndir+nshr)
    real PSIG(nblock,ndir),PEPS(nblock,ndir)
    real E,NU

    Integer i,j,k,IFLAG,STATE

      E=PROPS(1)
      NU=PROPS(2)

      do 100 i=1,nblock
C
    do j=1,nstatev-1
    stateNew(i,j)=stateOld(i,j)+strainInc(i,j)
    end do

C     FORM INITIAL STIFFNESS MATRIX
      do j=1,ndir+nshr
      do k=1,ndir+nshr
       DDSDDE(i,j,k)=0
    end do
```

```
      end do

C     FORM TAUT STIFFNESS MATRIX
      DDSDDE(i,1,1)=E/(1.0-NU*NU)
      DDSDDE(i,1,2)=E*NU/(1.0-NU*NU)
      DDSDDE(i,2,1)=DDSDDE(i,1,2)
      DDSDDE(i,2,2)=DDSDDE(i,1,1)
      DDSDDE(i,4,4)=E/(2.0*(1.0+NU))

C     CALCULATE CURRENT STRESS VALUES
      stressNew(i,1)=DDSDDE(i,1,1)*stateNew(i,1)+DDSDDE(i,1,2)
     $*stateNew(i,2)+DDSDDE(i,1,3)*stateNew(i,3)+DDSDDE(i,1,4)
     $*stateNew(i,4)

      stressNew(i,2)=DDSDDE(i,2,1)*stateNew(i,1)+DDSDDE(i,2,2)
     $*stateNew(i,2)+DDSDDE(i,2,3)*stateNew(i,3)+DDSDDE(i,2,4)
     $*stateNew(i,4)

      stressNew(i,3)=DDSDDE(i,3,1)*stateNew(i,1)+DDSDDE(i,3,2)
     $*stateNew(i,2)+DDSDDE(i,3,3)*stateNew(i,3)+DDSDDE(i,3,4)
     $*stateNew(i,4)

      stressNew(i,4)=DDSDDE(i,4,1)*stateNew(i,1)+DDSDDE(i,4,2)
     $*stateNew(i,2)+DDSDDE(i,4,3)*stateNew(i,3)+DDSDDE(i,4,4)
     $*stateNew(i,4)


      PSIG(i,1)=(stressNew(i,1)+stressNew(i,2))/2+sqrt(stressNew(i,4)
     $*stressNew(i,4)+(stressNew(i,1)-stressNew(i,2))
     $*(stressNew(i,1)-stressNew(i,2))/4)

      PSIG(i,2)=(stressNew(i,1)+stressNew(i,2))/2-sqrt(stressNew(i,4)
     $*stressNew(i,4)+(stressNew(i,1)-stressNew(i,2))
     $*(stressNew(i,1)-stressNew(i,2))/4)

      PSIG(i,3)=0
```

```
       PEPS(i,1)=(stateNew(i,1)+stateNew(i,2))/2+sqrt(stateNew(i,4)
      $*stateNew(i,4)/4+(stateNew(i,1)-stateNew(i,2))
      $*(stateNew(i,1)-stateNew(i,2))/4)

     PEPS(i,2)=(stateNew(i,1)+stateNew(i,2))/2-sqrt(stateNew(i,4)
      $*stateNew(i,4)/4+(stateNew(i,1)-stateNew(i,2))
      $*(stateNew(i,1)-stateNew(i,2))/4)

     PEPS(i,3)=0

     IFLAG=0
     STATE=1

C     DETERMINE WHEN FIRST ITERATION STARTS (ZEROTH ITERATION WHEN
NO STRAIN)
       j=1
       DO WHILE ((IFLAG.EQ.0).AND.(j.LE.ndir+nshr))
       IF (stateNew(i,j).NE.0.0) IFLAG=1
       j=j+1
       END DO

C   SKIP STATE TESTS FOR ZEROTH ITERATION
       IF (IFLAG.EQ.1) THEN

C     DETERMINE ELEMENT STATE (TAUT, SLACK, OR WRINKLED)
       IF (PSIG(i,2).GT.0.0) THEN
C         SET STRESS VALUES TO CURRENT VALUES (TAUT)
         STATE=1
       ELSE

         IF (PEPS(i,1).GT.0.0) THEN

C       FORM WRINKLED STIFFNESS MATRIX
             Q=(stateNew(i,4))/(PEPS(i,1)-PEPS(i,2))
             P=(stateNew(i,1)-stateNew(i,2))/(PEPS(i,1)-PEPS(i,2))
```

```
          DO j=1,ndir+nshr
              DO k=1,ndir+nshr
                DDSDDE(i,j,k)=0.0
              END DO
            END DO
            DDSDDE(i,1,1)=E*(1.0+P)/2.0
            DDSDDE(i,1,4)=Q*E/4.0
            DDSDDE(i,2,2)=E*(1.0-P)/2.0
            DDSDDE(i,2,4)=DDSDDE(i,1,4)
            DDSDDE(i,4,1)=DDSDDE(i,1,4)
            DDSDDE(i,4,2)=DDSDDE(i,2,4)
            DDSDDE(i,4,4)=E/4.0
        STATE=0
        ELSE

C       FORM SLACK STIFFNESS MATRIX
            DO j=1,ndir+nshr
          DO k=1,ndir+nshr
            DDSDDE(i,j,k)=0.0
          END DO
            END DO
            STATE=-1
        END IF
      END IF
    END IF

C     RECALCULATE CURRENT STRESS VALUES
      stressNew(i,1)=DDSDDE(i,1,1)*stateNew(i,1)+DDSDDE(i,1,2)
     $*stateNew(i,2)+DDSDDE(i,1,3)*stateNew(i,3)+DDSDDE(i,1,4)
     $*stateNew(i,4)

      stressNew(i,2)=DDSDDE(i,2,1)*stateNew(i,1)+DDSDDE(i,2,2)
     $*stateNew(i,2)+DDSDDE(i,2,3)*stateNew(i,3)+DDSDDE(i,2,4)
     $*stateNew(i,4)

      stressNew(i,3)=DDSDDE(i,3,1)*stateNew(i,1)+DDSDDE(i,3,2)
```

```
      $*stateNew(i,2)+DDSDDE(i,3,3)*stateNew(i,3)+DDSDDE(i,3,4)
      $*stateNew(i,4)

     stressNew(i,4)=DDSDDE(i,4,1)*stateNew(i,1)+DDSDDE(i,4,2)
      $*stateNew(i,2)+DDSDDE(i,4,3)*stateNew(i,3)+DDSDDE(i,4,4)
      $*stateNew(i,4)

C     RECALCULATE PRINCIPAL STRESS
       PSIG(i,1)=(stressNew(i,1)+stressNew(i,2))/2+sqrt(stressNew(i,4)
      $*stressNew(i,4)+(stressNew(i,1)-stressNew(i,2))
      $*(stressNew(i,1)-stressNew(i,2))/4)

     PSIG(i,2)=(stressNew(i,1)+stressNew(i,2))/2-sqrt(stressNew(i,4)
      $*stressNew(i,4)+(stressNew(i,1)-stressNew(i,2))
      $*(stressNew(i,1)-stressNew(i,2))/4)

     PSIG(i,3)=0
100   continue
      return
      end
```